Lakehead University

Numerical Analysis of Discontinuous Structures: Static and Dynamic

A Thesis by

Andrew D. Melro

Master of Science in Mechanical Engineering

Submitted to the Faulty of Graduate Studies

in Partial Fulfillment of the Requirements for the

Master's Degree in Mechanical Engineering

Thunder Bay, Ontario

January 2018

Abstract

Discontinuous beam structures can be found in various applications such as adhesive bonded joints and piezoelectric energy harvesters. In adhesive bonded joint design, the single lap joint is commonly used and is constructed by adhering two overlapped materials with an adhesive. It is important to evaluate the static and dynamic behaviours of a single lap joint to mitigate the chance of failure under normal operating conditions. Piezoelectric energy harvesters use piezo-ceramic materials, which are glued to a host structure with a thin layer of adhesive. Studying the dynamic behaviours of piezoelectric energy harvesters is key to achieving optimal power output.

This research presents the use of numerical analysis approaches to investigate the static and dynamic behaviours of discontinuous beam structures, with a focus on applications which require single physics (i.e. static and dynamic behaviours of a single lap joint), and multi-physics (i.e. dynamic behaviours of a piezoelectric energy harvester). Throughout this research, the primary numerical approach used is the finite element method. An alternative approach is the transfer matrix method, to determine the dynamic behaviours of a single lap joint. These numerical approaches are compared with analytical methods and experimental testing, to validate their use. In this research, an experimental apparatus was developed for testing purposes. Overall, the results from the numerical approaches used closely match those from the analytical methods and experimental testing for all applications.

This work investigates key relationships and factors that influence the behaviours of the single lap joint and piezoelectric energy harvesters. The effect of the adhesive layer thickness and the overlap region length on a single lap joint are studied. Increasing the adhesive layer thickness reduces the adhesive stress and the natural frequencies of a single lap joint. The effects of the electrical load resistance and a proof mass on the performance of a piezoelectric energy harvester are discovered. It is found that increasing the electrical load resistance of the piezoelectric energy harvester causes an increase in voltage across the resistor, and the impedance matched resistance, yielding the maximum power output. The proof mass reduces the fundamental frequency, increases the transmissibility function magnitude at this frequency, increases efficiency, and increases the impedance matched resistance of the piezoelectric energy harvester.

Acknowledgements

Firstly, I would like to thank my supervisor, Dr. Kefu Liu, for his guidance and wisdom. Dr. K. Liu encouraged me to pursue my Master's degree, and his continued encouragement and support throughout this degree were paramount in ensuring my successful completion. He has been a strong mentor, and has given me an unmeasurable amount of knowledge on this path, with the occasional reminder to strive for excellence, not perfection. I would like to thank my co-supervisor, Dr. Meilan Liu, for her expertise with regard to the finite element method. Dr. M. Liu ignited within me a passion for the finite element method, which I know will burn long into the distant future. She always made time for me whether it was meetings or conversing in passing. I would like to thank my committee, Dr. Jian Deng and Dr. Ali Tarokh, for taking the time to review and provide feedback. I would like to acknowledge Dr. Ayan Sadhu's generosity for allowing me to use his shaker in the experimental apparatus. I would like to thank S. Stangier, J. Ripku, and K. Bhatia for their assistance in Lakehead University's machine shop.

I would like to thank Bombardier Transportation for their initial involvement in this research, which provided me with a strong foundation to build from, particularly with regard to adhesive bonding. I would also like to thank Maria D'Aniello from 3M for donating a sample of the electrically conductive adhesive transfer tape. I would like to extend my sincere gratitude to the Ontario Graduate Scholarship Program. The funding provided was an enormous benefit towards my research efforts.

I would like to thank my parents, Fernanda and George Melro, my future mother-in-law, Elia Gaspar, my Nieces and Nephews, and my entire family. Your love and support gave me strength and clarity throughout this journey. Specifically, my Nieces and Nephews for always bringing joy and warmth to my heart. I hope you will always overcome the challenges you may face and always chase your dreams.

Most importantly, my eternal appreciation goes to my partner, Carolyn Gaspar. Carolyn has shown me great patience, understanding, support and love, providing me with the drive needed for the successful completion of my Master's. Carolyn was always there to instill in me that extra belief and support when most needed. I am privileged to share this accomplishment with you. Thank you, Carolyn, you have been my number one supporter and I could not do this without you.

Table of Contents

Table of Figures

List of Tables

List of Acronyms and Abbreviations

FE – Finite element

FEM – Finite Element Method

FRF – Frequency response function

PEH – Piezoelectric energy harvester

RMS – Root mean squared

SHM – Structural health monitoring

SLJ – Single lap joint

TMM – Transfer Matrix Method

TR – Transmissibility ratio

Chapter 1 Introduction

1.1. Motivation of the Research

With growing concerns over greenhouse gases and rising fuel costs, the use of lightweight materials and fasteners is an attractive way to improve fuel efficiency in industries such as the automotive and aerospace industries. The Corporate Average Fuel Economy Standards, devised by the Environmental Protection Agency and the National Highway Traffic Safety Administration, regulate average fuel economy and emission targets for the automotive industry in the United States, with which Canada has aligned itself [1]. In 2025, passenger vehicles and light trucks will require an average fuel economy and emissions level of 49.6 mpg (4.74 L/100 km) and 163 g/mi of CO_2 (101 g/km), respectively [2]. Along with technological advancements of vehicle drivetrains, automotive companies are using adhesives and lightweight materials to reduce vehicle weight, thus improving fuel economy and lowering emissions. The Ford F-150 is one example where the company achieves weight reduction of 700 lbs (318 kg) through the use of lightweight materials bonded with adhesives [3], which contributes to an overall improvement in vehicle fuel efficiency and emissions.

Adhesively bonded joints are increasingly utilised in industry due to their desirable characteristics when adhering lightweight materials. They are advantageous as they are easy to apply, have the capability to connect dissimilar and thin materials, have inherent damping characteristics, and are potentially inexpensive [4, 5]. Adhesively bonded joints distribute applied loads evenly across the bond line in comparison to typical fasteners, therefore reducing the presence of stress concentrations [6, 7, 8]. They are also versatile in the manufacturing of complex joint geometries.

Vibration energy harvesting is a growing field with an aim to harness waste energy, which can be beneficial for low power consumption devices such as wireless sensors [9, 10, 11]. A system may experience either free vibration due to an initial displacement and/or velocity, or forced harmonic excitation. When the system experiences free vibration, its mechanical energy is dissipated through internal/external resistance (i.e. damping) in the form of heat. When subjected to forced harmonic excitation, the system continues to oscillate throughout the duration of the applied load, which may not be desired. Vibration energy harvesters attempt to serve a dual purpose by providing vibration absorption for the primary structure, while generating

electrical energy output [12]. Vibration suppression increases the desirability of utilising vibration energy harvesters. Implementation of vibration energy harvesting requires the transformation of mechanical energy into electrical energy. This can be achieved in several ways, including electromagnetic inductance, capacitance, and piezo-ceramic materials.

Research is actively exploring ways in which vibration energy harvesting can be useful in practical applications. In the automotive industry, there is potential to harvest energy from a vehicle's suspension system. One method is to generate electrical energy directly from the vehicle's shock absorber. The function of a conventional shock absorber is to dissipate vibration energy through hydraulic fluid into heat energy. Moallem incorporates an algebraic screw to generate electrical energy, which is connected to a rotary DC machine and boost converter [13], that dissipates vibration energy through electromagnetic inductance. Audi AG has developed a prototype suspension system named eROT, which uses electromechanical rotary dampers rather than hydraulic dampers. According to their test results, the system can recuperate an average of 100 W to 150 W on German roads, with a peak output of 613 W on rough roads [14].

Vibration energy harvesting is also increasingly important in the field of structural health monitoring (SHM) in the pursuit of stand-alone self-powered sensors. The use of wireless sensor networks is attractive when communicating data over relatively large distances, such as in an aircraft or high-rise buildings, to reduce costs associated with coaxial cables [9]. These sensors require a power source which can be provided by batteries, a finite source of power, which must be replaced once depleted. Incorporating energy harvesting into the design of a wireless sensor allows it to be stand-alone and self-powered, thus reducing the cost of replacement batteries and the associated labour costs. Piezoelectric energy harvesters (PEHs) are appropriate in this application when ambient vibrations are present. One significant advantage of using a PEH over electromagnetic or electrostatic energy harvesters is their greater Volume Figure of Merit, which compares transducer performance as a function of their size [15].

Various applications involve discontinuous beam structures such as those previously discussed: adhesively bonded joints and PEHs. The single lap joint (SLJ) is commonly used in adhesively bonded joint design, constructed by joining two overlapped materials with adhesive. In design, it is important to evaluate the static and dynamic behaviour of the SLJ to mitigate the chance of failure under normal operating conditions. PEHs use piezo-ceramic materials bonded

to the host structure with a thin layer of adhesive. The dynamic behaviour of PEHs is key to achieving optimal power output. Analytical solutions for the dynamic behaviour of the SLJ and PEHs cannot be found due to their discontinuous material and geometric properties. Numerical analysis in Engineering is becoming increasingly useful in the design and evaluation of components and systems. Numerical analysis, unlike general symbolic derivations, provides approximate solutions within an acceptable degree of error. Typically, numerical analysis is performed through algorithms, repeated until the error is minimized to an acceptable level. The Finite Element Method (FEM) is a common numerical method that is used to discretize systems into elements. With improvements to computational resources and availability over the years, the FEM has been employed for systems of increasing complexity, which may not have convenient analytical solutions. The Transfer Matrix Method (TMM) is a simple numerical approach relative to the FEM, which can be used to characterise the dynamic behaviour of discontinuous beam structures.

With the increasing use of adhesives in industry and various applications, developing numerical models to design and deploy systems bonded with adhesives could be beneficial. This research will explore the use of numerical analysis approaches to model the behaviour of discontinuous beam structures containing adhesive bonds. Experimental testing and analytical methods, when available, will be compared with the numerical models.

1.2. Literature Review

1.2.1. Lap-Shear Joints

Typically, when designing adhesively bonded joints, the adhesive carries the applied load in shear. This increases the strength of the joint, as adhesives typically perform better in shear than in tension [16]. Thus, lap-shear joints are commonly used in the design of adhesively bonded joints, as they are effective in transmitting tensile forces acting on the adherends and transmit them through the adhesive in shear. Figure 1.1 shows several lap-shear joint designs, where the light grey colour represents the joined adherends, and the dark grey colour represents the adhesive. As shown in Figure 1.1(a), the SLJ is a simple design when compared to the other common lap-shear joints, making it easy to manufacture, and convenient for experimental testing.

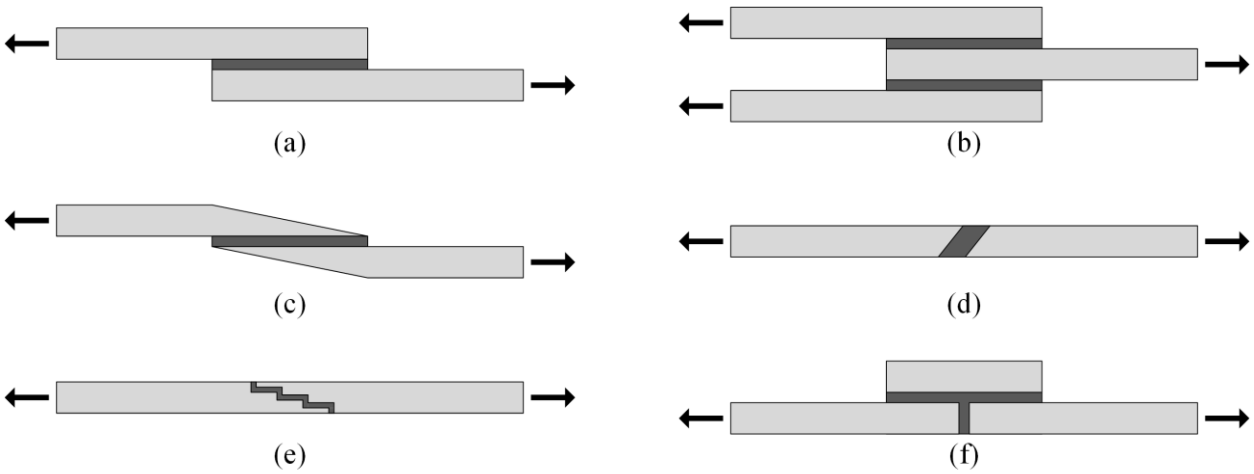

Figure 1.1: Common types of lap-shear joints: (a) single lap; (b) double lap; (c) scarf; (d) bevel; (e) step; (f) butt strap

Although convenient, the geometry of the SLJ introduces an eccentricity in the load path. This causes the adherends to bend, introducing normal stress within the adhesive layer [16], commonly referred to as peel stress in adhesive design. The remainder of this work uses the term peel stress instead of normal stress. Figure 1.2 shows the line of action, the resulting bending in the adherends, and the adhesive's state of stress. Peel stress is an important consideration in the design of adhesively bonded joints as it could be relatively large, and could cause joint failure. Adherend bending also increases the shear stress carried by the adhesive. Therefore, it is important to have models that can reliably predict the stress distribution within the adhesive layer, to ensure the bonded joints do not fail under normal operating conditions.

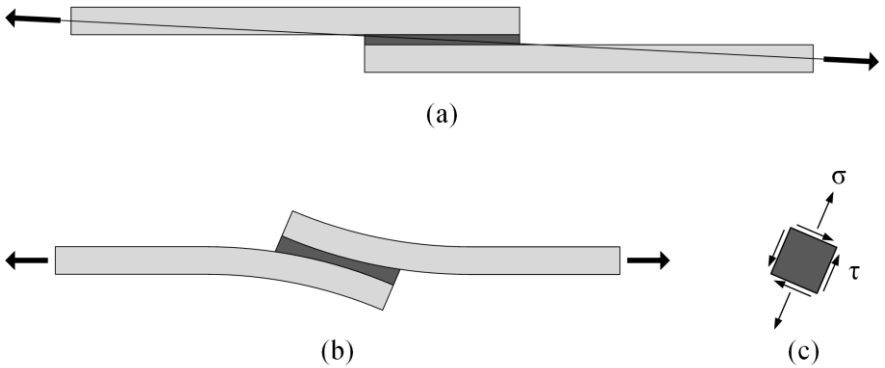

Figure 1.2: Effect of load eccentricity: (a) initial load line of action; (b) bending due to load eccentricity; (c) adhesive stress state.

1.2.1.1. Closed-form Analytical Models

Researchers have developed many closed-form analytical methods for determining the stress distribution within the adhesive region of the SLJ [8]. The shear-lag model, the Goland and Reissner model, and the Hart-Smith model are of particular interest, as they represent classical methods [8, 17], and have been studied in great detail [18, 19, 20, 21, 22, 23]. Each method used different assumptions and considered different contributions to the adhesive stress distributions.

The shear-lag model, developed in 1938 by Volkersen [24], represented an early attempt to describe the stress distribution within an adhesively bonded SLJ. The model is one-dimensional, as the stresses through the thickness of the adhesive and the adherends are assumed to be constant [25]. It neglected bending due to the applied tensile load eccentricity acting on the joint, assuming the adherends deformed in tension only [17, 26]. Therefore, the adhesive layer was subjected to a state of pure shear stress, which disregarded the presence of peel stress. Although this represented a significant weakness of the shear-lag model, it was useful for understanding the relationships between joint design parameters and the resulting shear stress distribution [27].

The shear stress distributions and peak shear stresses within the adhesive layer of adhesively bonded steel and concrete joints have been determined experimentally [19]. A total of 15 specimens, with five steel and adhesive layer thickness configurations, were tested and compared to the shear-lag model, and a finite element (FE) model. While both the shear-lag and FE models closely resembled the experimentally determined shear stress distributions and peak shear stresses, the FE model provided better results for the specimens with the thinnest adhesive layer thickness (1 mm) [19]. Failure loads of single and mixed-adhesively bonded SLJs have also been investigated experimentally [20]. Mixed-adhesively bonded joints were used to increase strength by using ductile and brittle adhesives at the ends and the middle of the overlap area, respectively. Experimental failure loads of the single adhesive SLJs were compared with the shear-lag model and a global yielding criteria. Failure loads found by the shear-lag model compared favourably with experimental failure loads for brittle adhesives, while the global yielding criteria compared favourably for ductile adhesives. These two models were combined to determine the failure loads of the mixed-adhesive SLJs analytically; the shear-lag model and

global yielding criteria were used for the brittle and ductile adhesive regions, respectively. This approach showed good agreement with the experimental failure loads of the mixed-adhesive SLJs [20].

The method developed by Goland and Reissner in 1944 [28] was built from the shear-lag model, by including bending due to the eccentric load path of adhesively bonded SLJs [29]. The adhesive layer was modelled as a spring in the shear and transverse directions, which resulted in constant stress distributions through the adhesive thickness [30], and allowed for the derivation of the adhesive shear and peel stress distributions [4]. As deformation due to bending increased with increased applied tensile load, the load eccentricity was reduced. Consequently, the bending moment and transverse force acting on the overlap region of the SLJ was reduced, introducing geometric non-linearity. To account for this reduction of load eccentricity due to an increased applied load, bending moment and transverse force factors were introduced to relate the applied tensile load to the applied bending moment and transverse force [17].

Tsai and Morton investigated non-linear deformations in SLJs to determine the stress distributions, the bending moment factor, and transverse force factor experimentally [21]. The experimental shear and peel stress distributions were compared with an FE model and the Goland and Reissner model. Although there were similar results between the FE model and the Goland and Reissner method, they did not match well with the experimental shear stress distribution near the end of the overlap region, or with the experimental peel stress distribution, which had been in compression throughout the entire overlap length, therefore violating equilibrium. The shear stress distribution discrepancy was attributed to the presence of a spew fillet in the experimental SLJ specimen at the end of the overlap area, which caused a reduction in shear stress magnitude. The violation of equilibrium found in the experimental peel stress distribution was the result of the measurement method used: moiré interferometry. This method measured the displacement along the length and height of the overlap region along the width's edge instead of along the centerline. This was not a problem for the shear stress distribution, which was relatively constant through the width of the overlap region. However, the peel stress distribution varied through the width. Along the centerline near the end of the overlap region, peel stresses were in tension, becoming more compressive towards the width's edge of the

overlap region. Therefore, it was determined that moiré interferometry was not suitable to measure the peel stress distribution along the centerline of the overlap region [21].

The Hart-Smith model further built upon both the shear-lag and the Goland and Reissner models [4]. Developed in 1973 [31], the model considered both the shear and peel stress distributions within the adhesive layer of the SLJ, by treating the adhesive layer as a spring in the shear and transverse directions, consistent with the Goland and Reissner model. The bending moment and transverse force factors are modified by the Hart-Smith model in pursuit of improved relationships between these and the applied tensile load. The most notable differentiator in the Hart-Smith model was its ability to model the plasticity of the adhesive material [32]. The shear stress-strain relationship of the adhesive material was treated as elastic-perfectly plastic, where the shear stress in locations of material yielding was held constant at the yield shear stress magnitude with increasing shear strain [32].

An experimental investigation to estimate the bending moment factor of an adhesively bonded SLJ was conducted to compare with the analytical bending moment factors modelled by the Hart-Smith and the Goland and Reissner methods, among others [22]. It was found that the bending moment factor modelled by Goland and Reissner was appropriate when the adhesive was thin relative to the adherend thickness. Moreover, the Hart-Smith model of the bending moment factor compared favourably with experimental results when the adhesive overlap length was short [22]. One study investigated the failure load predictions of composite adhesive SLJs using the Hart-Smith model and an FE model [23]. These were compared with experimental failure loads found through bulk tensile tests. The authors tested a ductile and a brittle adhesive, and considered various SLJ overlap lengths. The Hart-Smith model was only used to compare with the experimental results of the brittle adhesive, since it was not suited for ductile adhesive materials, while the FE model was used for both. The tensile tests revealed that the specimens bonded by the brittle adhesive failed through the adhesive for short overlap lengths up to 20 mm, whereas specimens with longer overlap lengths experienced interlaminar failure in the composite adherends. This suggested that failure was the result of peel stress. When compared with the failure load predictions of the Hart-Smith shear stress and peel stress relationships, the peel stress relationship was more favourable than the shear stress relationship, which agreed with the experimental mode of failure. The magnitude of the predicted failure loads in both peel and

shear were less than the experimental results, which suggests that the Hart-Smith model was slightly conservative. The FE model also compared favourably with the experimental results, however, the predicted failure loads were higher than the experimental failure loads [23].

1.2.1.2. The Finite Element Method in Adhesive Joint Design

Much of the work discussed above, specifically [19, 21, 23], included FE models which were designed to model the static behaviour of adhesively bonded joints. The ability to model adhesively bonded SLJs subjected to static loading provided a foundation for increasingly complex models, including dynamic loading. An extensive review of the FEM used in adhesive joint design was presented in [4]. Use of the FEM in adhesively bonded joints subjected to static loading has primarily focused on the ability to model the following: the stress distribution within the adhesive including peak or failure stresses and loads, stress singularities, fracture, and damage. The details of adhesive joint fracture and damage were presented in the aforementioned review [4], and therefore will not be discussed further in this work. The dynamic characteristics of adhesively bonded joints has led to important insights, which are useful in their design and implementation. It is prudent to ensure the adhesively bonded joint is designed to minimize the excitation of resonant frequencies. The dynamic response of adhesively bonded joints may also be useful to determine the health of bonded joints over time [33]. This is particularly important, as they cannot be disassembled in the same way as traditional fasteners, making it difficult to determine their integrity throughout their lifecycle.

Pereira et al. investigated the effects of adherend thickness and overlap length on the shear strength of aluminum adhesive SLJs [34]. A 2D FE model was used to determine the rotation angle of the joint, the stress distribution within the adhesive layer, and the predicted failure load, which were compared to experimental results. Increasing adherend thickness increased the rigidity of the joint, which resulted in a reduction in the rotation angle of the joint. This caused a reduction in shear stress and an increase in peel stress within the adhesive layer, while the failure load of the joint was improved. Increasing the overlap length of the joint showed results similar to those found when increasing adherend thickness, apart from the peel stress within the adhesive layer. It was observed that an increase in the overlap length caused a reduction in the peel stress, which indicated improved joint strength [34]. Díaz et al. [35] investigated the stress and strain behaviour within the adhesive layer of carbon fiber reinforced

plastic SLJs. The SLJ introduced mesh refinement challenges due to the poor aspect ratio of its geometry. The authors developed a parametric 3D FE model as a benchmark to determine the number and type of elements needed to achieve satisfactory results without sacrificing computational time and demand. A total of 26 models with unique element configurations were studied, with the number of elements varying from 4,400 to 695,155, which included shell, solid, cohesive, and continuum shell elements. The adhesive layer strain distribution results were compared with experimental data from a study by Tsai and Morton [36]. Some guidelines were presented, such as the use of a high mesh density near the longitudinal ends of the adhesive material, and a low mesh density in the middle [35]. Experimental verification of a 3D FE model to determine the strength of SLJs joining different materials was conducted [37]. Experimental failure loads for aluminum-aluminum, titanium-titanium, composite-composite, titanium-composite, and aluminum-composite bonded SLJs were found to compare with the numerical results. The FE model consisted of solid elements for the adherends, and cohesive elements for the adhesive region. The numerical failure loads for most configurations compared favourably to the actual failure loads, apart from the titanium-titanium SLJ, which showed an error of 17%. The resulting FE joint deformations at the predicted failure loads were shown to visually compare them with the resulting experimental deformation after joint failure, which showed good agreement [37].

The tapering of adherends was studied to reduce adhesive peak stresses, and to shift their location away from the end of the adhesive layer. Haghani et al. [38] investigated the effect of normal and reverse tapering and material properties of carbon fiber reinforced plastic laminates that were bonded to existing structures to restore their strength. The tapering length and material properties of the laminate and adhesive were varied to understand their effects. FE models for normal and reverse tapered laminates were used to determine the peak stresses within the adhesive, along with the corresponding stress distribution, to determine whether the position of the peak stresses had been impacted. These were compared to an FE model of a laminate with no tapering. Reverse tapering was found to have the most significant impact on the position of adhesive peak shear and peak principal stress, moving their position further away from the end of the adhesive layer. The effect of normal tapering on the peak shear stress and peak principal stress were negligible within a reasonable tapering length, whereas reverse tapering caused a significant reduction in these stresses even for relatively short tapering lengths. However, both

normal and reverse tapering caused an increase in peak peel stress, which could be a concern since adhesives are vulnerable to peel stresses [16]. Finally, it was found that the ratio of the laminate Young's modulus to the adhesive shear modulus (termed in this study as the stiffness ratio) impacted the peak stresses. A lower stiffness ratio generally resulted in reduced peak stresses [38]. Similar trends were observed by reverse tapering the adherends of an SLJ [39]. The authors of this study referred to this as an inner chamfer on the adherends, and investigated the effects of chamfer height, angle, and material properties on the adhesive peak stresses and joint strength, both experimentally and when using the FEM. Unlike the previous study, the authors included a spew fillet at the end of the adhesive layer. Increasing the inner chamfer height caused a reduction of peak peel stresses. However, the peak shear stresses, although significantly reduced when compared with that with no chamfer, were relatively constant with the increased chamfer height. Increasing the chamfer angle was useful for reducing peak shear stress until reaching an optimal angle, beyond which the peak shear stresses began to increase. Interestingly, in this study, the peak peel stresses were reduced with increasing chamfer angle. It was also demonstrated that an adhesive material which had a relatively low Young's modulus did not seem to benefit from an inner chamfer, while an adhesive which had a relatively high Young's modulus benefited from increased joint strength [39].

Pre-formed angles in the adherends of an SLJ were explored as an approach to reduce applied load eccentricity [40]. In this study, SLJs with their adherends bent at various angles were subjected to tensile testing to determine joint strength. An FE model was used to determine the effect of the pre-formed angle on the adhesive layer stress distribution. It was found that a pre-formed angle of approximately 10° removed the applied load eccentricity, given the geometry used. Interestingly, a pre-formed angle of 7° showed the most significant improvement when compared to an SLJ without a pre-formed angle, resulting in a 64% increase in failure load. The joint with a pre-formed angle of 10° had a 34.5% increase in failure load, while a pre-formed angle of 15° reduced the failure load by 17.3%. Increasing the pre-formed angle also caused a reduction in the peak stresses within the adhesive layer, while the adhesive stresses at the middle of the overlap region tended to increase [40].

The influence of geometric and material properties on the dynamic characteristics of adhesively bonded SLJs were theorized using the FEM [41, 42, 43, 44]. Ko et al. studied the

effect of the adhesive overlap region length and adherend thickness on the natural frequencies of fixed-fixed SLJs [41]. The SLJ configurations considered included metal-metal bonding, metal-composite bonding, and composite-composite bonding. In general, increasing the overlap length of the SLJ caused a slight increase in the first transverse frequency for all joint configurations. The first lateral frequency initially decreased with increasing overlap length, however, when the overlap region was close to 50% of the overall beam length, it began increasing. The effect of increasing adherend thickness caused a significant increase in the transverse natural frequencies, while there were no significant changes in the lateral frequencies [41]. He and Oyadiji studied the effect of the adhesive Young's modulus and Poisson's ratio on the transverse free vibration characteristics of cantilevered SLJs [42]. A variety of Young's modulus and Poisson's ratios were considered to measure their impact on the first six natural frequencies. The Poisson's ratio of the adhesive had an insignificant impact on the modal frequencies. In addition, an increase in the adhesive Young's modulus caused an increase in all the transverse modal frequencies. However, the significance of the changes in these frequencies largely depended on whether odd or even modes of vibration were considered. Although all six transverse modes initially showed a noticeable increase in the modal natural frequencies, the odd modes showed insignificant changes in their corresponding natural frequencies once the adhesive Young's modulus was greater than 2 GPa, while the even modes continued to show significant changes. This was due to the location of the overlap region, which had been positioned on nodes and antinodes for odd and even modes of vibration respectively [42]. Therefore, one could conclude that the position of the lap joint within the bonded structure had a significant impact on its modal frequencies. In a more recent study, He investigated the effect of the adhesive material properties on the torsional free vibration characteristics of cantilevered adhesively bonded SLJs [43], and discovered that the adhesive Young's modulus and Poisson's ratio had a similar impact on the torsional modal natural frequencies, as discussed in the previous study. However, the torsional modal frequencies in this study were not impacted by the location of the overlap region within the bonded structure, therefore an increase in Young's modulus showed a significant increase for all torsional modal frequencies [43]. Kaya et al. considered the effect of the adhesive layer thickness and damping on the dynamic characteristics of cantilevered adhesively bonded SLJs [44]. The study considered in-plane vibrations, specifically the in-plane transverse and axial modes of vibration. It was shown that an increase in adhesive thickness caused a reduction in the

first six natural frequencies of the structures due to the increase in mass. The introduction of damping caused a significant reduction in the resonant frequency displacement amplitudes [44].

Non-destructive damage detection in adhesively bonded joints was performed using vibration analysis [45]. This work considered bonded SLJs subjected to six stages of incrementally increasing cyclic tensile loading to induce damage. At the completion of each stage, the corresponding natural frequencies and modal damping ratios were found for the first three modes of transverse vibration, to detect the increasing amount of damage after each stage. It was found that the natural frequencies decreased with increasing damage, showing an overall difference of 1-6% between the healthy and damaged joint condition. The modal damping ratios tended to increase with increasing damage, with a difference of 40-250% between the healthy and damaged joint condition. It was also shown that the second mode of transverse vibration was particularly sensitive to damage when compared to the first and third modes. High modal stress in regions of damage directly impacted that mode's natural frequency. To understand this behaviour, a 2D FE model was used to measure the principal stresses within the adhesive layer when the joint was subjected to impact loading. The model was first validated by comparing the predicted natural frequencies of the healthy SLJ to those of the experimental natural frequencies, which gave a maximum error of 2.5%. The adhesive principal stresses for the second mode were found to be larger than the first and third mode, which explained why the second mode was more sensitive to damage [45]. A more recent study by Du and Shi investigated the effect of cyclic-vibration-peel loading on adhesively bonded SLJs, joining aluminium and steel adherends [46]. Similar trends were found, whereby increasing load cycles tended to reduce the modal natural frequencies of the joint. For comparison, an aluminium beam with the same length as the SLJs examined was subjected to fatigue loading. In this case, the modal natural frequencies showed an increase with increasing load cycles, which indicates that the adhesive layer was the cause of the reduction in the modal natural frequencies for the SLJs. To investigate this behaviour in more detail, the authors used a 3D FE model to measure the impact of the adhesive material Young's modulus, and adhesive contact area degradation on the modal properties of the SLJ. In order to cause the observed reductions in the natural frequencies, the required Young's modulus and adhesive contact area degradation required was 99% and 80% respectively, which did not seem practical in reality. They concluded that additional studies needed to be done to further understand the cause of the modal frequency shifting observed experimentally [46]. The authors

did not consider both Young's modulus and adhesive contact area degradation simultaneously, instead considering only their individual impact. Additionally, tensile testing of the SLJ samples could be performed to determine the adhesive Young's modulus before and after exposure to cyclic-vibration-peel.

The frequency response function (FRF), natural frequencies, and modes shapes of a cantilevered adhesively bonded SLJ were investigated, both experimentally and numerically [47]. The study considered two SLJ specimens, with the specimens having a width of 25 mm and 50 mm, while the remainder of their geometry was the same. To measure the FRF, the specimens were subjected to a sinusoidal forcing function for a frequency range of 0 – 1,000 Hz. The FRFs were found for three positions along the free end of the beam, one located on each corner, and the other along the centerline of the beam. The modal frequencies given by the FE model compared well with the experiment for the first three frequencies, however a significant level of error was observed for higher modes of vibration. He explained that this discrepancy is due to the added accelerometer mass, which was not included in the FE model. This seems reasonable since the experimental modal frequencies were lower than the numerical frequencies. Deviations were found in the excitation amplitude at the natural frequencies in the FRFs, found experimentally and numerically. However, the overall trends of the FRFs were comparable. The study also presented the FRFs of three SLJ specimens with differing adhesive layer thickness. Although these were not compared to numerical results, the results matched the study conducted by Kaya et al. [44]. Specifically, increasing the adhesive thickness caused a reduction in the modal natural frequencies of the SLJ specimens [47].

1.2.2. Model Updating

Model updating has been explored as an effective approach to identify and improve uncertain modelling parameters, which had a significant impact on model performance and accuracy [48, 49, 50]. Uncertainty may arise from certain aspects of the physical structure to be modelled, which are either difficult to measure directly through experimentation, or difficult to model; for example, identifying frequency dependent properties of a non-linear material, simplification of structural details, and boundary conditions, among others [48, 49, 50]. An example of a simplification of structural detail could include a joint within the structure, as these may be difficult to model due to their relative size and aspect ratio, or the level of detail required

[51, 52, 53]. These situations were avoided by introducing modelling simplifications to represent the physical structure. These simplifications sacrifice model accuracy for a reduction in computational demand. In an attempt to preserve the model accuracy, parameters that were used to simplify the model can be tuned through model updating to ensure any model simplifications more accurately represent the physical structure. Our discussion focuses on the use of model updating to improve parameters impacting the dynamic response of a structure. This can be achieved by making use of the measured modal characteristics or FRFs of the physical structure in order to reduce numerical modelling errors [48, 49].

The use of model updating to improve the performance of an FE model was studied by Arora et al. [51, 52, 53]. The work primarily considered the dynamic behaviours of an F-shaped test structure, which was fixed at the base of the vertical member with a welded joint, while the two horizontal members were fixed to the vertical member with bolted connections. To consider these joints in an FE model, the fixed joints were taken as coincident nodes, with horizontal, vertical, and torsional spring couples. By conducting a sensitivity analysis, it was found that the torsional stiffness of the joints had the most significant impact on the dynamic behaviours of the structure. Therefore, the torsional stiffness coupling of each joint was selected as the model updating parameters [51, 52, 53]. Arora et al. compared two damped model updating approaches: a direct method and a complex parameter method [52]. Both were derived using the response function method, an iterative approach where model updating was based on the experimental FRF of the structure. Model updating by the direct method was conducted in two steps. Firstly, the mass and stiffness matrices were updated, followed by the computation of the damping matrix based on the mass and stiffness matrices, and eigendata. In the complex parameter method, the model updating parameters were considered as complex, where the real and complex parts represented the physical variable and damping of the system, respectively. The torsional stiffness couplings were updated with measured data from the F-shaped test structure. Compared to the experimentally determined FRFs, the FRFs of both FE model updating schemes showed a significant improvement over the FRFs of the FE models before updating, where the complex parameter method had slightly greater accuracy than the direct method. To investigate the robustness of the resulting updated parameters, structural modifications in the form of added mass and stiffness were performed, and the resulting experimental FRFs were compared to those found by the modified FE models. The mass and

stiffness matrices of the FE models were adjusted to suit the test structure modifications; however, the previously updated torsional stiffness couplings were used. Although the FRFs determined by both model updating approaches compared well with the measured FRFs in both cases of added mass and stiffness, the complex parameter method gave a more accurate representation than the direct method [52]. Further, Arora used an FE model updating approach based on incomplete or noisy experimental data to obtain the FRFs of the F-shaped structure [54]. Therefore, it was important to evaluate the performance of the model updating methods faced with these challenges. This paper compared two model updating approaches and presented the strengths and weaknesses of each method when incomplete or noisy experimental data was used in the model updating process [54].

Naraghi and Nobari implemented an FE model updating approach to identify frequency dependent non-linear properties of a viscoelastic adhesive material [55]. In order to determine the properties of the adhesive material, a steel beam, which underwent random excitation, was bonded to a fixed steel block to measure the FRFs of the system. The optimum equivalent linear FRF was used to extract the FRFs of the structure since the beam was subjected to random excitation. The dynamic response of the system was considered for two excitations levels: 50 mV and 700 mV. An inverse eigen-sensitivity model updating method was implemented to determine the viscoelastic properties of the adhesive material. The viscoelastic model used was a modified Maxwell model, which added a spring in parallel with a spring and dashpot in series, whose properties were determined through model updating. It was found that the FRFs of the updated FE model were in good agreement with the measured FRFs. To validate the updated material model, a second case study was conducted, which considered the dynamic response of a cantilevered SLJ. Close agreement was found between the measured and numerical FRFs for the modified beam configuration, which suggested that the updated material model was useful as a generic model for the adhesive [55]. Further research on the viscoelastic model used within the updating process was conducted by Najib et al. [56]. A total of five viscoelastic material models were considered, which include: the Hookean model, the Voigt model, the modified Maxwell model, a modified Voigt model, and the Maxwell and Voigt model connected in parallel. It was found that the modified Voigt model and the Maxwell and Voigt model connected in parallel were best suited to model the adhesive used [56].

1.2.3. Transfer Matrix Method

The TMM represents a numerical method which could be used to determine the natural frequencies and mode shapes of chain-like structures with piecewise continuous material and geometric properties, such as beams and shafts [57]. The TMM was formulated such that the structure could be divided into elements at the locations of material or geometric discontinuities. The surface states of both sides of each element (i.e. left and right) were related through a transfer matrix which when combined, yielded the global transfer matrix of the structure. The TMM was advantageous for long slender beam structures, as increasing the complexity (i.e. number of elements required) of the structure did not affect the size of the global transfer matrix, thereby reducing computational demand [58]. Additionally, the same formulation was used for an increasingly complex structure, with arbitrary material and geometric properties [59]. The TMM was originally proposed by Holzer in 1921 to predict the torsional natural frequencies and mode shapes of shafts [60]. In 1945, Myklestad applied the TMM to determine the transverse natural frequencies and mode shapes of beam structures [61]. Both Holzer and Myklestad used lumped models, which included stations and fields that represented lumped rigid masses and massless uniform elastic members respectively [62].

A computer program was developed by Subrahmanyam and Garg, which employed the TMM to determine the natural frequencies and mode shapes of beams [63]. The developed code incorporated all possible boundary conditions, and included TMM formulations based on the Euler-Bernoulli beam theory, and the Timoshenko beam theory. It also allowed for the addition of concentrated elements including lumped masses, linear springs, rotational springs, and spring supported mass. To evaluate the performance of the code, it was compared to published data and exact solutions where applicable. Detailed results were presented for some specific cases including the effects of shear deformation and rotary inertia, variable axial tension/compression and spring supports, variable mass and stiffness distribution, and determination of rigid body modes and deformation modes. The predicted natural frequencies were similar to the published data and exact solutions [63]. A more recent study, which applied the continuous mass TMM, investigated the natural frequencies and mode shapes of axial-loaded multi-step beams carrying arbitrary concentrated elements [64]. The method that was presented in this paper included a displacement function for the beam's shear deformation to simplify the formulation of the problem, and allowed classical and non-classical boundary conditions to be used. The computed

results compared well with an FE model and published data, and the effects of the concentrated elements and axial loading on the systems natural frequencies and mode shapes were investigated [64].

Boiangiu et al. studied the transverse bending vibrations of cantilever and fixed-fixed conical beams by the TMM [65]. Typically, modelling a beam with a continuously variable cross section was carried out in the TMM by introducing elements with a stepwise change in cross section [66]. However, the authors used the Euler-Bernoulli beam theory and a Bessel function in their formulation of the TMM, where the Bessel function accounted for the variable cross section over the length of the conical beam. The authors used both approaches of the TMM (i.e. TMM using a stepwise change in cross section, and TMM using a Bessel function) to compare their performance with the experimental natural frequencies of conical beams. Further, to determine the effects of using a conical beam on its dynamic characteristics, the natural frequencies were found for two beams, which had a constant circular cross section of diameters corresponding to the large and small diameter of the conical beam. While both TMM approaches gave natural frequencies that compared well with the measured natural frequencies, the TMM formulation using the Bessel function provided better results. Interestingly, the cantilever conical beam showed a significant increase in its fundamental frequency when compared to the constant cross section beams. However, this was not found for the fixed-fixed conical beam, which gave a fundamental frequency within the range of the two constant cross section beams [65].

The TMM was used to model energy harvesters with piecewise continuous material and geometric properties. Chatterjee and Bryant incorporated axial loads in the TMM for a piezo-solar energy harvesting ribbon in order to obtain transverse natural frequencies, mode shapes, and optimal piezoelectric patch coverage [58]. Wickenheiser employed the TMM to model PEHs, with arbitrary angles between discretized beam segments [59]. In these papers, material discontinuities were introduced within elements containing a piezoelectric layer mounted to the substructure, similar to the layered construction of the overlap region of an SLJ. To represent these elements, effective elemental stiffness and mass per unit length properties were determined in an additive manner [67]. However, this approach did not provide effective material properties directly.

1.2.4. Piezoelectric Energy Harvesting

Many methods have been used to investigate the performance of PEHs, including uncoupled methods, equivalent electric circuit methods, and advanced modelling analyses [68]. Lefeuvre et al. applied the uncoupled method to study the performance of piezoelectric processing circuits [69], while Shu and Lien compared the uncoupled method with simulation and experimental testing [70]. Uncoupled methods have typically been used when the electromechanical coupling of the energy harvesting device was relatively weak, such that the assumption can be made that the electromechanical coupling had an insignificant impact on the vibration amplitude of the device. The work by Shu and Lien established that the uncoupled method did not yield accurate results when the energy harvesting device had a significant electromechanical coupling [70]. The equivalent electric circuit method was studied by Yang and Tang [71], and Liu [72], to model the performance of PEHs. This method was based on the constitutive equations for piezoelectric materials. Depending on the processing circuit configuration, either the electric field or electric displacement were assumed to be insignificant, which allowed either the electric charge or voltage across the piezoelectric material to be found. However, this method typically led to an unconservative depiction of the power output of the piezoelectric energy harvesting device [68]. Advanced modelling methods were proposed by Lu et al. [73], and by Guyomar et al. [74]. Lu et al. analytically modelled the behaviours of a cantilever PEH, including the effects of the electromechanical coupling of the device. This study focused on the impact of a load resistor on power output, and the conversion efficiency of the device, which compared well with published data [73]. Guyomar et al. proposed a non-linear synchronized switch harvesting on inductor, which showed significant increases in power output of a piezoelectric device with high electromechanical coupling [74].

The method proposed by Zhu et al., the coupled piezoelectric-circuit finite element method (CPC-FEM), included a load resistor directly connected to the piezoelectric energy harvesting device, and the electromechanical coupling of the device [68]. In this paper, a cantilever bimorph piezoelectric energy harvesting device with an attached proof mass was studied to determine the effect of the load resistor on power output, on proof mass displacement amplitude, and on the system's fundamental frequency. The piezoceramics were connected both in series and in parallel configurations, and a varying load resistance was applied in the FE model, including an approximation of the short circuit and open circuit resistance (10^{-20} Ω and

10^{20} Ω respectively), and the theoretical optimal load resistance. It was shown that the load resistor had a significant impact on the current through and load across the resistor, the power output of the device, and the system's fundamental frequency. It was also observed that the displacement amplitudes of the proof mass were affected by the load resistance. Interestingly, the relationship between load resistance and proof mass displacement amplitude is complicated, and an increase in load resistance did not necessarily mean that there would be a decrease in displacement amplitude. Although the authors suggested that experimental testing needed to be conducted to validate their results, the model demonstrated the need to account for the electromechanical coupling of PEHs [68].

The geometry of a cantilever bimorph PEH with a proof mass was investigated by Gallina and Benasciutti [75]. The authors employed an FE model to compare the performance of rectangular and trapezoidal beam geometries. Four trapezoidal beam geometries were selected, including two trapezoidal beams in direct and reversed orientations, of total piezoelectric material volume equivalent to the rectangular beam geometry, and two reduced trapezoidal beams in direct and reversed orientations, with maximum width equal to the width of the rectangular beam geometry. When the maximum and minimum widths of the trapezoidal geometry were fixed and free, respectively, this was termed the direct orientation, while the opposite was termed the reversed orientation. Through simulation, it was found that there was a slight difference in the maximum power output of each geometry ranging from 5.29 μW – 5.62 μW, while the reduced reversed trapezoidal geometry resulted in the largest power output density of 0.091 $\mu W/mm^3$. The piezoelectric material strength was not considered in this study, therefore experimental testing should be conducted to verify the results [75]. Zhang et al. investigated the impact of the proof mass on the fundamental frequency, the displacement amplitude, and the open-circuit voltage of a cantilever bimorph PEH [76]. They used an analytical and an FE model to compare with experimental results. The analytical model consisted of a spring-mass-damper to represent the energy harvesting structure. The attached proof mass was incrementally increased, giving a total of six different proof mass configurations. It was found that increasing the proof mass reduced the fundamental frequency of the energy harvester, while increasing the displacement amplitude of the free end, and the maximum open-circuit voltage. The FE model depicted a more accurate representation of the experimental results compared to the analytical model. Interestingly, the ability of the analytical model to

predict the fundamental frequency and displacement amplitude with increasing proof mass became increasingly and decreasingly accurate, respectively [76]. An extensive investigation on numerically optimizing certain geometrical parameters of a cantilever PEH was conducted by Zhu et al. [77]. This study considered performance variations in current and voltage across a load resistor, power output of the device, displacement amplitude of the proof mass, and resonant frequencies, due to variations in beam length and width, piezoelectric layer thickness, mass length, width, and height. Output performance was evaluated at the resonant frequency with impedance matched resistance. The FE model employed was similar to the model presented in [68] with modifications to the device geometry. Many relationships and recommendations in the pursuit of an optimal energy harvesting device were presented, which will not be repeated here for brevity [77].

Berdy et al. proposed a novel meandering PEH [78]. In order to reduce the fundamental frequency, the length of the beam and proof mass were typically increased, however, this may not be feasible due to the relatively small size of the PEH used for electronics and sensor nodes. The proposed meandering energy harvester featured a fixed-fixed S-shaped design, which effectively increased the length of the beam, while maintaining a relatively small footprint. Due to the design of the energy harvester, some portions of the beam were in positive and negative strain when vibrating at the fundamental mode, which caused voltage cancellation. Two methods were compared to avoid voltage cancellation, namely the strain-matched electrode, and the strain-matched polarization. The former used electrode disconnects at the location of strain nodes, such that positive and negative strain beam segments were separated, while the latter method involved a change in polarity of either the positive or negative strain beam segments, so the entire structure had the same polarity during energy harvesting. To demonstrate the advantage of the meandering energy harvester, three additional energy harvesters were investigated with FE models, including a long fixed-fixed beam with length equal to the effective length of the meandering energy harvester, which had a proof mass at the center of the beam, a straight fixed-fixed beam and a cantilever beam with the same footprint as the meandering energy harvester, and proof mass at the center and the free end of the beam, respectively. Out of these three, only the long fixed-fixed beam achieved a low fundamental frequency of 19.9 Hz; however, its length was deemed unsuitable for the application. The performance of the meandering energy harvester was compared between the single electrode (voltage cancellation),

the strain-matched electrode, and the strain-matched polarization, for several parameters through both an FE model and experimental testing. It was found that the FE model gave comparable results to the experimental results. Overall, the strain-matched polarization method yielded the most favoured power output and power density of 118 μW and 0.20 μW/mm^3, respectively. The strain-matched electrode method gave slightly inferior power output and density of 105 μW and 0.18 μW/mm^3, respectively, while the single electrode gave the least desired performance of 5.5 μW and 0.026 μW/mm^3, respectively, due to voltage cancellation. In terms of manufacturing cost, the single electrode device was the least costly, whereas the strain-matched polarization device was the most expensive [78].

1.3. Objectives and Contributions

This research intends to use the FEM to investigate the static and dynamic behaviours of discontinuous beam structures with a focus on its ability to model systems that require single physics (i.e. static and dynamic behaviours of an SLJ), as well as multi-physics (i.e. dynamic behaviours of a PEH). The FE software used throughout the work is Comsol Multiphysics. The TMM is employed as an alternative to determine the natural frequencies and mode shapes of an SLJ. Due to the layered construction of the SLJ overlap region, a single variable model updating approach will be used with the TMM to determine its effective Young's modulus. This is done to attain improved results when compared to the effective Young's modulus determined by a commonly used additive approach. Numerical results are compared with analytical and experimental data, where available, to validate their use. Important relationships impacting the dynamic characteristics of the SLJ, including the geometry of the joints and material properties, are discussed. These insights are useful in the design and application of adhesively bonded SLJs in industry.

In the study by He [47], the FRF was measured with an accelerometer, which added mass to the structure. Since the mass of the structure is related to its dynamic behaviours, unavoidable errors were introduced during data collection. The objective is to determine the dynamic characteristics of the specimens without introducing additional mass. To remedy this issue, this research presents an experimental approach which uses optical position sensors to measure the transmissibility ratio (TR) of SLJ specimens. Therefore, the dynamic characteristics of the specimens tested are unaffected by the additional mass of the accelerometers. In this way, the

experimental results illustrate a more accurate representation of the SLJ specimens considered, which allows for the development of more accurate numerical models. The developed experimental apparatus is also used to measure the dynamic behaviours of the PEH devices.

1.4. Thesis Outline

The remainder of this thesis is organized as follows: Chapter 2 presents the static single physics study, modelling the stress distributions within the adhesive layer of an adhesively bonded SLJ subjected to tensile loading. The analytical models used to validate the FE model are presented, including a brief discussion of their assumptions used in their derivation. Different mesh schemes are applied in the FE models to determine which of them best represents the stress distributions within the adhesive layer. In Chapter 3, we consider the dynamic single physics study of a cantilevered adhesively bonded SLJ subjected to harmonic base excitation. Both the FE model and TMM model are discussed in detail. Improvement of the TMM is presented, for the determination of effective material properties of a bimorph structure. Chapter 4 details the experimental apparatus developed to measure the dynamic behaviours of the SLJ beams. The experimental apparatus is employed to collect experimental data in order to validate the numerical models presented in Chapter 3. Chapter 5 focuses on a cantilevered PEH, which is modelled numerically with a dynamic multi-physics FE model. The effect of adding mass to the free end of the PEH is investigated, and the performance of the two configurations are compared. Chapter 6 provides concluding remarks for the research, along with suggestions for future work.

Chapter 2 Adhesive Single Lap Joint Subjected to Static Loading

We begin our investigation by modeling an adhesive bonded SLJ subjected to static loading and single physics. This scenario is common amongst engineering designs, and provides a foundation for more complicated loading and physics applications. The ability to model the behaviour of the adhesive material within an adhesive bonded joint, subjected to tensile loading is important in design, and leads to useful insights to understand how the adhesive carries the applied load. Typically, adhesive materials are weaker than the adherends they join, and are critical to the joint's structural integrity. Thus, it is necessary to develop models which accurately depict the stress within the adhesive material of an adhesive bonded joint subjected to a static load, to ensure the material can withstand the required operating loads.

This chapter focuses on the development of FE models using different modeling strategies, which are discussed in detail, to determine the most suitable modelling approach to investigate the stress distribution within the adhesive layer of an adhesive bonded SLJ. The FEM is an approach which can be used to model more complex bond line geometries than the closed-form analytical methods discussed in Section 1.2.1.1 (i.e. shear-lag, Goland and Reissner, and Hart-Smith methods). These analytical methods are suitable for adhesive bonded SLJs; however, they cannot be used for larger assemblies with increasingly complex bond line geometries. The closed-form analytical methods are used to evaluate the performance of the FE models. Experimental tensile testing results are also presented for the adhesive material used in the construction of the adhesive bonded SLJs subjected to dynamic loading in Chapter 3: Dinitrol 501 FC HM.

The adhesive stress distributions found by the FE models are compared with the analytical models of Volkersen, Goland and Reissner, and Hart-Smith. The SLJ specimen used in this chapter is constructed of aluminum adherends, bonded by an adhesive material found in Table 2.1 which was selected from the following study [42]. The geometry of the SLJ specimen is shown in Figure 2.1. The thickness of the adhesive layer is varied from 0.1 mm – 0.5 mm, with a step size of 0.2 mm, with a fixed applied load of 500 N since the adhesive thickness has a significant impact on the stress distribution within the adhesive layer. All remaining parameters remain fixed.

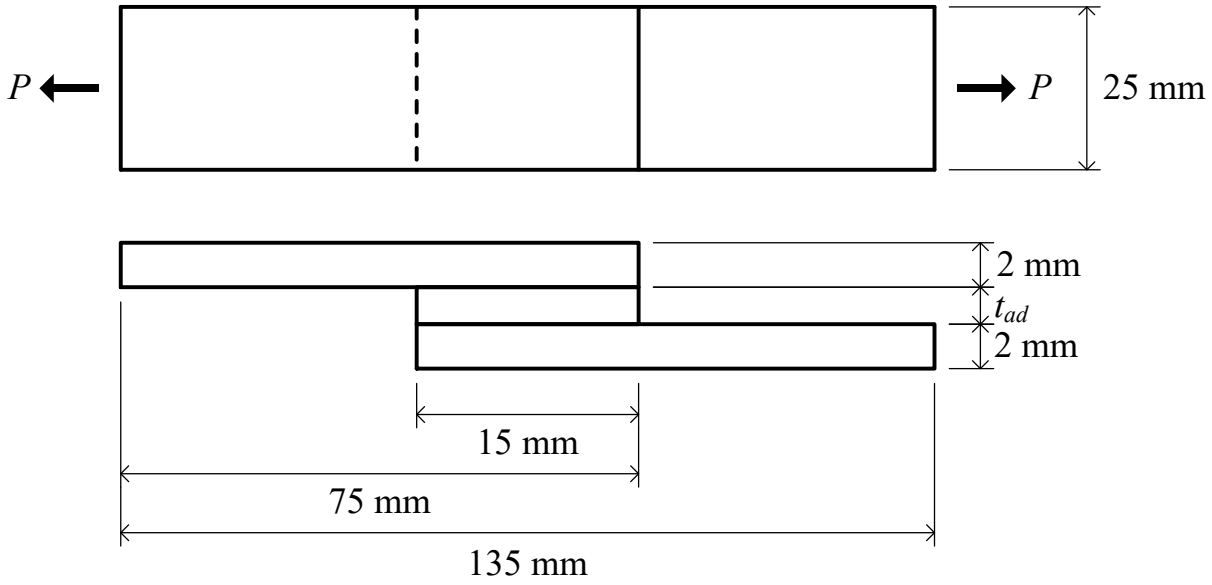

Figure 2.1: Static SLJ specimen geometry (not drawn to scale)

Table 2.1: Static SLJ specimen material properties

Adherend Young's Modulus, E	70 GPa
Adherend Density, ρ	2,700 kg/m^3
Adherend Poisson's Ratio, v	0.33
Adhesive Young's Modulus, E_{ad}	7 GPa
Adhesive Density, ρ_{ad}	1,200 kg/m^3
Adhesive Poisson's Ratio, v_{ad}	0.40

2.1. Analytical Models of Stress Distribution

2.1.1. Volkersen's Shear-Lag Model

The Volkersen shear-lag model is the first known analytical method to model the shear stress distribution within an adhesive bonded SLJ. This model introduces the concept of differential shear within the overlap region of the SLJ. Thus, when the SLJ is subjected to a tensile load, the resulting shear stress within the adhesive material varies along the overlap length of the joint. This results in a shear stress distribution with a relatively large and small gradient near the ends and the middle of the overlap region, respectively. As mentioned in Section 1.2.1.1, it is assumed that the adherends deform in tension only, therefore the adhesive material experiences a state of pure shear stress, which can be seen in Figure 2.2(b). The

resulting shear stress distribution within the adhesive material is found in [27] as a ratio of the average shear stress as follows:

$$\frac{\tau}{\tau_{av}} = \frac{\omega \cosh(\omega X)}{2\sinh\left(\omega/2\right)} + \left(\frac{t_t - t_b}{t_t + t_b}\right)\frac{\omega \sinh(\omega X)}{2\cosh\left(\omega/2\right)} \tag{2.1}$$

where,

$$\tau_{av} = \frac{P}{b l_{ad}} \tag{2.2}$$

$$\omega = \sqrt{\frac{G_{ad} l_{ad}^2}{E t_t t_{ad}}\left(1 + \frac{t_t}{t_b}\right)} \tag{2.3}$$

$$X = \frac{x}{l_{ad}} \tag{2.4}$$

In equations (2.1) to (2.4), τ and τ_{av} are the adhesive shear stress distribution and average adhesive shear stress respectively, P is the applied axial load, the inverse of ω is called the characteristic shear-lag distance, x is the position within the overlap region, and G_{ad} and E represent the adhesive shear modulus and adherend Young's modulus respectively. The geometric parameters are shown in Figure 2.2(a), where t_t and t_b, represent the thickness of the top and bottom adherend respectively, t_{ad} represents the adhesive thickness, and b and l_{ad} represent the joint width and overlap region length respectively.

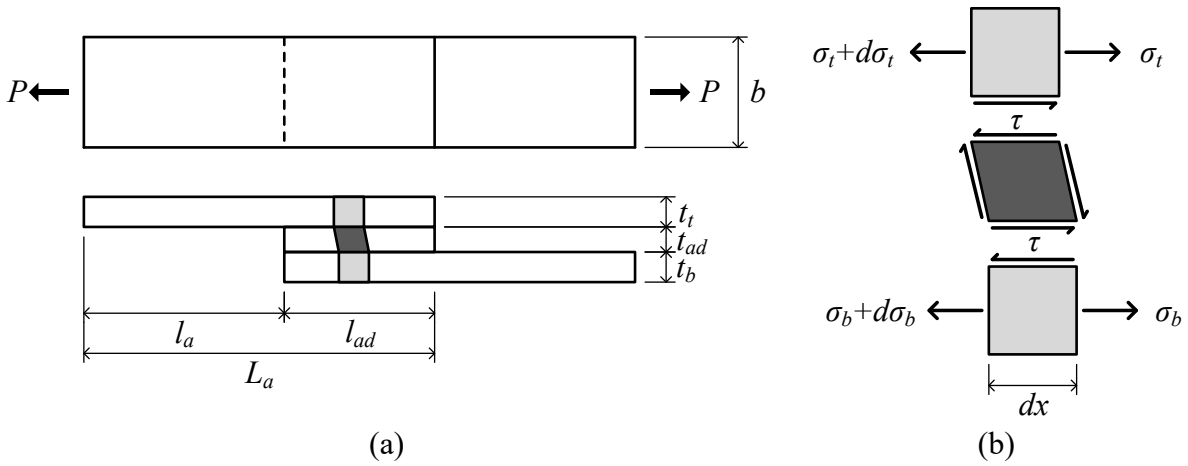

Figure 2.2: SLJ subjected to static loading: (a) geometric parameters; (b) elemental diagram

Observations about the relationship between the joint geometry and the resulting shear stress distribution can be made for the shear-lag model. From equation (2.1) it can be seen that the thickness of the adherends has a significant impact on the shape of the shear stress distribution. If, for example, the top and bottom adherend are the same thickness, then the resulting shear stress distribution is symmetric, whereas if they are not equal, the shear stress distribution is not symmetric. Also, the maximum shear stress within the adhesive is significantly reduced when the adherends are of equal thickness [32]. Figure 2.3 shows the typical shape of the shear stress distribution given by the shear-lag model for these two cases. The shear stress distributions are normalized based on the maximum shear stress determined by the case where the adherends have an unequal thickness, to illustrate the reduction in the maximum shear stress when equal adherend thicknesses are used. When the adherend thicknesses are not equal, the maximum shear stress is located at the end with the thinner adherend. This phenomenon is likely due to the differential deformation of the adherends. Since the thinner adherend experiences more axial deformation in the overlap region, the shear stress is increased.

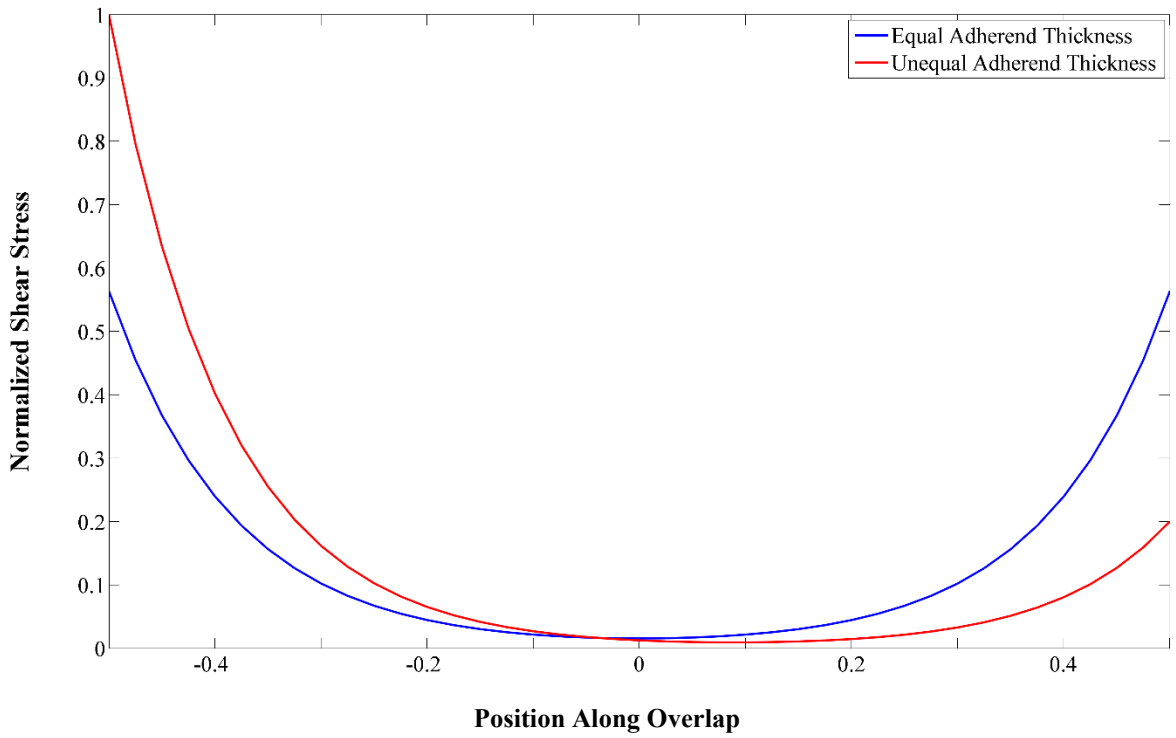

Figure 2.3: Example of typical shear-lag adhesive shear stress distributions

2.1.2. Goland and Reissner Model

The first to include the effects of bending in the adherends due to the eccentric load path is Goland and Reissner. The model builds from the shear-lag model, by including bending in the adherends due to the eccentric load path of the SLJ. The assumption is made that the adherends are of equal thickness ($t_t = t_b = t$). To determine the shear and peel stress distributions within the adhesive layer, the solution was divided in two parts. First the load acting on the ends of the overlap area is found using finite deflection theory, then the resulting shear and peel stress distributions within the adhesive layer are solved [79], as shown in Figure 2.4. As mentioned in Section 1.2.1.1, bending moment and transverse force factors are used to relate the applied tensile load to the bending moment and transverse forces within the SLJ. The bending moment and transverse force factors are at unity for low tensile loads, and decrease with increasing load, since the effective load eccentricity reduces with increasing load [27], as can be seen in Figure 1.2(a) and Figure 1.2(b) from Section 1.2.1. The Goland and Reissner adhesive shear stress distribution is as follows [80]:

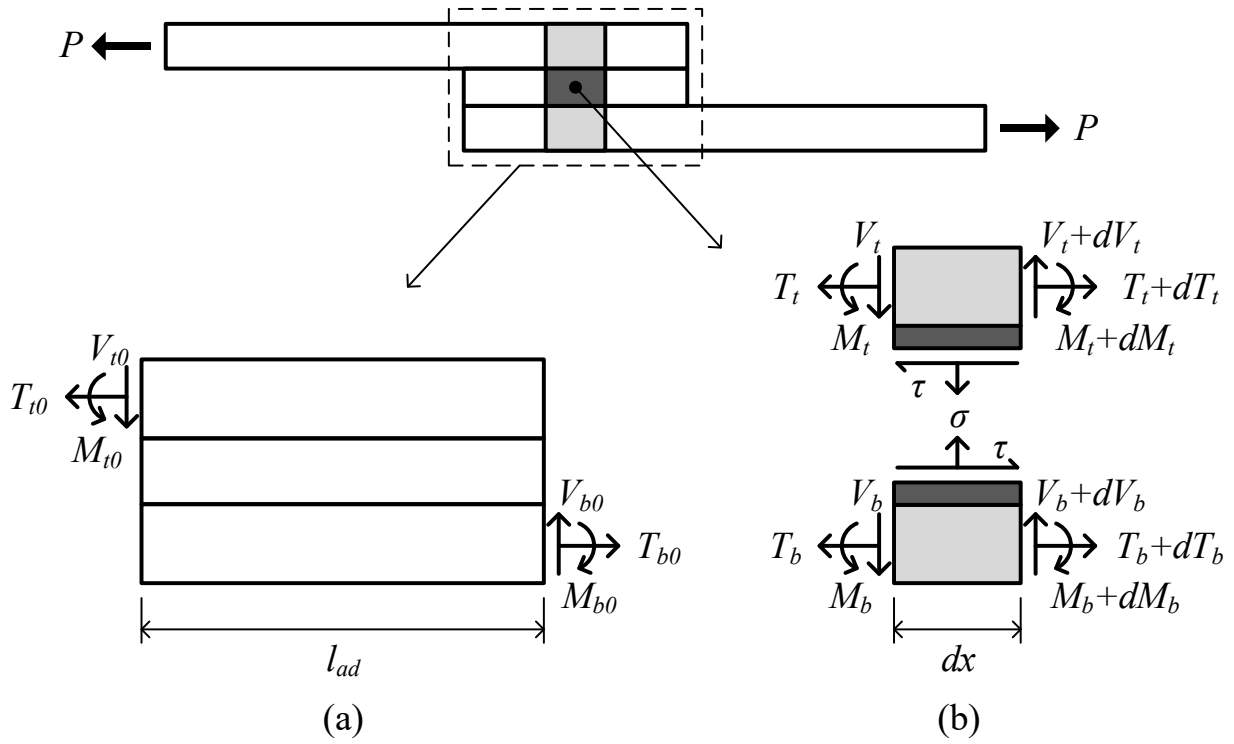

Figure 2.4: Goland and Reissner method: (a) overlap end loading; (b) differential element within overlap region

$$\frac{\tau}{\tau_{av}} = \frac{1}{4}\left[\frac{\beta l_{ad}}{2t}(1+3k)\frac{\cosh\left(\frac{\beta x}{t}\right)}{\sinh\left(\frac{\beta l_{ad}}{2t}\right)} + 3(1-k)\right] \tag{2.5}$$

where,

$$k = \frac{\cosh\left(\frac{u_2 l_{ad}}{2}\right)}{\cosh\left(\frac{u_2 l_{ad}}{2}\right) + 2\sqrt{2}\sinh\left(\frac{u_2 l_{ad}}{2}\right)} \tag{2.6}$$

$$u_2 = \sqrt{\frac{3(1-\nu^2)P}{2t^3 bE}} \tag{2.7}$$

$$\beta^2 = 8\frac{G_{ad}t}{Et_{ad}} \tag{2.8}$$

In equations (2.5) to (2.8), *k* represents the bending moment factor, and *v* represents the Poisson's ratio of the adherend. The remaining terms are the same as those used in the shear-lag model. The Goland and Reissner adhesive peel stress distribution is as follows [80]:

$$\sigma = \frac{4Pt}{\Delta b l_{ad}^2}\left[\left(R_2\lambda^2\frac{k}{2}+\lambda k'\cosh(\lambda)\cos(\lambda)\right)\cosh\left(\frac{2\lambda x}{l_{ad}}\right)\cos\left(\frac{2\lambda x}{l_{ad}}\right) + \left(R_1\lambda^2\frac{k}{2}+\lambda k'\sinh(\lambda)\sin(\lambda)\right)\sinh\left(\frac{2\lambda x}{l_{ad}}\right)\sin\left(\frac{2\lambda x}{l_{ad}}\right)\right] \tag{2.9}$$

where,

$$k' = \frac{kl_{ad}}{2t}\sqrt{3\left(1-\nu^2\right)\frac{P}{tbE}} \tag{2.10}$$

$$\lambda = \frac{l_{ad}}{2t}\left(6\frac{E_{ad}t}{Et_{ad}}\right)^{1/4} \tag{2.11}$$

$$\Delta = \frac{1}{2}\left(\sin(2\lambda)+\sinh(2\lambda)\right) \tag{2.12}$$

$$R_1 = \sinh(\lambda)\cos(\lambda)+\cosh(\lambda)\sin(\lambda) \tag{2.13}$$

$$R_2 = \sinh(\lambda)\cos(\lambda)-\cosh(\lambda)\sin(\lambda) \tag{2.14}$$

where, *k'* is the transverse force factor, and E_{ad} is the Young's modulus of the adhesive material.

Since it is assumed that the thickness of the top and bottom adherends is the same, the Goland and Reissner method gives symmetric shear and peel stress distributions. The typical shape of the shear and peel stress distributions can be seen in Figure 2.5. The shear stress distribution is similar to the shear-lag model. It can be seen that the peel stress distribution is in tension, and is largest in magnitude near the ends of the overlap region, while the distribution becomes compressive near the center of the overlap region.

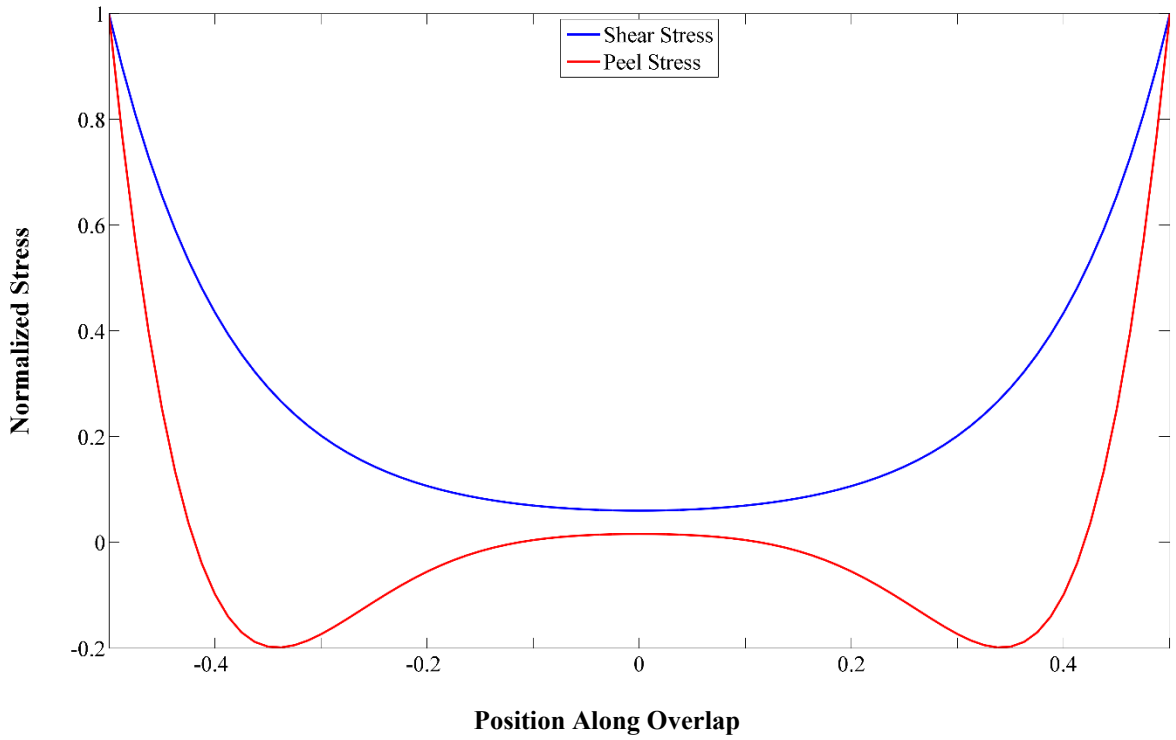

Figure 2.5: Example of typical Goland and Reissner adhesive stress distributions

2.1.3. Hart-Smith Model

The Hart-Smith model builds from the shear-lag and Goland and Reissner models. This model introduces modifications to the bending moment and shear force factors used in the Goland and Reissner model. These are found in the Goland and Reissner model by assuming the overlap region deforms as a single block, while the Hart-Smith model considers the deformation of the top and bottom adherends separately [27]. Adhesive plasticity is included in the Hart-Smith model, assuming that the adhesive materials behaviour is elastic-perfectly plastic as can be seen in Figure 2.6(a). Thus, the regions of the adhesive material which have yielded have constant stress with increasing strain. Due to the typical shape of the stress distributions, shown in the shear-lag and Goland and Reissner methods, yielding commences at the overlap ends of the joint, and moves towards to middle of the joint with increasing load as can be seen in Figure 2.6(b). This study considers low load applications, within the elastic region of the adhesive material, such that the shear-lag, Goland and Reissner, and Hart-Smith models can be used for validation of the numerical model. Thus, the Hart-Smith model for the plastic deformation is not

considered in this work. The reader is encouraged to find these details in [32]. The Hart-Smith shear stress distribution for the adhesive material is as follows [32]:

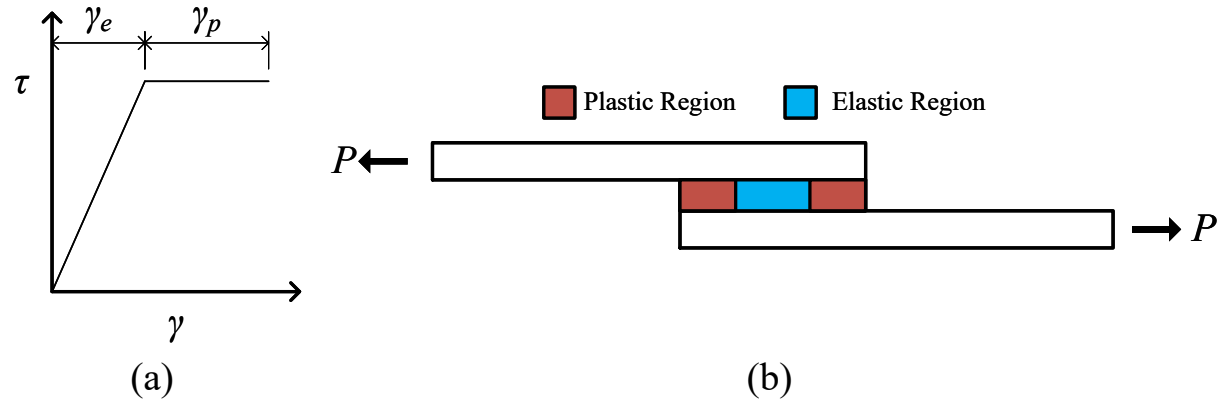

Figure 2.6: Hart-Smith Model: (a) elastic-perfectly plastic shear stress strain relationship; (b) plastic and elastic deformation of the adhesive

$$\tau = A_2 \cosh\left(2\lambda' x\right) + C_2 \tag{2.15}$$

where,

$$\lambda' = \sqrt{\left[\frac{1+3\left(1-\nu^2\right)}{4}\right]\frac{2G_{ad}}{t_{ad}Et}} \tag{2.16}$$

$$A_2 = \frac{G_{ad}}{t_{ad}Et}\left[\frac{P}{b} + \frac{6\left(1-\nu^2\right)M}{t}\right]\frac{1}{2\lambda'\sinh\left(\lambda' l_{ad}\right)} \tag{2.17}$$

$$C_2 = \frac{1}{l_{ad}}\left[\frac{P}{b} - \frac{A_2}{\lambda'}\sinh\left(\lambda' l_{ad}\right)\right] \tag{2.18}$$

$$M = \frac{P}{b}\left(\frac{t+t_{ad}}{2}\right)\frac{1}{1+\frac{\xi l_{ad}}{2}+\left(\frac{\xi^2 l_{ad}^2}{24}\right)} \tag{2.19}$$

$$\xi^2 = \frac{P}{bD} \tag{2.20}$$

$$D = \frac{Et^3}{12\left(1-\nu^2\right)} \tag{2.21}$$

In equations (2.15) to (2.21), M represents the bending moment, and D represents the bending stiffness of the adherend. The remaining terms are the same as those used in the shear-lag model and Goland and Reissner method. The Hart-Smith adhesive peel stress distribution is as follows [32]:

$$\sigma = A\cosh(\chi x)\cos(\chi x) + B\sinh(\chi x)\sin(\chi x) \tag{2.22}$$

where,

$$A = -\frac{E_{ad}M\left(\sin(\chi x)-\cos(\chi x)\right)}{t_{ad}D\chi^2 e^{\chi c}} \tag{2.23}$$

$$B = \frac{E_{ad}M\left(\sin(\chi x)+\cos(\chi x)\right)}{t_{ad}D\chi^2 e^{\chi c}} \tag{2.24}$$

$$\chi = \left(\frac{E_{ad}}{2Dt_{ad}}\right)^{\frac{1}{4}} \tag{2.25}$$

The general shape of the Hart-Smith adhesive shear and peel stress distributions are similar to the Goland and Reissner method. The main difference is the actual magnitudes of the distributions. Thus, the general shape of the shear and peel stress distributions of the Hart-Smith method are not shown in this section.

2.2. Finite Element Model

Developing an accurate and efficient FE model for the SLJ geometry presents a challenge. Beam structures typically have a long slender geometry, which means their aspect ratio is poor. In the FEM, these structures can be modelled using beam elements, which give good accuracy and computational efficiency. However, the geometry of an SLJ is more complicated than a beam structure, since it contains material and geometric discontinuities. Therefore, it is not suitable to model an SLJ using beam elements. This presents a challenge in developing an FE model, as the quality of the elements used has a significant impact on the accuracy of the model, while the number of elements has a significant impact on the

computational demand [4, 35]. For example, the most desired aspect ratio for 2D quadrilateral elements is unity, whereby the element is a square shape having sides of equal length. Thus, there exists a trade off between model accuracy and computational efficiency, by using many elements with a desirable aspect ratio, or less elements having a poor aspect ratio respectively. Another challenge in using the FEM to model the SLJ geometry is the presence of high stress gradients and stress singularities at the corners of the adhesive region. This is addressed by using appropriate mesh refinement near the ends of the overlap region of the adhesive [81].

Certain modelling simplifications can be used to preserve accuracy, while minimizing computational demand. Firstly, the closed-form analytical methods assume that the stress distribution is constant through the width of the adhesive material; therefore, the FE models developed below are 2D. Reducing the 3D geometry of the SLJ to a 2D FE model presents a significant reduction in computational demand, without sacrificing the accuracy of the stress distribution within the adhesive material. Secondly, the stresses present within the adherends are not the primary focus of the analysis, therefore element quality within the adherends can be sacrificed to reduce computational demand further.

Three FE models are developed below, which include various modeling simplifications and strategies are used to model the adhesive SLJ. The performance of these models is compared with the analytical models to determine which modeling strategies give the most appropriate adhesive stress distribution results for the static loading scenario. The general geometry of the FE models is shown in Figure 2.7. All models employ a stationary study, using the solid mechanics module. Each model is discussed in detail below.

Figure 2.7: Geometry of the static SLJ FE model

2.2.1. Static Single Lap Joint Model 1 Mesh

This model was developed using the default mesh generation tool in Comsol Multiphysics. The software attempts to generate a computationally lightweight mesh, with predefined element densities ranging from extremely coarse to extremely fine. Further mesh

refinement is achieved by defining custom element size parameters. Figure 2.8 shows the Static SLJ Model 1 overlap region mesh, and a detailed view of the elements used in the adhesive layer. Since the stress distribution within the adhesive material is to be found, the adhesive layer has a custom mesh density which is finer than the predefined mesh densities, while the adherends have a normal mesh density.

Comsol Multiphysics includes an element quality index which gives useful details about the elements used in the FE model. The element quality ranges from 0 to 1, representing poor element quality and most desired element quality respectively. The element quality mainly depends on the element shape, and aspect ratio. Since the adhesive layer thickness is varied, only the element quality index for an adhesive thickness of 0.5 mm is shown. For this FE model, 3,826 triangular elements are used with an average element quality is 0.9477.

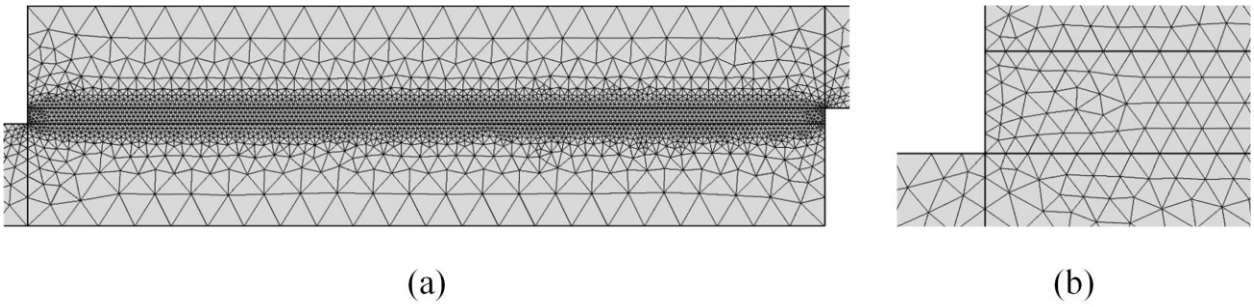

Figure 2.8: Static SLJ Model 1 Mesh: (a) overlap region mesh; (b) detail of the adhesive layer mesh

2.2.2. Static Single Lap Joint Model 2 Mesh

The mesh used for the adhesive layer in this model is user-defined, and does not use the default mesh tools. However, the adherends are meshed using the default mesh: a normal mesh density. The default mesh tool automatically ensures continuity of elements at the interface between the adhesive region and the adherends, regardless of the defined mesh density. The elements selected for the adhesive layer are quadratic quadrilateral elements, which are widely used in the FEM due to their high accuracy. When rectangular in shape, the quadratic quadrilateral element can accurately represent all states of pure bending and constant strain [82].

The FE mesh for this model can be seen in Figure 2.9. Along the length, width, and height of the adhesive layer, 60, 20, and 5 elements are used respectively. The elements along

the length of the overlap are distributed such that there are more elements per unit length near the ends of the adhesive layer, than in the middle. This better represents the stress distribution closer to the ends, where higher stress gradients are typically located. This is also beneficial to avoid stress singularities near the ends of the overlap region [81]. For this FE model, 2,818 triangular elements, and 720 quadratic quadrilateral elements are used with an average element quality is 0.9142. This results in a total of 3,538 elements, which represents a reduction in computational demand compared with Model 1, while maintaining a satisfactory element quality.

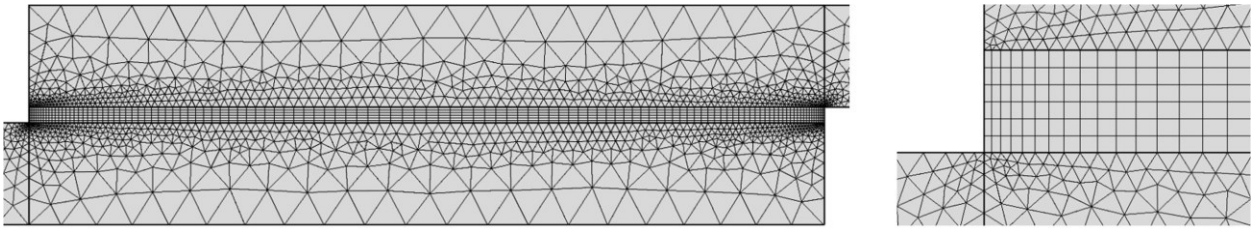

Figure 2.9: Static SLJ Model 2 Mesh: (a) overlap region mesh; (b) detail of the adhesive layer mesh

2.2.3. Static Single Lap Joint Model 3 Mesh

This model uses the thin elastic layer boundary condition to represent the adhesive layer of the SLJ. The thin elastic layer is appropriate for domains with large aspect ratios. For interior boundaries, the displacements between the two sides of the boundary are decoupled. They are then connected by elastic and viscous forces, equal in magnitude, but opposing in direction, proportional to the relative displacements and velocities. With the contact surface area held constant, the thin elastic layer boundary condition tends to be more accurate with decreasing thickness, and less accurate with increasing thickness. Using this boundary condition, the adhesive layer needs not be explicitly modelled, which reduces the number of elements in the model mesh, thus reducing computational demand. The thin elastic layer is applied between the overlap surfaces between the two adherends as shown in Figure 2.10. The adherends are meshed using the predefined mesh tools as a normal mesh density. The normal and tangential spring constant per unit volume (k_n and k_t respectively) can be estimated as follows:

$$k_n = \frac{E_{ad}\left(1-\nu_{ad}\right)}{t_{ad}\left(1+\nu_{ad}\right)\left(1-2\nu_{ad}\right)} \tag{2.26}$$

$$k_t = \frac{G_{ad}}{t_{ad}} \tag{2.27}$$

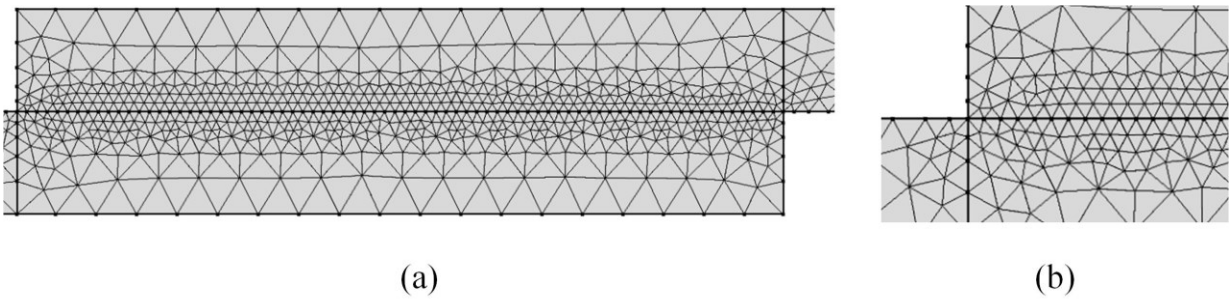

Figure 2.10: Static SLJ Model 3 Mesh: (a) overlap region mesh; (b) detail of the adhesive layer mesh

Since the adhesive layer is represented by the thin elastic layer boundary condition, the mesh quality and number of elements used is fixed. For this FE model, 1,602 triangular elements are used with an average element quality is 0.9261. The represents a significant reduction in computational demand compared to Models 1 and 2, while maintaining a good average element quality.

2.2.4. Boundary Conditions

Appropriate physical constraints were used in order to simulate a tensile test, which can be seen in Figure 2.11. Firstly, the free end of the top adherend is fixed, while a boundary load is applied on the free end of the bottom adherend, which represents the axial tension applied in a tensile test. Each of the FE models above have an extended grip length of 25 mm, beyond the length of the adherends outlined in Figure 2.1. This grip length portion of each of the adherends is constrained by a roller support such that this portion can be displaced in the axial direction only. Roller constraints are necessary, as without them, the boundary load creates a moment about the fixed end of the test specimen, inducing large bending stresses in the bottom adherend, which is not representative of a tensile test. By applying the roller constraints, bending occurs in the extension and overlap portions of both the adherends due to the eccentricity created by the load path, as described in Section 1.2.1.

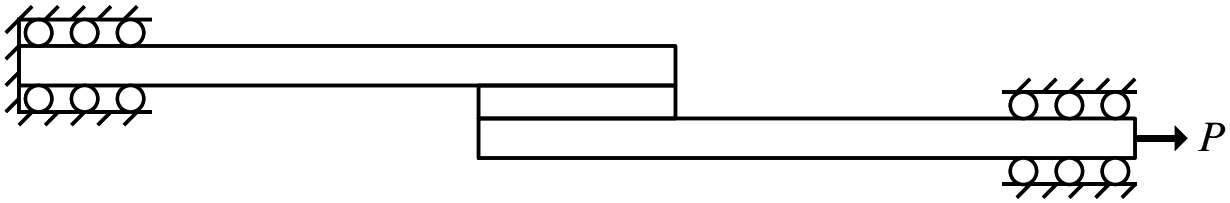

Figure 2.11: Boundary conditions of the FE models

2.2.5. Post-Processing

Since the analytical methods assume that the shear and peel stresses are constant through the thickness of the adhesive, the adhesive shear and peel stress distributions are evaluated at the midline of the adhesive layer. The red line in Figure 2.12 represents the location of the 2D cutline used to evaluate the stress distribution. From the FE model, the xy- and y-components of stress along the 2D cutline represent the adhesive shear and peel stress distributions respectively. Since the adhesive layer of Model 3 is represented by the thin elastic layer boundary condition, the 2D cutline is placed at the interface of the top and bottom adherends.

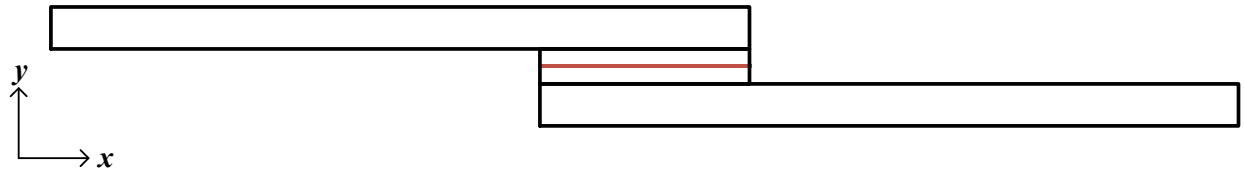

Figure 2.12: Location of the FE 2D cutline

2.3. Finite Element Model Evaluation

The shear and peel stress distributions from the analytical and FE models for an adhesive thickness of 0.1 mm are shown in Figure 2.13 to Figure 2.15. Since the analytical models are used to evaluate the performance of the FE models, their shear and peel stress distributions are plotted in each figure, while Figure 2.13 to Figure 2.15 show the distributions for Models 1 to 3 respectively. The average of the analytical models is also plotted for comparison with the FE models, and the maximum shear and peel stress of the analytical average and each of the FE models are tabulated in Table 2.2 to Table 2.4, along with the associated error.

From Figure 2.13 it can be seen that while the Goland and Reissner, and Hart-Smith stress distributions are in close agreement, the shear stress distribution of the shear-lag model differs significantly for an adhesive thickness of 0.1 mm. In particular, the maximum shear stress from the shear-lag model is found to be 19.36 MPa, while the Goland and Reissner, and Hart-Smith models give 10.94 MPa and 10.81 MPa respectively. This results in an average maximum shear stress of 13.70 MPa. The Goland and Reissner, and Hart-Smith maximum peel stresses are 15.43 MPa and 14.93 MPa respectively, giving an average max peel stress of 15.18 MPa.

Comparing the FE model results from Figure 2.13 to Figure 2.15 shows that Models 1 and 2 compare well with the average analytical stress distributions, while Model 3 shows noticeable irregularities in the shear and peel stress distributions. The shear and peel stress distributions of Model 3 are not smooth near the ends of the overlap region, unlike the analytical models which are smooth throughout. The reason for this can be attributed to the use of the thin elastic layer boundary condition, since it is used to decouple the displacements between the two sides of the boundary. Model 3 also gives a significant amount of error in the maximum shear stress for all adhesive thicknesses, and the peel stress for an adhesive thickness of 0.1 mm, as seen in Table 2.4. For these reasons, Model 3 does not adequately represent the behaviour of an adhesive bonded SLJ subjected to static loading.

Although Models 1 and 2 compare well with the analytical models, Model 2 has a few subtle advantages. Figure 2.13(a) shows that the adhesive shear stress distribution of Model 1 has poor symmetry, whereas the analytical results give symmetric distributions. Figure 2.14(a), on the other hand, shows that the adhesive shear stress distribution of Model 2 has better symmetry. Model 2 accurately represents the adhesive shear stress free boundary condition at the ends of the overlap region [83, 84], as the shear stress tends to zero. Although Model 1 shows a reduction in shear stress near the ends of the overlap region, the shear stress is found to be approximately 6.5 MPa. This represents a significant drawback in the classical analytical models. From Table 2.2 and Table 2.3, Model 2 gives favourable results for the maximum adhesive peel stresses for all thicknesses when compared with Model 1, while Model 1 gives slightly better maximum adhesive shear stresses for adhesive thicknesses of 0.1 mm and 0.3 mm. Finally, Model 2 is more computationally efficient than Model 1, using a total of 3,538 elements

compared to 3,826 elements in Model 1. Therefore, Model 2 is selected as the most suitable FE model to represent the behaviour of an adhesive bonded SLJ subjected to static loading. For brevity, only the remaining adhesive stress distributions for Model 2 are shown in the remainder of this section. The reader is directed to Table 2.2 and Table 2.4 for the additional data from Models 1 and 3 for adhesive thicknesses of 0.3 mm and 0.5 mm.

Table 2.2: Model 1 maximum stress and error

Adhesive Thickness (mm)	Max Average Analytical Shear Stress (MPa)	Max Average Analytical Peel Stress (MPa)	Max FE Shear Stress (MPa)	Max FE Peel Stress (MPa)	Max Shear Stress Error (%)	Max Peel Stress Error (%)
0.1	13.70	15.18	10.42	17.36	-23.93	14.41
0.3	6.58	9.20	6.29	10.11	-4.33	9.86
0.5	4.86	7.46	5.03	6.98	3.56	-6.39

Table 2.3: Model 2 maximum stress and error

Adhesive Thickness (mm)	Max Average Analytical Shear Stress (MPa)	Max Average Analytical Peel Stress (MPa)	Max FE Shear Stress (MPa)	Max FE Peel Stress (MPa)	Max Shear Stress Error (%)	Max Peel Stress Error (%)
0.1	13.70	15.18	9.90	15.74	-27.76	3.72
0.3	6.58	9.20	6.18	8.90	-6.00	-3.23
0.5	4.86	7.46	5.02	7.04	3.42	-5.56

Table 2.4: Model 3 maximum stress and error

Adhesive Thickness (mm)	Max Average Analytical Shear Stress (MPa)	Max Average Analytical Peel Stress (MPa)	Max FE Shear Stress (MPa)	Max FE Peel Stress (MPa)	Max Shear Stress Error (%)	Max Peel Stress Error (%)
0.1	13.70	15.18	8.13	13.84	-40.66	-8.82
0.3	6.58	9.20	5.62	9.91	-14.59	7.67
0.5	4.86	7.46	4.59	8.18	-5.54	9.68

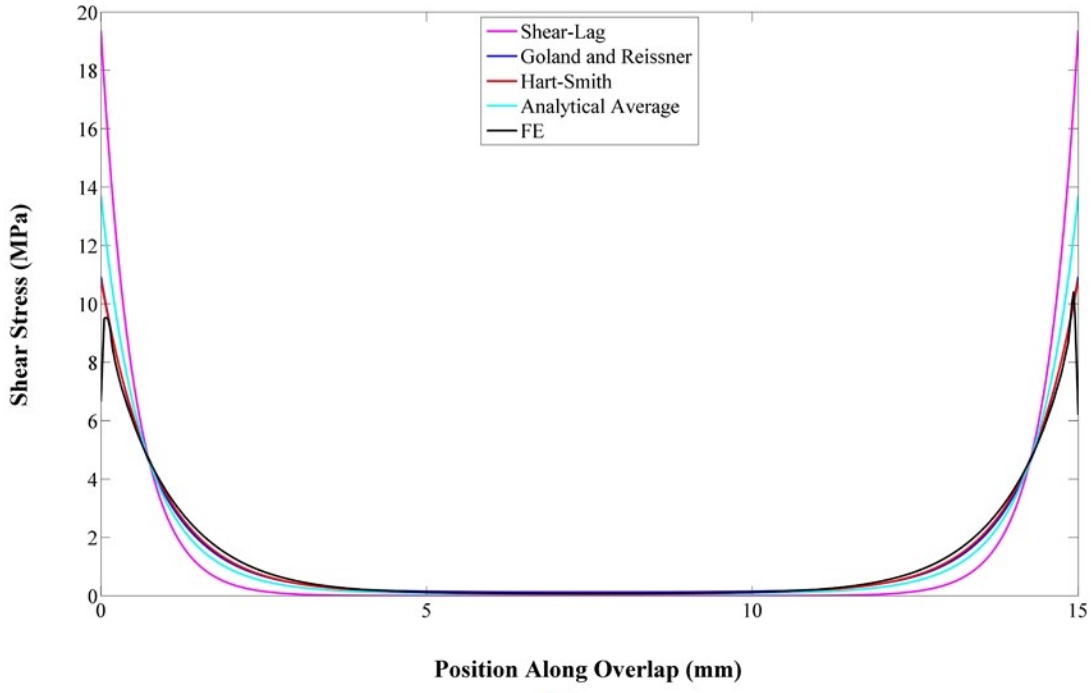

Figure 2.13: Model 1 stress distribution for an adhesive thickness of 0.1 mm: (a) shear stress distribution; (b) peel stress distribution

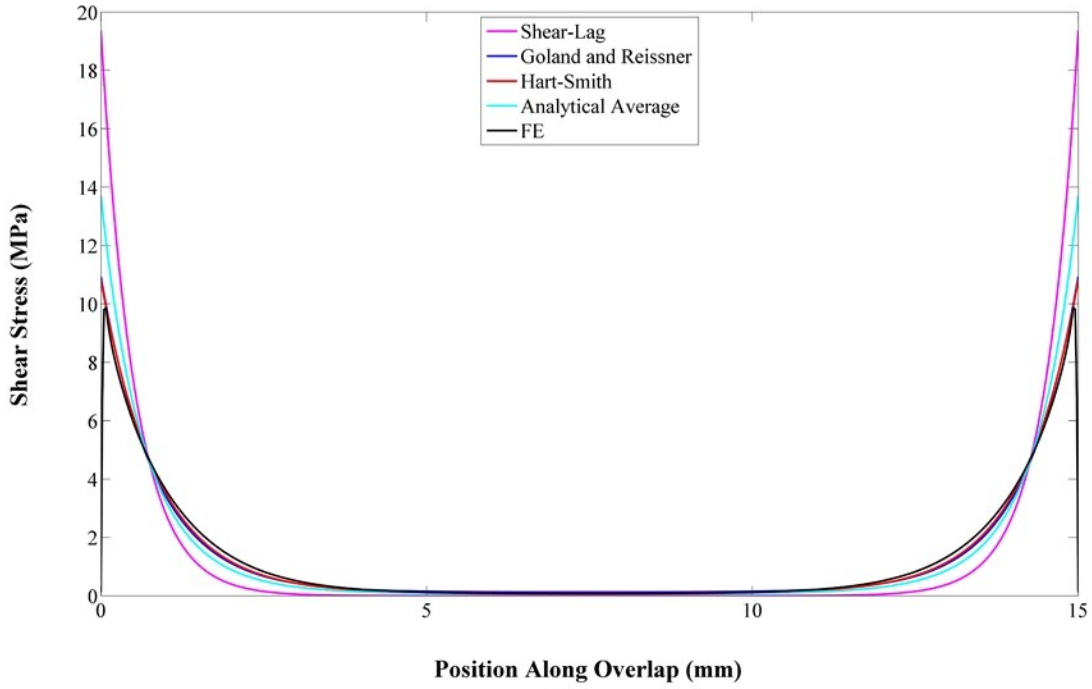

(a)

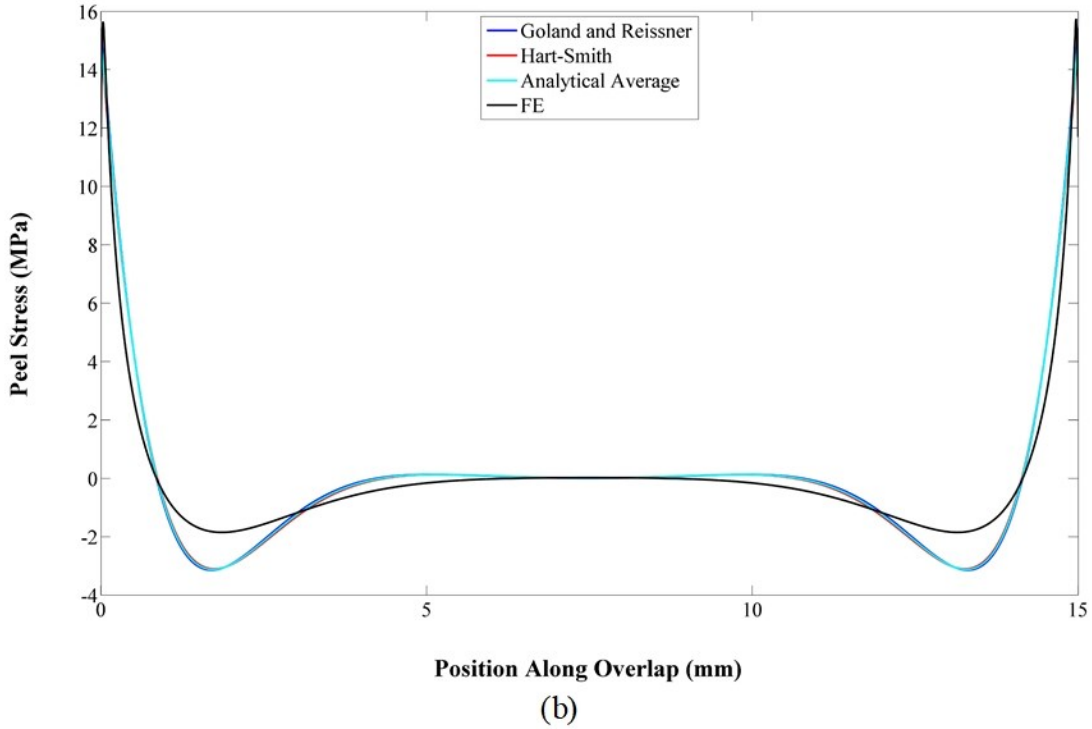

(b)

Figure 2.14: Model 2 stress distribution for an adhesive thickness of 0.1 mm: (a) shear stress distribution; (b) peel stress distribution

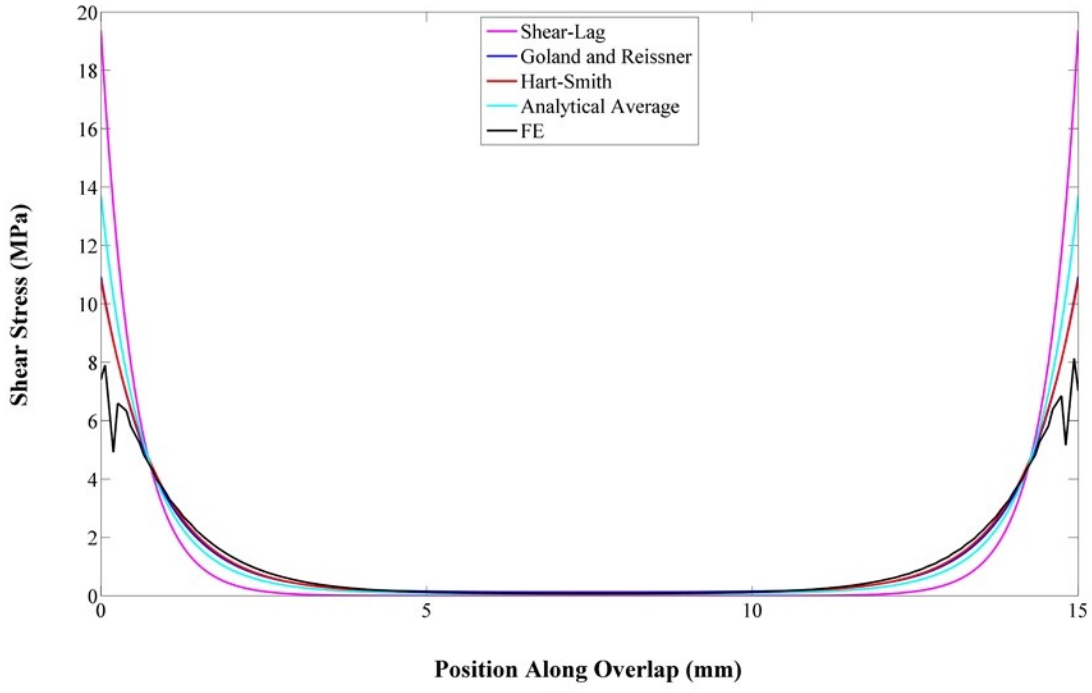

Figure 2.15: Model 3 stress distribution for an adhesive thickness of 0.1 mm: (a) shear stress distribution; (b) peel stress distribution

The adhesive shear and peel stress distributions for adhesive thicknesses of 0.3 mm and 0.5 mm, given by Model 2 and the analytical models, are shown in Figure 2.16 and Figure 2.17. The shear stress distribution of the shear-lag model compares well with the Goland and Reissner, and Hart-Smith models for an adhesive thickness of 0.3 mm, while slightly deviating again for an adhesive thickness of 0.5 mm. Comparing the stress distributions from the Goland and Reissner, and Hart-Smith models shows that the slightly deviate from each other with increasing adhesive thickness.

Model 2 compares well with the classical analytical models, as shown in Figure 2.14, Figure 2.16 and Figure 2.17, with the most significant error found in the maximum adhesive shear stresses, as shown in Table 2.3. This is attributed to the fact that the analytical models cannot represent the adhesive shear stress free boundary condition at the ends of the overlap region. The shear stress from the analytical models continually increases to a maximum at the ends of the overlap region, which violates the shear stress free boundary condition [83, 84]. On the other hand, Model 2 tends to zero near the ends of the overlap region, thus, it is reasonable to expect a significant difference in the maximum adhesive shear stress.

Table 2.3 shows that the magnitude of the maximum shear stress from Model 2 is initially less than the maximum average analytical shear stress for an adhesive thickness of 0.1 mm. The opposite is true for an adhesive thickness of 0.5 mm. On the other hand, the maximum peel stress magnitude from Model 2 is initially greater than the maximum average analytical peel stress for an adhesive thickness of 0.1 mm. For adhesive thicknesses of 0.3 mm and 0.5 mm, the maximum peel stress magnitude from Model 2 becomes less than the maximum average analytical peel stress. The relative error percentages between the maximum shear and peel stresses determined by the average analytical model and Model 2 are tabulated in Table 2.3 and displayed in Figure 2.18.

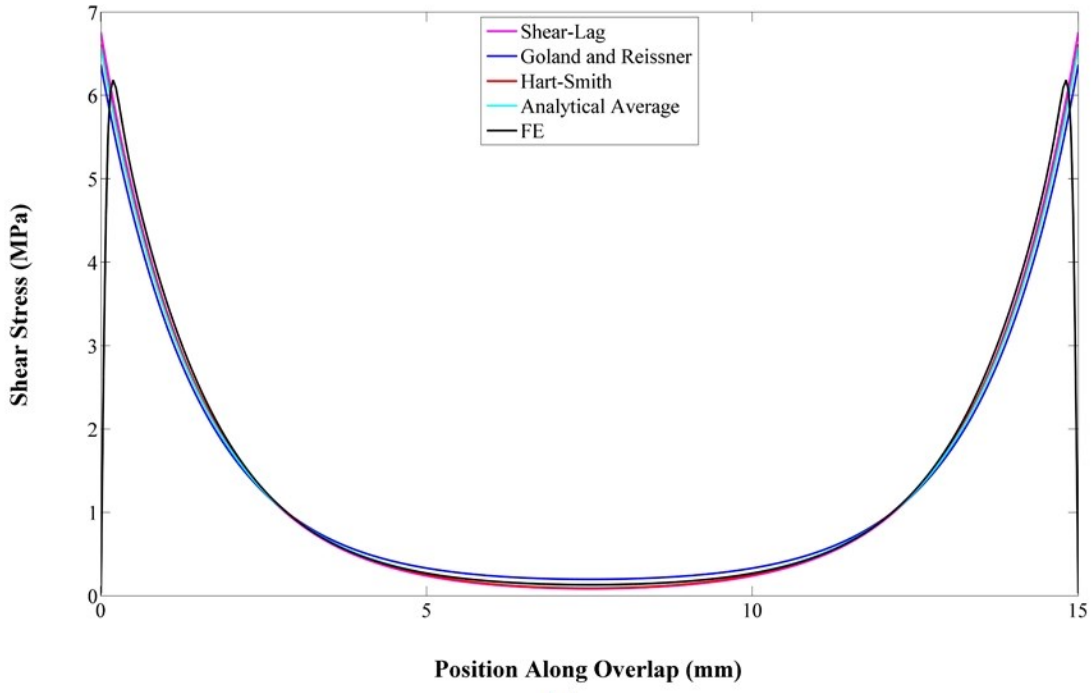

Figure 2.16: Model 2 stress distribution for an adhesive thickness of 0.3 mm: (a) shear stress distribution; (b) peel stress distribution

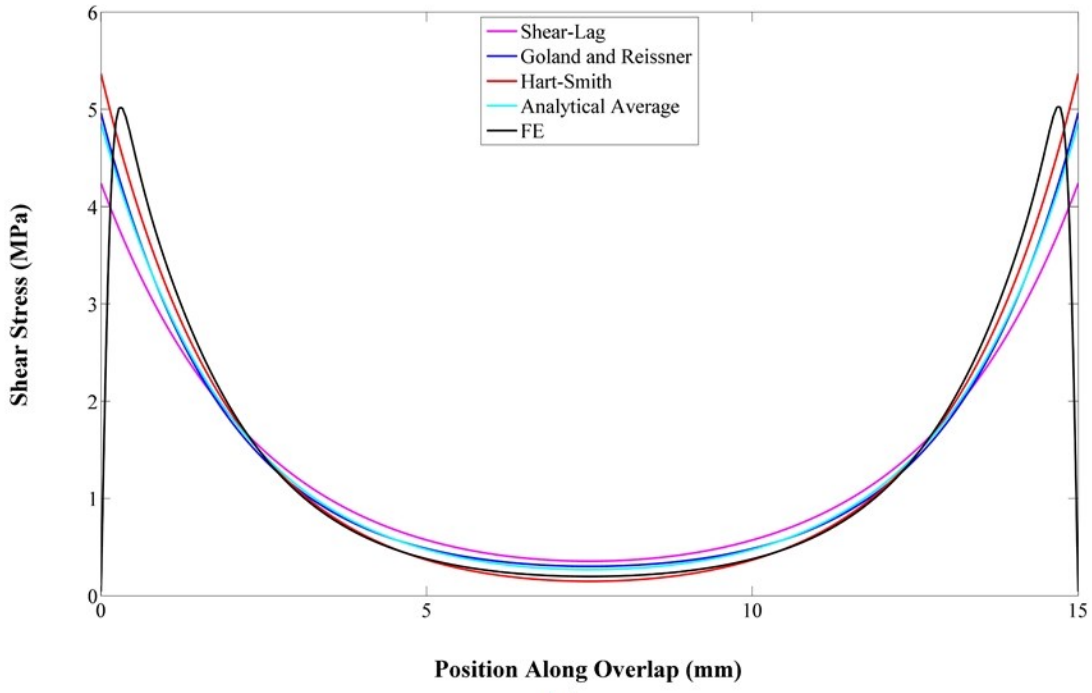

(a)

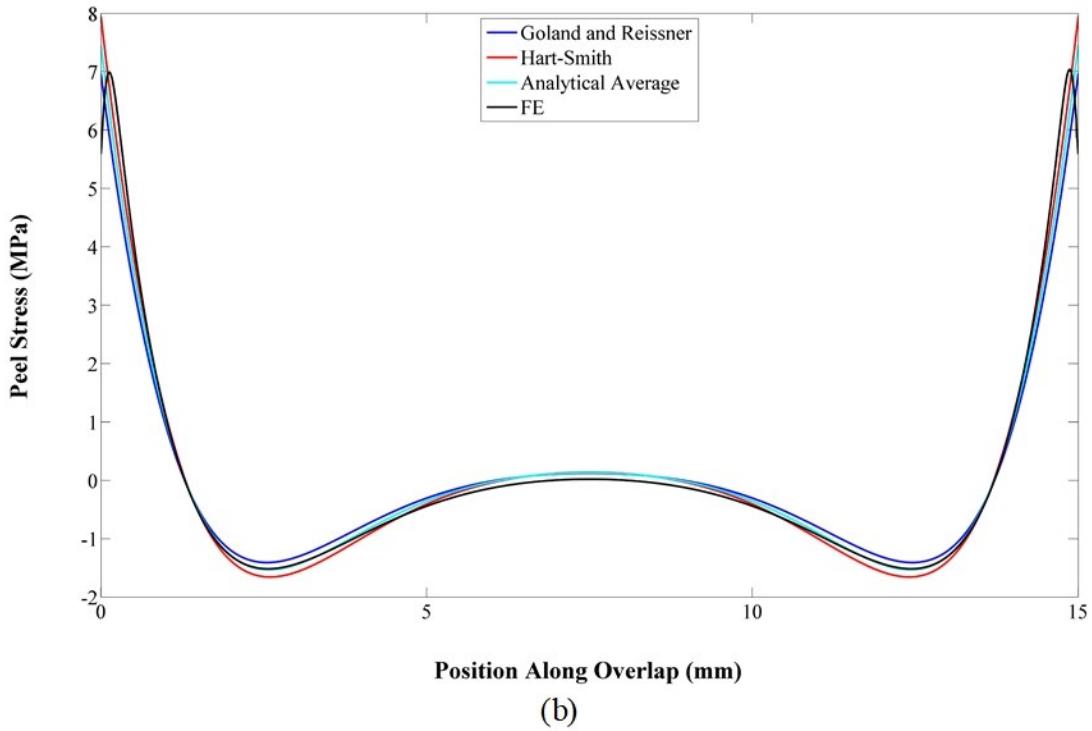

(b)

Figure 2.17: Model 2 stress distribution for an adhesive thickness of 0.5 mm: (a) shear stress distribution; (b) peel stress distribution

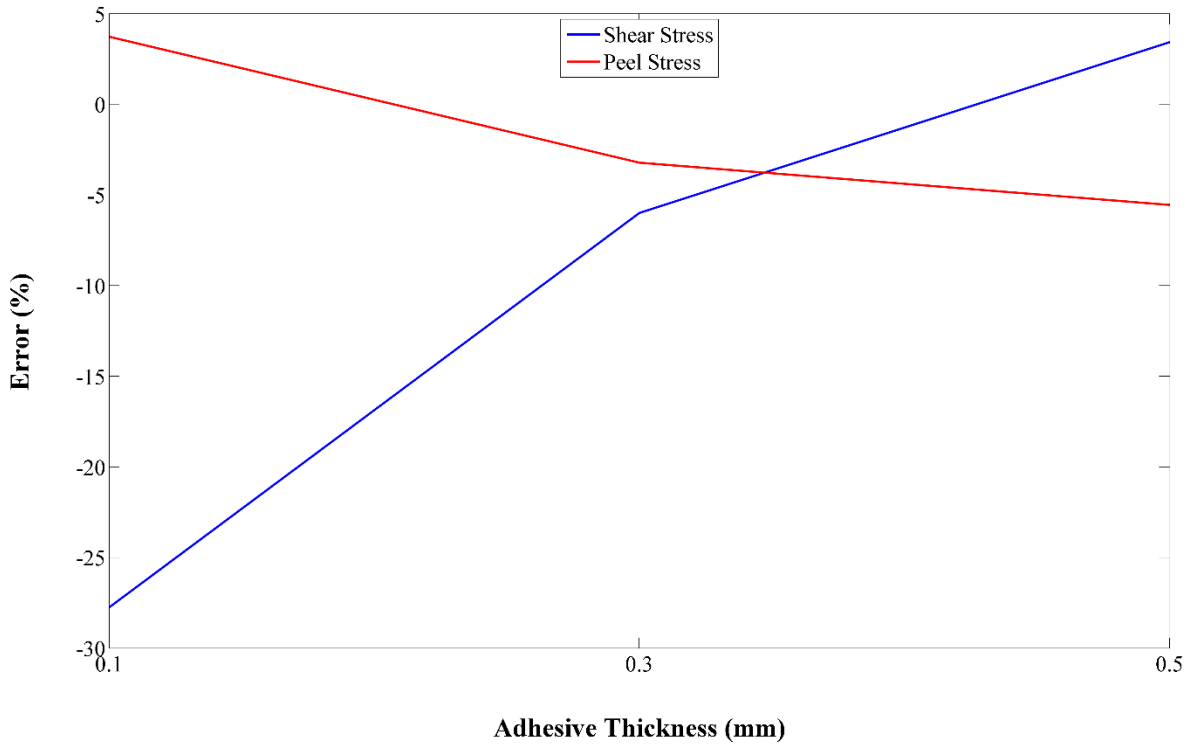

Figure 2.18: Maximum shear and peel stress relative error between the average analytical model and Model 2

The effect of the adhesive layer thickness on the shear and peel stress distributions is shown in Figure 2.19. Increasing the adhesive thickness results in a reduction in both the shear and peel stress magnitudes. From Table 2.3, when the adhesive thickness is increased from 0.1 mm to 0.5 mm, the maximum shear stress given by Model 2 reduces from 9.90 MPa to 5.02 MPa. Likewise, the maximum peel stress is reduced from 15.74 MPa to 7.04 MPa. Figure 2.19 also shows that the location of the maximum shear and peel stress shifts away from the overlap ends slightly with an increase in adhesive thickness. Considering one half of the overlap region length, the location of the maximum shear stress shifts from 0.079 mm to 0.33 mm, while the location of the maximum peel stress shifts from 0.031 mm to 0.12 mm. Further, the stress is distributed more evenly along the overlap length with increasing adhesive thickness, as locations near the middle of the overlap region show a slight increase in shear and peel stress, as shown in Figure 2.19.

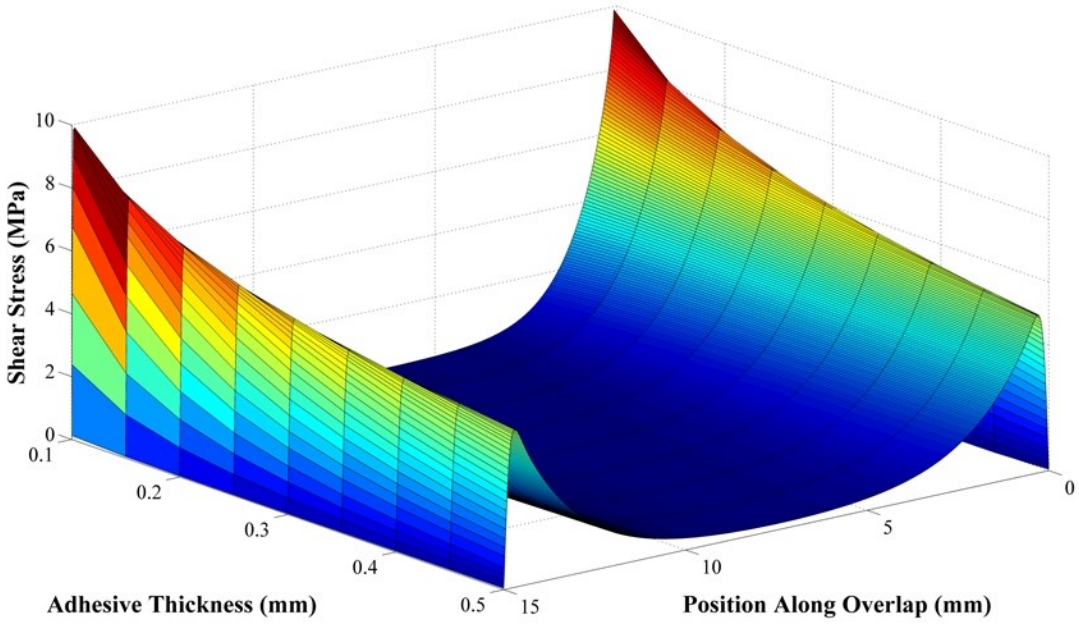

(a)

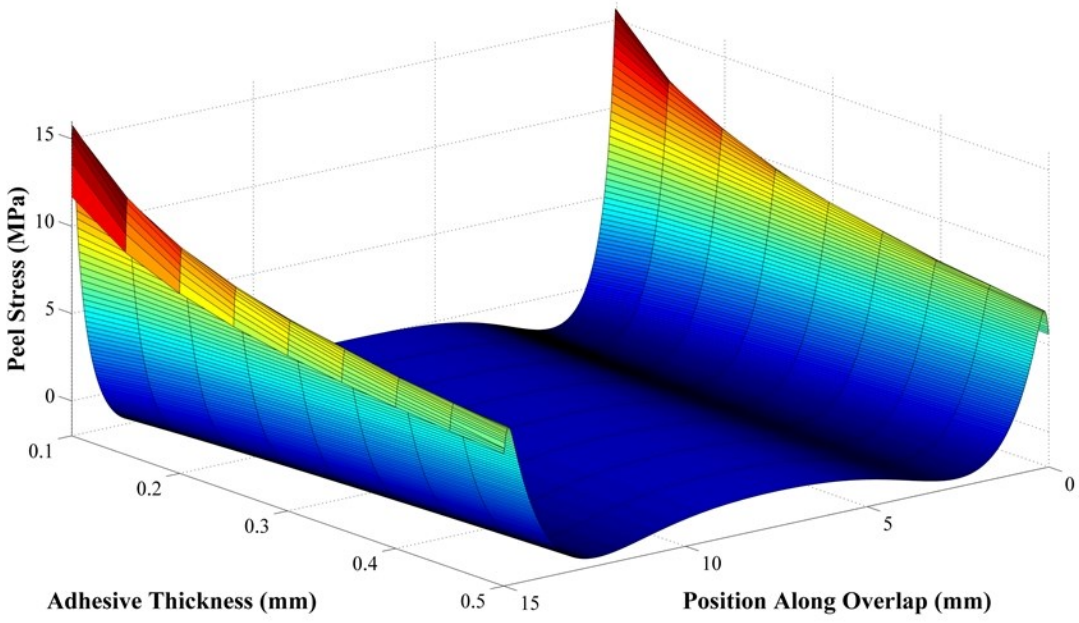

(b)

Figure 2.19: Effect of adhesive thickness on stress distribution: (a) shear stress distribution; (b) peel stress distribution

2.4. Experimental Tensile Test: Dinitrol 501 FC HM

The adhesive material used to build the SLJ specimens used for experimental testing in Chapter 3 is Dinitrol 501 FC HM. This adhesive is a semi-structural humidity curing polyurethane adhesive, which is ideal for applications such as mounting body panels or windshields to locomotive vehicles. Semi-structural adhesives in this context are defined as adhesives which are used when material failure is relatively less critical than a structural adhesive. Tensile testing is performed on SLJ specimens to verify the static properties provided in the manufacturers technical data sheet (see Appendix). Fabrication of the SLJ specimens, and the experimental procedure are discussed and the results are compared with the data provided by the adhesive manufacturer. Four SLJ specimens are tested and are used for the material property determination.

2.4.1. Single Lap Joint Specimen Fabrication

There are many factors to be considered when assembling adhesive bonded joints. As discussed in Section 2.3, the adhesive thickness has a direct impact the load carrying capabilities of the bonded joint. Thus, it is critical to build the specimens according to the designed thickness, within a reasonable level of tolerance. Further, surface preparation has a significant impact on the quality of adhesion achieved by the bonded joint. Poor surface preparation may lead to adhesive failure, where failure occurs at the interface between the adhesive and adherend, as opposed to cohesive failure, where failure occurs through the adhesive itself. Cohesive failure gives a higher joint strength, which is desired. Thus, it is important to follow the correct surface preparation procedures.

A simple approach to maintaining the desired adhesive thickness for a SLJ is to build a jig fixture, as seen in Figure 2.20. This is simplified version of the fixture used in [85] for adhesive bonded double lap joints. The fixture and alignment guides are represented by the blue and red colours respectively. The stepwise change in thickness is used to control the adhesive thickness. The alignment guides are used to maintain the desired overlap length, and align the two adherends. Finally, clamps (not shown in the figure) are used to press the adherends against the surface of the jig fixture, which ensures that the desired adhesive thickness is achieved within a reasonable level of tolerance.

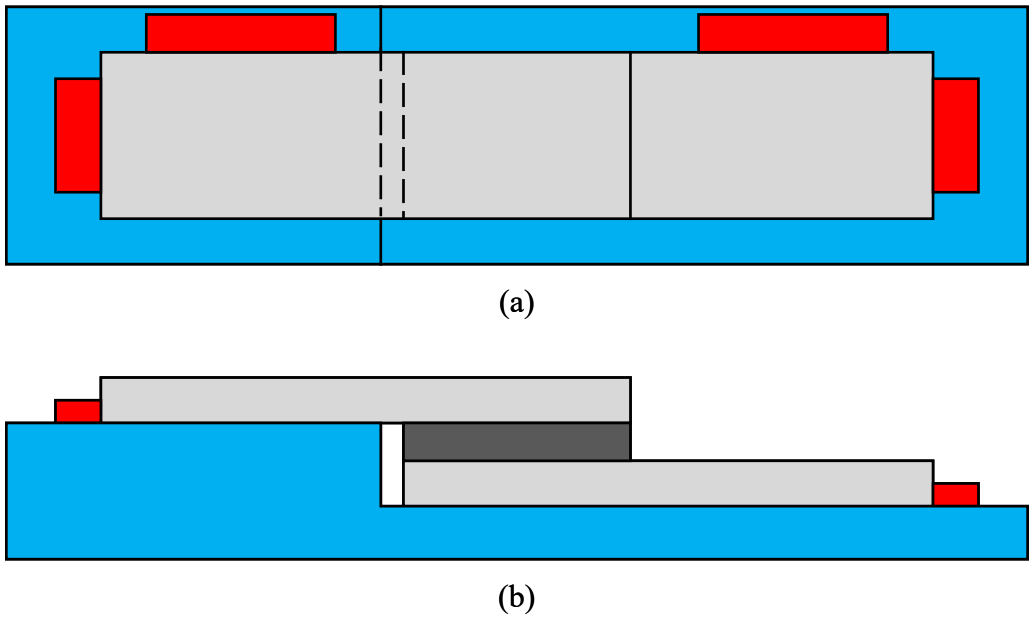

Figure 2.20: SLJ Jig Fixture: (a) top view; (b) side view

Surface preparation is done per the adhesive manufacturers guidelines. To begin, the surface of the adherend is cleaned with acetone to remove any dirt or oil. The adherends must sit for ten minutes to allow the acetone to evaporate. Next, an activator (Dinitrol 520) is applied to the surface of the adherend, which must dry for 10 minutes. A primer (Dinitrol 550) is applied with a sponge to the overlap area of the adherend, which must dry for 10 minutes. Finally, the adhesive is applied to the adherends, and the joint is assembled. It is worth mentioning that the time between surface preparation steps should not exceed a 24-hour period as this may compromise the integrity of the bonding surface.

2.4.2. Experimental Apparatus

The strength and material properties of the adhesive are determined experimentally using a Chatillon TCD 1100 digital force tester, as shown in Figure 2.21. This machine is ideal for testing composite and adhesive materials, with a load capacity of 1,124 lbf (5 kN), and an intelligent load sensing system with measuring accuracies better than 0.1% full scale [86]. The main components include the load frame, the load cell, specimen grips, and the TCD series consol. The specimen grips used are offset grips (not shown in the figure), which are ideal for

testing SLJ specimens due to the load eccentricity, otherwise spacers would be required for testing.

Figure 2.21: Chatillon TCD 1100 digital force tester [86]

2.4.3. Experimental Procedure

The user uses the TCD series console to define the load test to be performed; tensile loading until failure in this case. The displacement rate is selected as 25 mm/min. The load cell readings are zeroed prior to inserting the SLJ specimen. The SLJ specimen is inserted into the grips of the load frame, ensuring that the longitudinal axis of the SLJ specimen is parallel to the applied load axis. The offset grips are adjusted such that the SLJ specimen is positioned vertically. Once the test is completed, the data is saved, and the SLJ specimen is removed from the grips for further inspection.

2.4.4. Results

The shear stress-strain relationships for each of the four specimens are shown in Figure 2.22. In general, the four specimens give similar results in the elastic region of the adhesive,

whereas there are some notable discrepancies in the plastic region. Specimen 2 shows a staggered reduction in stress carrying capability beyond the location of ultimate strength. This is the result of additional adhesive, squeezed from the overlap region of the SLJ during fabrication as seen in Figure 2.23, which had not failed when the adhesive within the overlap region failed. It was recommended that this additional adhesive material not be removed prior to testing to avoid any potential stress concentrations. This allowed the additional adhesive material of specimen 2 to carry load even though failure occurred within the bulk of the adhesive. However, the other specimens did not present this issue, as can be seen by the rapid and smooth reduction in shear stress beyond the ultimate strength locations, leading to adhesive failure.

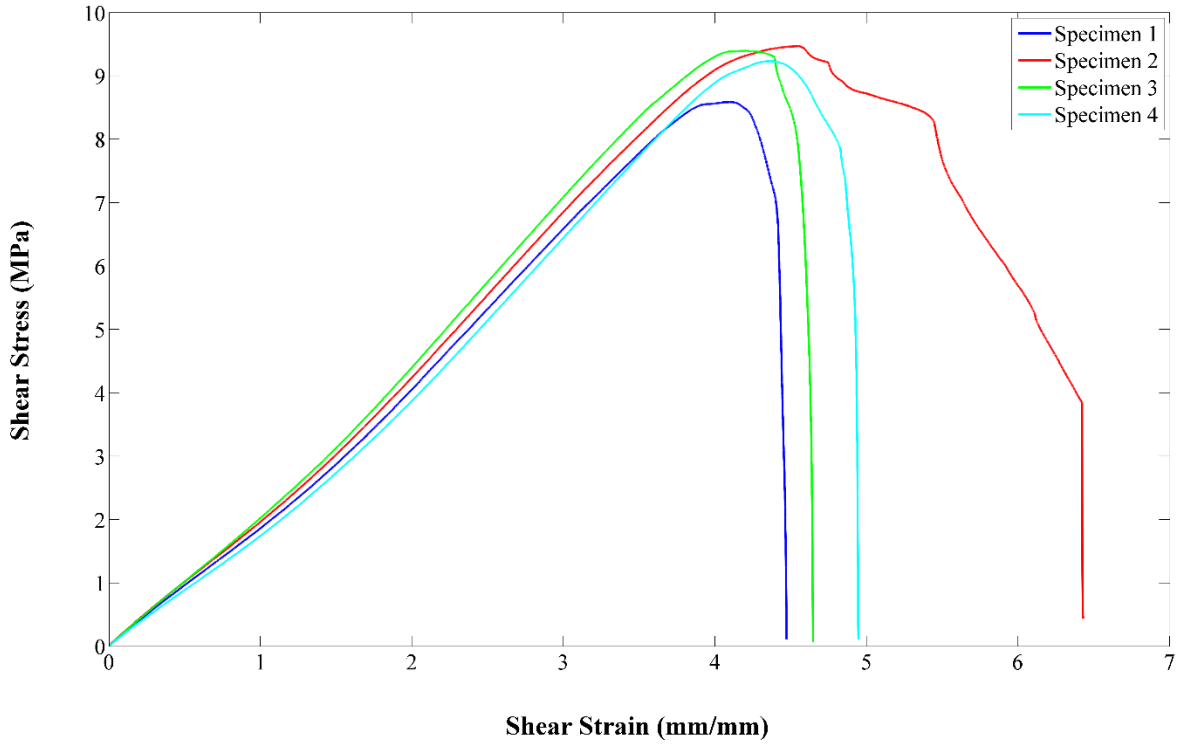

Figure 2.22: Shear stress-strain relationship; Dinitrol 501 FC HM

The measured material properties of each specimen, including the average of the four specimens, are displayed in Table 2.5. The initial portion of the shear stress-strain curve, where the slope is slightly reduced, is neglected [87]. The shear modulus is measured from the linear portion of the shear stress-strain relationship. The shear modulus ranged from 2.53 MPa – 2.69

MPa, giving an average of 2.61 MPa. The shear modulus provided by the adhesive manufacturer is 2.5 MPa, thus the measured shear modulus gives a reasonable error of 4.4%. The ultimate strength of specimen 1 is 8.59 MPa, which is noticeably lower than the other specimens 2 – 3 ranging from 9.23 MPa – 9.47 MPa. The lap shear strength of the adhesive was found using the 2% offset method, where a line with the same slope as the shear modulus is offset by 2%, and the lap shear strength is recorded at the intersection of itself and the shear stress-strain curve [88]. The measured lap shear strengths range from 7.60 MPa – 8.36 MPa, giving an average of 7.93 MPa. The lap shear strength given by the adhesive manufacturer is given as approximately 9 MPa, thus the measured lap shear strength gives an error of 11.9%. The reason for this error could be the result of the ambient conditions while the adhesive was curing after fabrication.

Table 2.5: Dinitrol 501 FC HM Measured material properties

SLJ Specimen	Shear Modulus (MPa)	Lap Shear Strength (MPa)	Ultimate Strength (MPa)
1	2.53	7.60	8.59
2	2.62	7.67	9.47
3	2.69	8.07	9.39
4	2.61	8.36	9.23
Average	2.61	7.93	9.17

The failure surfaces of the SLJ specimens, after tensile testing, are shown in Figure 2.23. The excess adhesive material discussed earlier can clearly be seen. Examining the failure surfaces shows that the adhesive failed in cohesion for all specimens, since the failure surfaces cut through the bulk adhesive material, as opposed to the interface between the adhesive material and the adherend. This confirms that the tensile tests are meaningful representations of the adhesive material. Many ridges perpendicular to the load direction can be seen in the failure surface of each specimen, which is expected for semi-structural adhesives [89].

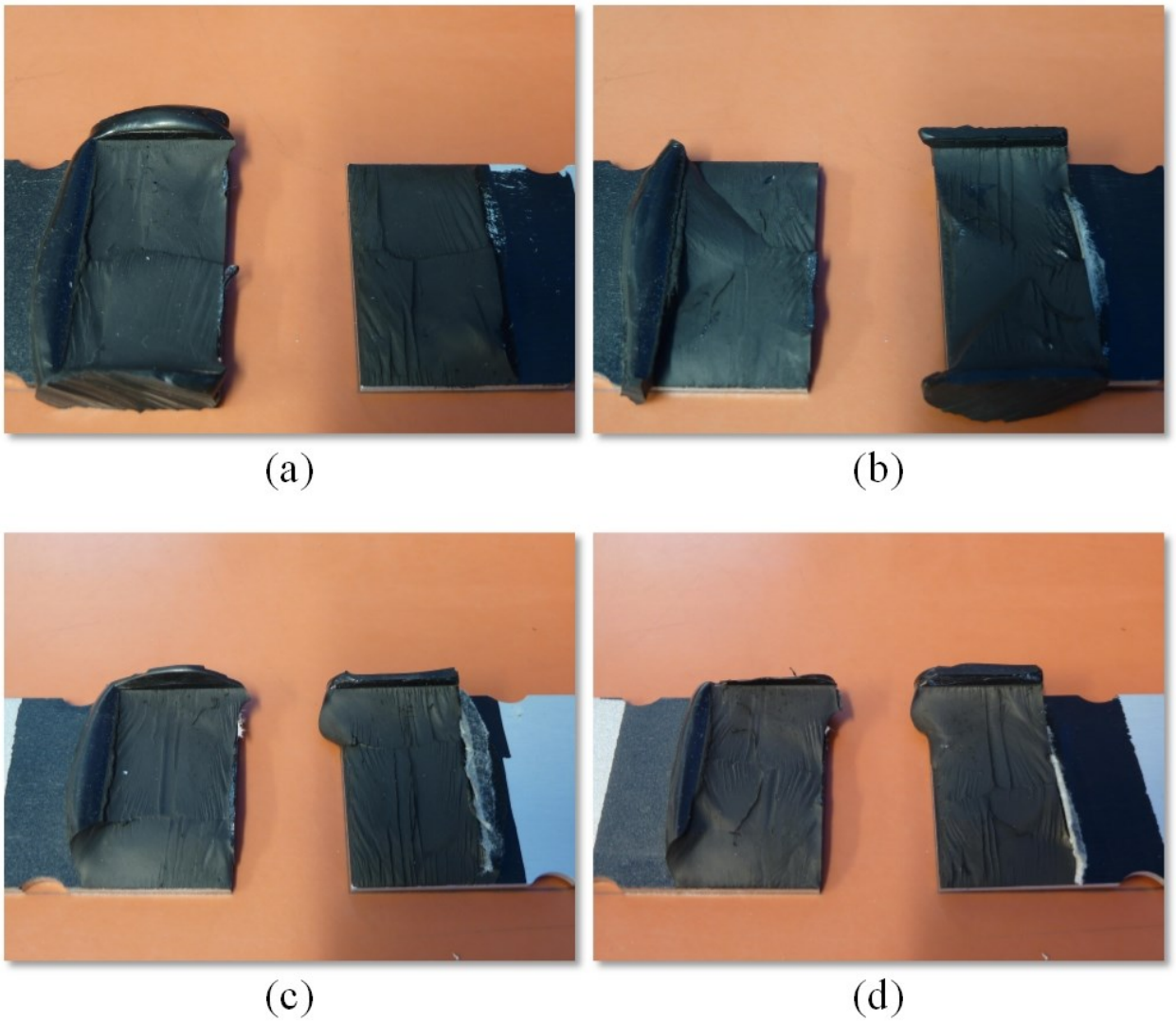

Figure 2.23: Adhesive failure: (a) specimen 1; (b) specimen 2; (c) specimen 3; (d) specimen 4

2.5. Conclusion

The static single physics scenario, involving the determination of the stress distribution within the adhesive layer of an adhesive bonded SLJ, has been done both analytically and numerically. Three FE models were created to compare different meshing strategies to model the stress distribution within the adhesive layer. It was found that using quadratic quadrilateral and triangular elements in the adhesive and adherends respectively, gave the most accurate results when compared with the analytical models, while having a relatively low computational demand. It was shown that the adhesive layer thickness has a significant impact on the adhesive

stress distribution. Increasing the adhesive thickness caused a reduction in the maximum shear and peel stress, while distributing the load more evenly across the bond line. The material properties of Dinitrol 501 FC HM were measured from tensile testing, using four SLJ specimens. The measured shear modulus was in close agreement with the manufacturers published shear modulus. The measured lap shear strength deviated slightly from the manufacturers data, however, this may be the result of the climate conditions while the adhesive specimens cured. The failure surface of each specimen had ridges perpendicular to the applied load direction, which is expected for semi-structural adhesives.

Chapter 3 Simulation of Dynamic Behaviours of an Adhesive Bonded Single Lap Joint

This chapter focuses on the effects of adhesive bonding on the dynamic behaviours of adhesive bonded joints. The operating environment of automotive, locomotive, and aerospace vehicles introduces vibration excitation from numerous sources including; the road surface, the vehicle's engine, wind induced vibration, etc. Since adhesives can be used to bond windshields and body panels, understanding their dynamic behaviours is important to ensure safe operation of the vehicle. Thus, reliable models are required to assist in the design of robust adhesive bonded joints. In this chapter, the dynamic behaviours of an adhesive bonded SLJ are investigated using numerical analysis approaches.

Two numerical approaches are used to model the dynamic behaviours of the SLJ specimens; the FEM, and the TMM. The TMM is a computationally efficient alternative to the FEM, which is used to determine the natural frequencies and mode shapes of discontinuous beam structures. The FEM, on the other hand, is advantageous since it can model the transmissibility functions of a system in addition to the natural frequencies and mode shapes. Due to the layered construction of the overlap region within a SLJ specimen, effective material properties must be used for the TMM. Typically, these effective material properties are approximated using an additive method detailed in [67], however, this approach does not give the effective material properties directly. Thus, a single variable TMM model updating approach is presented, which uses volume fractions to compute the effective density and optimization to update the effective Young's modulus of the overlap region.

The effects of the overlap length, and the overlap region adherend and adhesive layer thickness on the dynamic behaviours of an adhesive SLJ are investigated numerically. Varying the overlap length of the SLJ gives insight of the robustness of the effective Young's modulus found using the single variable TMM model updating approach. The effective Young's modulus of the overlap region is found for a particular overlap length. This effective Young's modulus is then used for a SLJ with different overlap lengths to see whether it adequately represents their dynamic behaviours. The adherend and adhesive thicknesses are varied to explore whether an adherend to adhesive thickness ratio exists for the effective material properties. The study will investigate if the effective Young's modulus found for a particular adherend to adhesive ratio can

still be used if the material thicknesses are changed, while maintaining the adherend to adhesive thickness ratio.

Several SLJ specimens are used in this chapter, constructed of aluminum adherends, bonded by the Dinitrol 501 FC HM adhesive, whose material properties are listed in Table 3.1. The geometry of the SLJ specimen is shown in Figure 3.1. The adhesive Young's modulus measured in Chapter 2 is used for the numerical models. The SLJ specimens have overlap lengths ranging from 30 mm – 60 mm, in 10 mm increments. Table 3.2 shows the SLJ specimen names, their corresponding dimensions, and the adherend to adhesive thickness ratio of each beam. Specimens with an adherend and adhesive thickness of 2.2 mm and 1.9 mm respectively, are identified by the letter A following the beam number, while specimens with an adherend and adhesive thickness of 1.6 mm and 1.38 mm are identified by the letter B. The specimens are grouped as category A and category B specimens, respectively.

Table 3.1: Dynamic SLJ specimen material properties

Adherend Young's Modulus, E	70 GPa
Adherend Density, ρ	2,700 kg/m^3
Adherend Poisson's Ratio, v	0.33
Adhesive Young's Modulus, E_{ad}	7.31 MPa
Adhesive Density, ρ_{ad}	1,200 kg/m^3
Adhesive Poisson's Ratio, v_{ad}	0.40

Table 3.2: Dimensions of the SLJ specimens subjected to harmonic base excitation

Specimen Name	Overlap Length, l_{ad} (mm)	Adherend Thickness, t (mm)	Adhesive Thickness, t_{ad} (mm)	Adherend/Adhesive Thickness Ratio
Beam 1A	30	2.20	1.90	1.16
Beam 1B	30	1.60	1.38	1.16
Beam 2A	40	2.20	1.90	1.16
Beam 2B	40	1.60	1.38	1.16
Beam 3A	50	2.20	1.90	1.16
Beam 3B	50	1.60	1.38	1.16
Beam 4A	60	2.20	1.90	1.16
Beam 4B	60	1.60	1.38	1.16

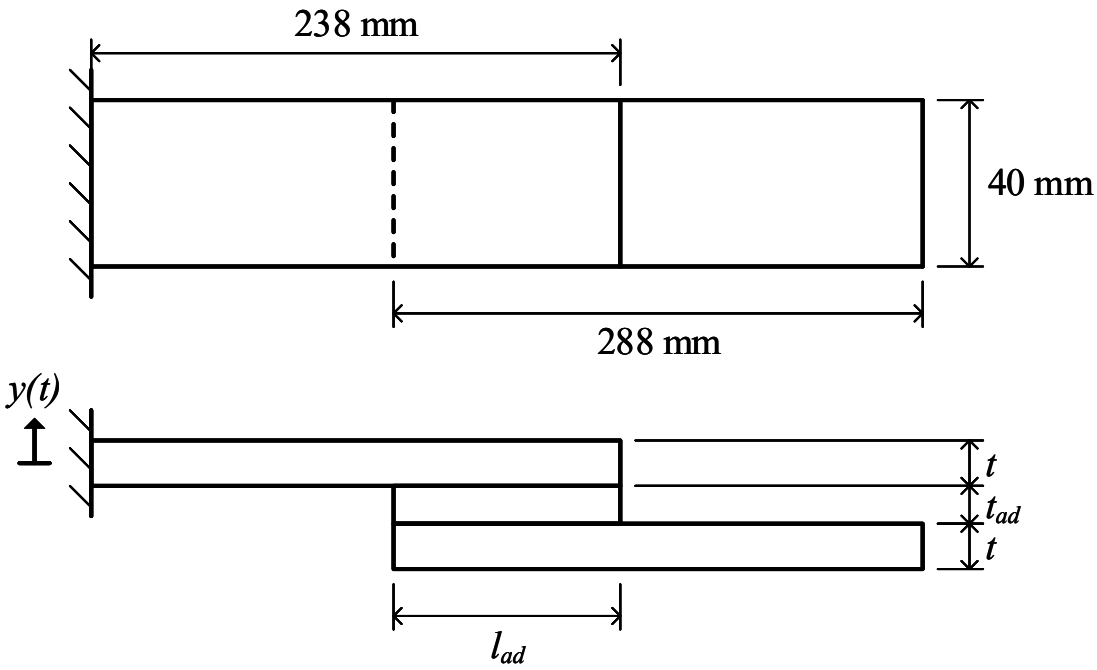

Figure 3.1: Dynamic SLJ specimen geometry (not drawn to scale)

3.1. Finite Element Model

Developing the FE model for the dynamic single physics case in this chapter presents similar challenges to those discussed in Chapter 2. In this model, the goal is to determine the dynamic behaviours of the SLJ specimens, including their natural frequencies, mode shapes, and transmissibility functions. Again, a balance exists between computation efficiency and model accuracy. The dynamic SLJ specimens face the same modelling challenges due to their poor aspect ratio. However, since a dynamic analysis is performed in this chapter there is a greater need for computational efficiency, as the simulation must be conducted over a specified time duration, as opposed to a single stationary analysis per specimen from Chapter 2.

Similar modelling simplifications from Chapter 2 are used in the FE model for the dynamic SLJ specimens. A 2D FE model is used since the experimental apparatus, discussed in Chapter 4, measures the in-plane transverse dynamic behaviours of the specimens. Therefore, different vibration mode orientations cannot be measured with the current experimental apparatus. Further, the model mesh within the adhesive layer region is simplified by using significantly less elements compared to the FE model of Chapter 2. Since the goal is to model

the dynamic behaviours of the dynamic SLJ specimens, there is no need for a detailed mesh to measure the stress distribution within the adhesive layer.

The FE model is developed in the following, including the model mesh, boundary conditions, damping, study and physics, and post-processing. In this chapter, the FE model is used as a benchmark for model updating, and to compare the performance of the single variable TMM model updating approach, and the additive TMM approach. The general geometry of the FE models is shown in Figure 3.2.

Figure 3.2: Geometry of the dynamic SLJ FE model

3.1.1. Dynamic Single Lap Joint Model Mesh

The model mesh used for the dynamic SLJ specimens is user defined for both the adherend and adhesive layers. Since the specimens are subjected to harmonic base excitation, the in-plane transverse vibration causes bending stress within the specimens. As mentioned in Section 2.2.2, the quadratic quadrilateral elements can represent all states of pure bending and constant strain. Thus, the quadratic quadrilateral elements are well suited for this application.

A computationally efficient model mesh is particularly important as both a time and driving frequency sweep are performed. Any increase in the model's degrees of freedom would result in a significant increase in solution time, and hardware demand (required RAM and CPU demand). To ensure accuracy and computational efficiency, the number of elements used is minimized, while preserving element quality. To achieve this, the adherend and adhesive layers use one quadratic quadrilateral element through their thickness. The number of elements along the length of the adherends is then selected such that the element quality is maximized. For the category A specimens, the top and bottom adherends have 107 and 127 elements along their length, respectively, while the adhesive layer has 27 elements along its length. This gives a total of 261 elements, with an average and minimum element quality of 0.9985 and 0.9879, respectively. Since the material thicknesses of the category B specimens are reduced, more elements are required along the specimen length to preserve element quality. For the category B

specimens, the top and bottom adherends have 148 and 178 elements along their length, respectively, while the adhesive layer has 38 elements along its length. This gives a total of 364 elements, with an average and minimum element quality of 0.9992 and 0.9828, respectively. Figure 3.3 shows the FE model mesh for category A and B specimens.

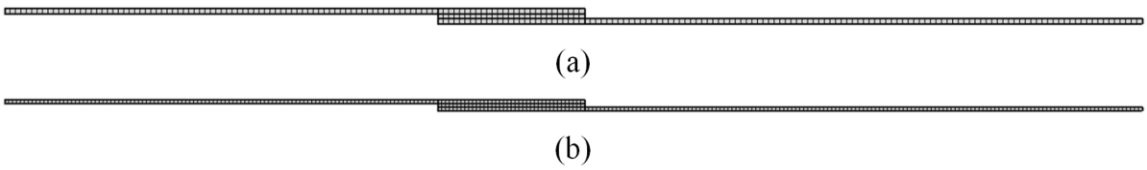

Figure 3.3: Dynamic SLJ model mesh: (a) category A specimens; (b) category B specimens

3.1.2. Rayleigh Damping

Damping is an important consideration when modeling a structure undergoing harmonic excitation. The inclusion of damping restricts the vibration amplitude of a system, and prevents the system from vibrating with an unbounded magnitude at resonant frequencies [90]. This is particularly important when evaluating the transmissibility functions of the dynamic SLJ FE model, as it experiences multiple resonances within the excitation frequency range considered. Exclusion of damping in a model could cause singularities when the specimen is excited near a resonant frequency, which could prevent the FE software from converging, or give overstated vibration amplitudes if a solution is found. Thus, it is crucial to include an appropriate damping model, to ensure the FE transmissibility functions compare well with the experiment.

The structural mechanics module in Comsol Multiphysics enables the user to select internal damping models such as: Rayleigh damping, isotropic loss factor, viscous damping, and explicit damping. Of these, Rayleigh damping is the only model which can be applied in both a frequency domain and time domain analysis, while the others only apply to frequency domain analyses [91]. Since the transmissibility functions of the FE models are evaluated in a time domain analysis, the Rayleigh damping model is used.

Rayleigh damping is a frequency dependant model, which relates the damping matrix to the mass and stiffness matrices through constants of proportionality. The Rayleigh damping model is formulated as follows [92]:

$$\mathbf{C} = \mu\mathbf{M} + \lambda\mathbf{K} \tag{3.1}$$

where μ and λ represent the mass and stiffness constants of proportionality respectively, and **M**, **C**, and **K** represent the mass, damping, and stiffness matrices of the system respectively. The damping ratios and resonant frequencies are related as follows:

$$\zeta_n = \frac{\mu}{4\pi f_n} + \pi\lambda f_n \tag{3.2}$$

where f_n represents the n^{th} resonant frequency of the system, and ζ_n represents the corresponding damping ratio. The constants of proportionality can be solved with equation (3.2), using two resonant frequencies and their corresponding damping ratios, as follows:

$$\mu = 4\pi f_1 f_2 \frac{\zeta_1 f_2 - \zeta_2 f_1}{f_2^2 - f_1^2} \tag{3.3}$$

$$\lambda = \frac{\zeta_2 f_2 - \zeta_1 f_1}{\pi\left(f_2^2 - f_1^2\right)} \tag{3.4}$$

where subscripts 1 and 2 represent the resonant frequency numbers. It should be noted that these subscripts do not necessarily correspond with the frequency mode numbers, as any two resonant frequencies may be used to tune the constants of proportionality.

There are some notable insights to consider when using Rayleigh damping. Figure 3.4 shows an example of the frequency dependent damping ratios given by the Rayleigh damping model for a beam with two resonant frequencies of 10 Hz and 40 Hz, and respective damping ratios of 0.01 and 0.006. The mass and stiffness proportional terms are plotted individually, as well as the complete Rayleigh damping relationship shown in (3.2). The mass and stiffness proportional terms of the Rayleigh damping cross at approximately 31 Hz. The mass proportional term is the main contribution to damping when the frequencies are lower than the crossover point. On the other hand, the stiffness proportional term is the main contribution to damping when the frequencies are larger than the crossover point. Further, the frequency values within the range of the tuning resonant frequencies tend to be under-damped in comparison to their actual damping ratios. The opposite can be said about frequencies outside of this range. Therefore, it is important to carefully select the appropriate frequencies when tuning the

Rayleigh damping model. This is further explored in Section 4.2.4 from Chapter 4 by using different resonant frequencies pairs to tune the Rayleigh damping model for Beam 1A.

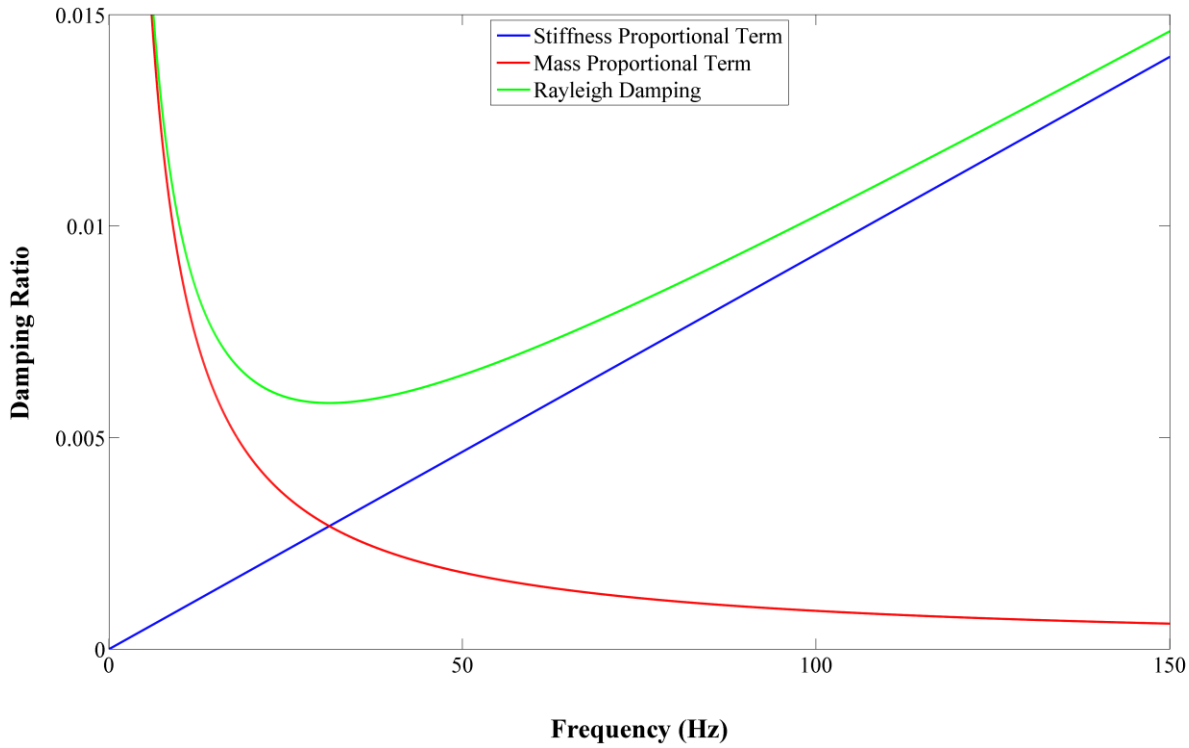

Figure 3.4: Example of Rayleigh damping

3.1.3. Boundary Conditions

Appropriate physical constraints are used in order to simulate the harmonic base excitation, shown in Figure 3.1. The undamped natural frequencies and mode shapes are first computed by using a fixed constraint for the clamped end of the specimens, and performing an eigenfrequency analysis. Once the natural frequencies are found, the fixed constraint is replaced by a prescribed displacement, and a time dependent study is performed. The model studies are detailed in Section 3.1.4. Since a harmonic base excitation is applied to the dynamic SLJ specimens, the prescribed displacement is defined by a sinusoidal function as follows:

$$y(t) = 10\sin(2\pi ft) \tag{3.5}$$

where, $y(t)$ represents the base displacement in millimeters, f is the driving frequency, and t is the elapsed time. The driving frequency of the base excitation is controlled by the frequency sweep.

To ensure that the first three vibration modes are measured, the frequency range considered for this study is 1 Hz - 150 Hz. From this, the displacement amplitudes of the base and free end of the beam are evaluated for all excitation frequencies, to find the transmissibility functions.

3.1.4. Physics and Study

To determine the dynamic behaviours of the SLJ specimens, a dynamic single physics FE model is required. The FE model employs both an eigenfrequency and time dependent study, and the physics are defined by the solid mechanics module. The eigenfrequency study solves the undamped natural frequencies and mode shapes of the FE dynamic SLJ specimens. The time dependent study subjects the specimens to harmonic base excitation to measure the base and free end displacements. Further, an auxiliary sweep is used to perform the frequency sweep. The natural frequencies found in the eigenfrequency analysis are useful to estimate the locations where frequency sweep refinement is required. The auxiliary sweep sweeps through the driving frequencies, which define the frequency of the sinusoidal prescribed displacement boundary condition.

It is important to use an appropriate frequency resolution in order to generate a smooth transmissibility function, due to the steep gradients at the locations near resonant frequencies. A frequency resolution that is too fine would require a significant computational time and demand, however, the resulting transmissibility function would have a high amount of detail. On the other hand, a frequency resolution that is too coarse may not capture the resonant frequencies of the specimens, however, the computation time and demand would be significantly reduced. To achieve a balance between the transmissibility function detail, and computational time and demand, frequency resolutions of 0.25 Hz and 2 Hz are used for frequencies near and away from the natural frequencies, respectively. This ensures a balance between computational time and demand, and accuracy at the resonant frequencies.

The time dependent study includes the initial transient response of the dynamic SLJ specimens. The transmissibility functions should be evaluated using the steady state solution. Thus, selecting an appropriate time duration is an important consideration for the time dependent study, to ensure the solution reaches steady state. It is found that a time duration of three seconds allows the responses to achieve steady state over the frequency range considered. An

additional two seconds are added to the time dependent study, which represents the steady state solution. Thus, the time dependent study uses a total time duration of five seconds.

3.1.5. Post-Processing

Measuring the mode shapes of the dynamic SLJ specimens is done after conducting the eigenfrequency study. The sensor positions from the experiment are shown in Figure 4.3 from Section 4.1.1. Since the sensor x_{12} is positioned 10 mm from the free end of the specimens for the experiment, the FE mode shapes are measured up to this point, for comparison. Displacements are measured by an array of 2D cut points in the FE model. The FE model solves the mode shapes using an arbitrary scaling factor, thus the mode shapes are normalized to compare with the mode shapes of both the TMM approaches.

The transmissibility functions of the specimens are found using the method described in Section 4.1.1 from Chapter 4. The displacements used for the transmissibility function are measured using 2D cutpoints. The input and output displacements are measured at the base and 10 mm from the free end, respectively. The root mean squared (RMS) amplitude of the input and output displacement is used to compute the transmissibility function of each specimen.

3.2. The Transfer Matrix Method

The TMM is formulated such that a beam with piecewise continuous material and geometric properties is discretized into beam segments [57, 58, 59]. Within each beam segment, constant geometric and material properties are assumed. It is possible to use average or effective properties for a beam segment containing two or more material layers of constant thickness. The Euler-Bernoulli beam theory is used to derive the field transfer matrix for each element, relating the surface states of both sides of the element (i.e. left and right). Combining the field transfer matrix of each element yields the global transfer matrix of the system, from which the natural frequencies are obtained.

The free body diagram of an infinitesimal beam element, shown in Figure 3.5, is used to derive the governing equations for the system. The four independent state variables are assembled in a state vector as follows:

$$\mathbf{z} = \left[\phi \quad d\phi/dx \quad M \quad V \right]^T \tag{3.6}$$

where, ϕ is the transverse mode shape function, $d\phi/dx$ is the slope, M is the internal bending moment, and V is the internal shear force. The transverse displacement of the beam and the applied external force are denoted as $w(x,t)$ and $f(x,t)$, respectively. Performing force and moment balances, while assuming free vibration (i.e. applied external load neglected), and small deformation yields:

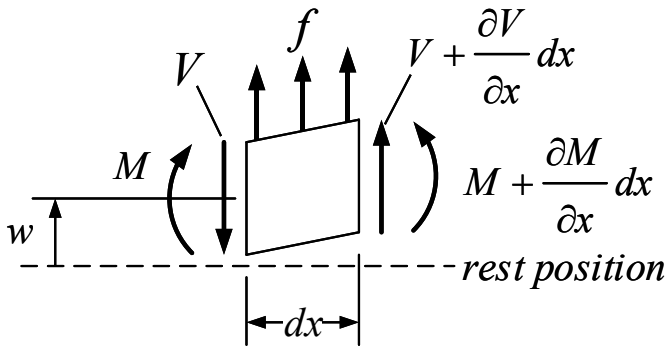

Figure 3.5: Infinitesimal Bernoulli beam segment free body diagram

$$\frac{\partial V(x,t)}{\partial x} = (\rho A)_j \frac{\partial^2 w(x,t)}{\partial t^2}, \quad \frac{\partial M(x,t)}{\partial x} = -V(x,t) \tag{3.7}$$

where, $(\rho A)_j$ is the mass per unit length of the jth beam segment. The transverse displacement of the beam is related to the internal bending moment, assuming the slope is small, through:

$$M(x,t) = (EI)_j \frac{\partial^2 w(x,t)}{\partial x^2} \tag{3.8}$$

where, $(EI)_j$ is the bending stiffness of beam segment j. Equations (3.7) and (3.8) represent the equations of motion for the beam segment from Figure 3.5. The material and geometric properties of beam segment j are represented by the mass per unit length, and bending stiffness. For a beam segment having a layered construction (i.e. differing material layers with a known thickness), its properties are typically determined in an additive manner [67], where the mass per unit length, and bending stiffness of each layer are added together. These properties are determined as follows for a bimorph structure:

$$(\rho A)_{eff} = b(\rho_{ad} t_{ad} + 2\rho t) \tag{3.9}$$

$$(EI)_{eff} = E_{ad} b \frac{t_{ad}^3}{12} + 2Eb\left[\frac{t^3}{12} + t\left(\frac{t_{ad}+t}{2}\right)^2\right] \tag{3.10}$$

where, $(\rho A)_{eff}$ and $(EI)_{eff}$ represent the effective mass per unit length and bending stiffness, respectively. The beam width, adherend thickness, and adhesive thickness are denoted by b, t, and t_{ad}, respectively. The adherend and adhesive Young's modulus and density are defined in Table 3.1. The approach presented in this paper for obtaining the material properties for the overlap region of a SLJ, is discussed in Section 3.3.

Applying the separation of variables approach to the transverse displacement of the beam, decomposes these displacements into its temporal and spatial components as follows:

$$w(x,t) = \sum_{r=1}^{\infty} \eta_r(t)\phi_r(x) \tag{3.11}$$

where, $\eta_r(t)$ and $\phi_r(x)$ are the rth modal displacement and mode shape function, respectively. As this formulation is applied to any mode, the subscript r is dropped for simplicity. Considering the spatial component of the transverse displacement, (3.11) is substituted into (3.7) and (3.8), written in terms of the mode shape function yields:

$$\frac{dV(x)}{dx} = -(\rho A)_j \omega^2 \phi(x), \quad \frac{d^2\phi(x)}{dx^2} = \frac{1}{(EI)_j} M(x), \quad \frac{dM(x)}{dx} = -V(x) \tag{3.12}$$

Writing (3.12) in matrix form, yields the state transition matrix:

$$\frac{d}{dx}\begin{Bmatrix} \phi \\ d\phi/dx \\ M \\ V \end{Bmatrix} = \begin{bmatrix} 0 & 1 & 0 & 0 \\ 0 & 0 & 1/(EI)_j & 0 \\ 0 & 0 & 0 & -1 \\ -(\rho A)_j \omega^2 & 0 & 0 & 0 \end{bmatrix} \begin{Bmatrix} \phi \\ d\phi/dx \\ M \\ V \end{Bmatrix} \tag{3.13}$$

where, the 4x4 constant state matrix of (3.13) is denoted $\mathbf{B_j}$. A solution to (3.13) is found from the linear systems theory [93], which gives the field transfer matrix $\mathbf{F_j}(\Delta x)$ for the jth beam segment as:

$$\mathbf{F_j}(\Delta x) = e^{\mathbf{B_j}\Delta x} \tag{3.14}$$

where, Δx represents the position considered along the length within the jth beam segment. The matrix exponential appearing in (3.14) is evaluated using the Cayley-Hamilton theory as follows:

$$e^{\mathbf{B_j}(\Delta x)} = c_0\mathbf{I} + c_1(\mathbf{B_j}\Delta x) + c_2(\mathbf{B_j}\Delta x)^2 + c_3(\mathbf{B_j}\Delta x)^3 \tag{3.15}$$

Substituting the constant state matrix, $\mathbf{B_j}$, into (3.15), the field transfer matrix is found using a software package Maple to perform symbolic manipulation, giving:

$$\mathbf{F_j}(\Delta x) = \begin{bmatrix} c_0 & \Delta x c_1 & \dfrac{(\Delta x)^2}{(EI)_j}c_2 & -\dfrac{(\Delta x)^3}{(EI)_j}c_3 \\ \dfrac{(\Delta x)^3(\rho A)_j\omega^2}{(EI)_j}c_3 & c_0 & \dfrac{\Delta x}{(EI)_j}c_1 & -\dfrac{(\Delta x)^2}{(EI)_j}c_2 \\ (\Delta x)^2(\rho A)_j\omega^2 c_2 & (\Delta x)^3(\rho A)_j\omega^2 c_3 & c_0 & -\Delta x c_1 \\ -\Delta x(\rho A)_j\omega^2 c_1 & -(\Delta x)^2(\rho A)_j\omega^2 c_2 & -\dfrac{(\Delta x)^3(\rho A)_j\omega^2}{(EI)_j}c_3 & c_0 \end{bmatrix} \tag{3.16}$$

where,

$$\begin{aligned} c_0 &= [\cosh(\beta\Delta x) + \cos(\beta\Delta x)]/2 \\ c_1 &= [\sinh(\beta\Delta x) + \sin(\beta\Delta x)]/2(\beta\Delta x) \\ c_2 &= [\cosh(\beta\Delta x) - \cos(\beta\Delta x)]/2(\beta\Delta x)^2 \\ c_3 &= [\sinh(\beta\Delta x) - \sin(\beta\Delta x)]/2(\beta\Delta x)^3 \end{aligned} \tag{3.17}$$

where, β represents the eigenvalues per unit length, which is defined as:

$$\beta^4 = \frac{(\rho \mathrm{A})_j\omega^2}{(EI)_j} \tag{3.18}$$

The field transfer matrix allows us to relate the state vector to different axial positions within the local beam element. Due to the semigroup property of this transfer matrix, we can find the global transfer matrix, by performing matrix multiplication on each individual field transfer matrix as follows:

$$\mathbf{U}(\omega) = \prod_{j=n}^{1} \mathbf{F_j}((\Delta x)_j, \omega) \tag{3.19}$$

which is used to relate the states at both the ends of the beam as follows:

$$\begin{Bmatrix} \phi(L_n) \\ d\phi(L_n)/dx \\ M(L_n) \\ V(L_n) \end{Bmatrix} = \mathbf{U}(\omega) \begin{Bmatrix} \phi(0) \\ d\phi(0)/dx \\ M(0) \\ V(0) \end{Bmatrix} \tag{3.20}$$

The characteristic equation of the system is contained within the global transfer matrix, which is found by imposing appropriate boundary conditions on the beam. Fixed-free boundary conditions are applied, as a cantilevered adhesive bonded SLJ is investigated. The boundary conditions for this configuration, assuming the fixed and free ends are located at positions $x = 0$ and $x = L_n$, respectively, are:

$$\phi(0) = \frac{d\phi(0)}{dx} = 0,\ M(L_n) = V(L_n) = 0 \tag{3.21}$$

where, n represents the number of beam segments. Substituting (3.21) into (3.20) and considering the third and fourth rows of the resulting system gives:

$$\begin{Bmatrix} 0 \\ 0 \end{Bmatrix} = \begin{bmatrix} U_{3,3} & U_{3,4} \\ U_{4,3} & U_{4,4} \end{bmatrix} \begin{Bmatrix} M(0) \\ V(0) \end{Bmatrix} \tag{3.22}$$

Equation (3.22) has a nonzero solution for M(0) and V(0) if and only if the reduced global transfer matrix is singular. Setting its determinant equal to zero yields a transcendental equation, which must be solved numerically to find the natural frequencies of the system.

The mode shapes are found by evaluating the displacements of each element evaluated at the corresponding resonant frequency. The internal bending moment and shear force are required to compute the mode shapes. From (3.22) the internal bending moment can be written in terms of the internal shear force as follows:

$$M(0) = -\frac{U_{3,4}}{U_{3,3}} V(0) \tag{3.23}$$

$V(0)$ then is a scaling factor for the mode shapes, and a convenient arbitrary value of 1 is assigned to it. Thus, the displacement amplitude at location x along the beam is found as follow:

$$\begin{Bmatrix} \phi(x) \\ d\phi(x)/dx \\ M(x) \\ V(x) \end{Bmatrix} = \prod_{j=x}^{1} \mathbf{F_j}((\Delta x)_j, \omega) \begin{Bmatrix} 0 \\ 0 \\ -U_{3,4}/U_{3,3} \\ 1 \end{Bmatrix} \tag{3.24}$$

Evaluating the first row of (3.24) at multiple positions along the beam yields the mode shapes. In this case, the displacement amplitudes for the mode shapes are computed at the same locations as the FE model.

3.3. Single Variable TMM Model Updating Approach

In order to model the overlap region of an adhesive bonded SLJ, we must determine its effective material properties. Since the thickness of the aluminum and adhesive is constant, we assume that the effective material properties within the overlap region must also be constant. The material properties, which must be determined, are the effective density, and effective Young's modulus.

A volume fraction approach is used to find the effective density, while a single variable model updating approach is used to obtain the effective Young's modulus. This constrains the material property ratio, which gives an effective density and an effective Young's modulus, which describe the true properties more accurately. The effective density of the overlap region is obtained as follows:

$$\rho_{eff} = 2V^* \rho + V_{ad}^* \rho_{ad} \tag{3.25}$$

where, V^* and V_{ad}^* are the volume fractions of the adherend and adhesive layers, respectively, given by:

$$V^* = \frac{V}{V_{ad} + 2V}, \quad V_{ad}^* = \frac{V_{ad}}{V_{ad} + 2V} \tag{3.26}$$

where, $V=lbt$ and $V_{ad}=lbt_{ad}$ are the volumes of the adherend and adhesive layers, respectively. Substituting these volumes into (3.25) and (3.26) yields:

$$\rho_{eff} = \frac{2t\rho + t_{ad}\rho_{ad}}{2t + t_{ad}} \tag{3.27}$$

It should be noted that the effective density found in equation (3.27) can be found from equation (3.9) by dividing by the cross-sectional area of the overlap region. Thus, the effective density determined by both the approaches is the same.

A model updating process intends to vary the effective Young's modulus such that an objective function is minimized. The second norm of the relative errors between the true natural frequencies and the TMM natural frequencies is chosen as the objective function as follows:

$$J = \sqrt{\sum_{r=1}^{k} \left(\frac{\omega_r - \omega_{r,0}}{\omega_{r,0}} \right)^2} \tag{3.28}$$

where, ω_r represents the r^{th} natural frequency computed using the TMM, $\omega_{r,0}$ represents the r^{th} true natural frequency of the system, and k represents the number of the natural frequency targets used for model updating. The Young's modulus corresponding to the minimum objective function is selected as the effective Young's modulus for the overlap region of the SLJ. It should be highlighted that the single variable TMM model updating approach and the additive TMM approach differ only in the way the effective Young's modulus for the overlap region of the SLJ are determined.

3.4. Simulation Results

The simulated dynamic characteristics of the SLJ specimens are shown for the FE model, the single variable TMM model updating approach, and the additive TMM approach. Specifically, this section presents the effects of the adhesive layer thickness, and overlap length on the natural frequencies and the effective material properties of the specimens. Since the effective Young's modulus of the single variable TMM model updating approach is found through model updating, the FE model natural frequencies are used as model updating targets in this chapter. In this way, the performance of the single variable TMM model updating approach to determining the effective material properties can be compared with the additive TMM approach. From hereafter, the term 'FE model natural frequencies' is used to refer to the natural frequencies obtained from the FE model. Further, the terms 'the single variable TMM model updating approach natural frequencies' and 'the additive TMM approach natural frequencies' are used to refer to the natural frequencies obtained by the single variable TMM model updating approach and the additive TMM approach respectively.

3.4.1. Effect of Adhesive Thickness

Consider an adhesive bonded SLJ cantilever beam shown in Figure 3.1, where the thickness of the adhesive layer, t_{ad}, is varied from 0.5 mm to 4 mm, incrementally by 0.5 mm. The overlap length, l_{ad}, is fixed at 40 mm. The first six transverse natural frequencies are first found by the FE model. The first four FE model natural frequencies are then used as model updating targets for the single variable TMM model updating approach, to determine the overlap region effective Young's modulus. Once the effective Young's modulus of the overlap region is found, the first six natural frequencies determined by the TMM are computed to see whether the fifth and sixth natural frequencies agree with the FE results. The effective Young's moduli determined by the single variable TMM model updating approach are compared with those determined by the additive TMM approach. The natural frequencies and mode shapes of each of the two TMM approaches are compared, using the FE model results as a benchmark for comparison.

The resulting FE model natural frequencies at each adhesive thickness are shown in Table 3.3. It can be seen that increasing the adhesive layer thickness causes a relatively modest reduction in the natural frequencies of the SLJ specimens. This is expected, since increasing the adhesive layer thickness causes an increase in the specimen's overall mass and decrease in the rigidity. Increasing the mass and deceasing the rigidity of a vibrating structure will result in a reduction in its resonant frequencies. It is noted that an increase of the adhesive layer thickness affects higher natural frequencies more than lower natural frequencies. For example, when the thickness is increased from 0.5 mm to 4.0 mm the relative reduction in the first natural frequency is 0.014% while for the sixth natural frequency is 0.145%.

Table 3.3: Natural frequencies determined by the FE model

Adhesive Thickness (mm)	Natural Frequencies (Hz)					
	f_1	f_2	f_3	f_4	f_5	f_6
0.5	7.64	45.51	133.25	257.25	428.22	638.89
1.0	7.63	45.05	132.93	255.45	425.70	634.00
1.5	7.61	44.65	132.63	253.92	423.38	628.51
2.0	7.60	44.28	132.34	252.46	421.01	621.22
2.5	7.58	43.91	132.05	251.05	418.48	610.30
3.0	7.57	43.56	131.75	249.65	415.71	593.43
3.5	7.55	43.21	131.45	248.27	412.59	570.68
4.0	7.54	42.87	131.14	246.89	409.00	545.96

Table 3.4 shows the effect of the adhesive layer thickness on the overlap region effective material properties using both the single variable TMM model updating and additive TMM approaches. Figure 3.6 displays the contrast between the two approaches. In general, increasing the adhesive thickness causes a reduction in the effective Young's modulus and density. This is expected as the adhesive material has a significantly lower Young's modulus and is less dense than the aluminum adherends. The second norm curves of the relative errors of the single variable TMM model updating approach are shown in Figure 3.7 for each of the adhesive layer thicknesses considered.

Table 3.4: Overlap region effective properties

Adhesive Thickness (mm)	Single Variable TMM Model Updating Young's Modulus (GPa)	Additive TMM Young's Modulus (GPa)	Effective Density (kg/m^3)
0.5	9.00	69.93	2,547
1.0	6.25	69.56	2,422
1.5	4.75	68.85	2,319
2.0	3.50	67.86	2,231
2.5	2.75	66.67	2,157
3.0	2.13	65.34	2,092
3.5	1.69	63.91	2,035
4.0	1.38	62.44	1,986

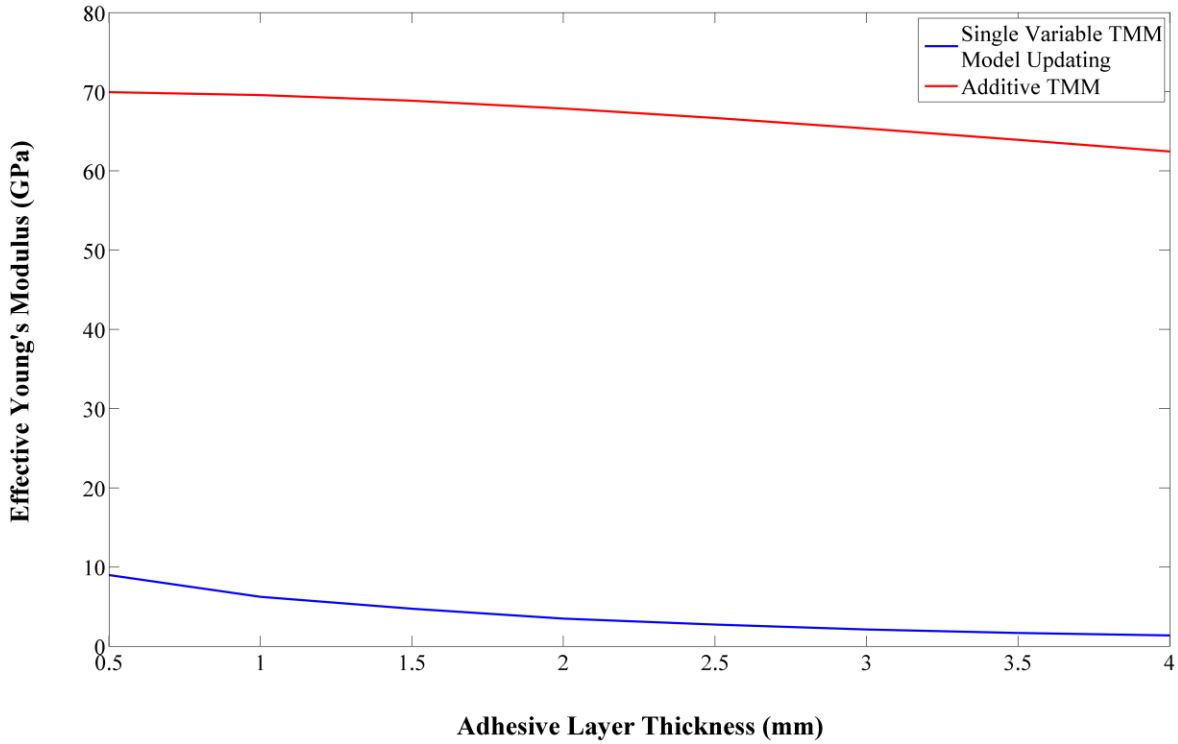

Figure 3.6: Effective Young's modulus comparison

The effective Young's moduli for the overlap region of the SLJ found by the single variable TMM model updating approach are significantly different from those found by the additive TMM approach. From Table 3.1, we can see that the Young's moduli of the adhesive and aluminum adherends are 7.31 MPa and 70 GPa, respectively. The single variable TMM model updating effective Young's moduli are significantly different from the aluminum and adhesive Young's moduli, whereas there is little difference between the additive TMM effective Young's moduli and the aluminum Young's modulus. This can be explained by the influence of the polar moment of inertia on the effective Young's modulus of the additive TMM approach. The polar moment of inertia of each adherend is relatively larger than the adhesive layer, since the aluminum layers are located further away from the neutral axis of the overlap region beam

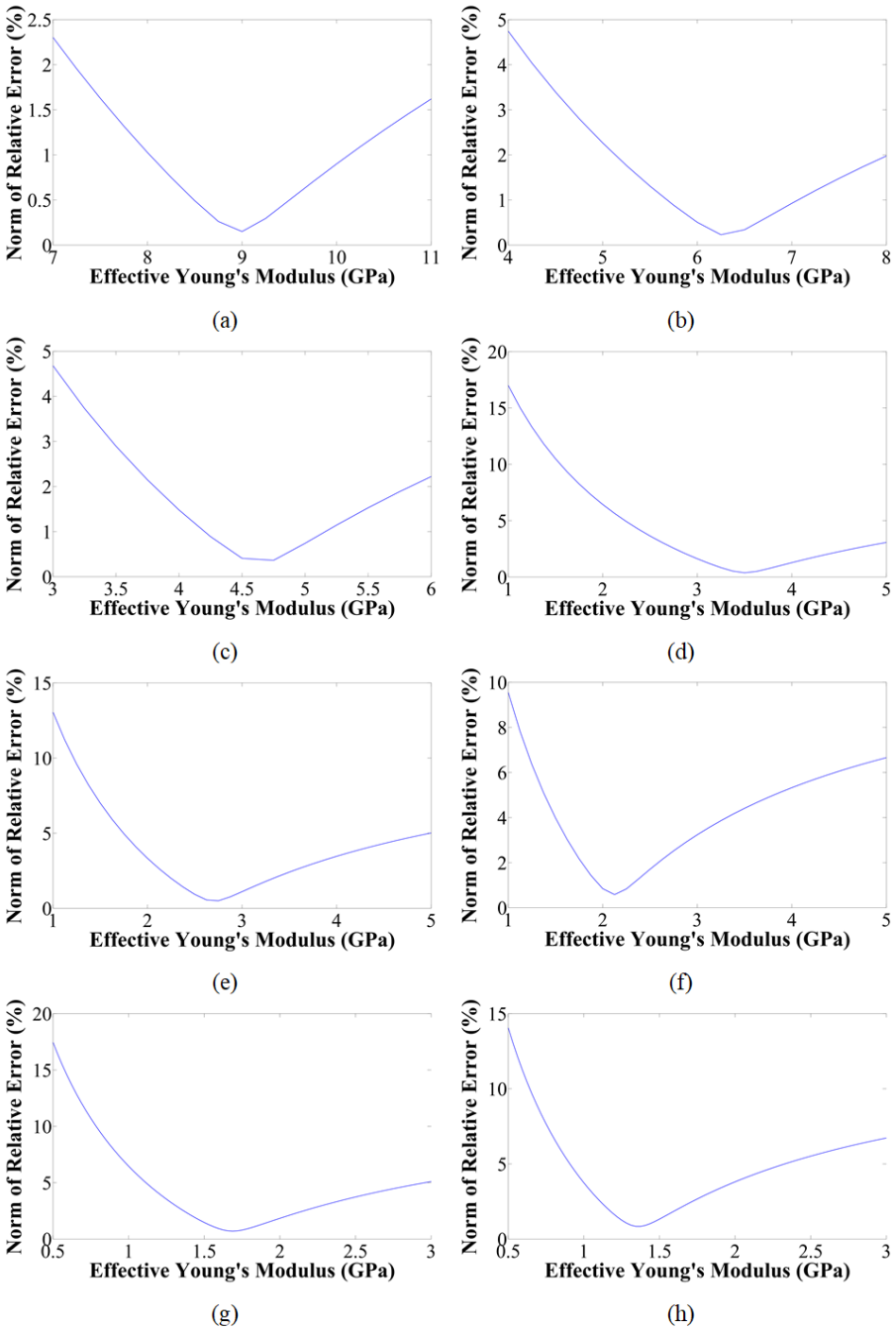

Figure 3.7: Objective function for adhesive thickness of: (a) 0.5 mm; (b) 1 mm; (c) 1.5 mm; (d) 2 mm; (e) 2.5 mm; (f) 3 mm; (g) 3.5 mm; (h) 4 mm

segment. As the adhesive layer thickness is increased, the local neutral axis of the aluminum layer is moved further away from the neutral axis of the overlap region segment. This increases the aluminum layer's polar moment of inertia, due to the parallel axis theorem, which significantly increases its contribution to the effective bending stiffness, EI_{eff}. This introduces a

bias towards the aluminum material properties, due to the geometry of the SLJ overlap region. Therefore, although increasing the adhesive thickness shows a decrease in the additive TMM effective Young's modulus compared with the aluminum Young's modulus, the drop is small. The single variable TMM model updating approach does not face this problem, as the effective Young's modulus of the overlap region is simply determined by minimizing the error between the computed natural frequencies and the true natural frequencies (FE in this case) of the structure. Thus, the geometric bias is avoided.

Table 3.5 and Table 3.6 show the resulting natural frequencies and relative errors of the single variable TMM model updating approach, respectively. The first four natural frequencies are particularly in close agreement with the FE model. From Table 3.6, it can be seen that the relative errors of the first four natural frequencies are less than 1%. This is mainly a result of the model updating scheme, which used the first four FE natural frequencies as error minimization targets. The fifth and sixth natural frequencies are of interest, since these were not used as model updating targets. In general, the fifth natural frequency shows close agreement with the FE model, with the largest absolute error of 2.577%. However, the relative error tends to increase with increasing adhesive thickness. This trend continues for the sixth natural frequency, where the single variable TMM model updating approach gives an absolute error greater than 5% for adhesive thicknesses larger than 2.5 mm. The greatest error magnitude is found to be 15.089% for an adhesive thickness of 4 mm. This demonstrates that the natural frequencies for higher modes of vibration can be found using the single variable TMM model updating approach, particularly for thinner adhesive layer thicknesses.

Table 3.5: Natural frequencies determined by the single variable TMM model updating approach

Adhesive Thickness (mm)	Natural Frequencies (Hz)					
	f_1	f_2	f_3	f_4	f_5	f_6
0.5	7.64	45.50	133.44	257.36	429.51	642.70
1.0	7.62	44.99	133.16	255.48	427.45	639.80
1.5	7.61	44.67	132.99	254.54	426.44	638.37
2.0	7.59	44.20	132.73	252.84	424.60	635.74
2.5	7.58	43.87	132.55	251.84	423.54	634.20
3.0	7.56	43.44	132.31	250.36	421.95	631.90
3.5	7.54	43.06	132.10	249.10	420.62	629.94
4.0	7.53	42.73	131.92	248.08	419.54	628.34

Table 3.6: Relative error of the single variable TMM model updating approach

Adhesive Thickness (mm)	Relative Error (%)					
	f_1	f_2	f_3	f_4	f_5	f_6
0.5	0.018	0.021	-0.142	-0.040	-0.303	-0.597
1.0	0.055	0.140	-0.173	-0.010	-0.412	-0.915
1.5	0.005	-0.040	-0.266	-0.245	-0.724	-1.568
2.0	0.070	0.178	-0.290	-0.148	-0.853	-2.337
2.5	0.048	0.095	-0.378	-0.317	-1.207	-3.917
3.0	0.098	0.263	-0.425	-0.284	-1.501	-6.483
3.5	0.123	0.343	-0.497	-0.337	-1.944	-10.385
4.0	0.118	0.323	-0.596	-0.485	-2.577	-15.089

The resulting resonant frequencies and relative errors from the additive TMM approach are shown in Table 3.7 and Table 3.8, respectively. Comparing the relative errors of the single variable TMM model updating approach with the additive TMM approach shows that the former consistently outperforms the latter. The relative errors of the additive TMM approach tend to increase with increasing adhesive thickness for all six modes of vibration. Interestingly, the first and third modes of vibration show reasonable agreement with the FE model, while the others show compare poorly. Apart from a 0.5 mm adhesive layer thickness, the relative errors of the second, fourth, fifth, and sixth natural frequencies have absolute relative errors greater than 5%. The maximum absolute error reported of 21.692% corresponds to the sixth modal frequency for

the 4 mm adhesive layer thickness. Thus, the single variable TMM model updating approach of determining the effective Young's modulus for the overlap region shows improved performance compared to the commonly used additive TMM approach.

Table 3.7: Natural frequencies determined by the additive TMM approach

Adhesive Thickness (mm)	Natural Frequencies (Hz)					
	f_1	f_2	f_3	f_4	f_5	f_6
0.5	7.77	48.25	134.97	271.91	447.34	667.06
1.0	7.76	48.08	134.89	271.85	447.39	667.19
1.5	7.75	47.87	134.79	271.63	447.22	667.02
2.0	7.74	47.65	134.68	271.30	446.91	666.66
2.5	7.73	47.42	134.56	270.92	446.51	666.18
3.0	7.72	47.18	134.45	270.49	446.07	665.62
3.5	7.71	46.95	134.33	270.05	445.59	665.02
4.0	7.70	46.71	134.22	269.60	445.09	664.39

Table 3.8: Relative error of the additive TMM approach

Adhesive Thickness (mm)	Relative Error (%)					
	f_1	f_2	f_3	f_4	f_5	f_6
0.5	-1.599	-6.025	-1.289	-5.699	-4.466	-4.409
1.0	-1.753	-6.709	-1.471	-6.420	-5.097	-5.235
1.5	-1.854	-7.203	-1.622	-6.975	-5.632	-6.126
2.0	-1.932	-7.616	-1.764	-7.462	-6.152	-7.314
2.5	-1.998	-7.986	-1.904	-7.914	-6.698	-9.156
3.0	-2.056	-8.329	-2.047	-8.349	-7.301	-12.166
3.5	-2.110	-8.655	-2.194	-8.775	-7.997	-16.532
4.0	-2.160	-8.970	-2.348	-9.200	-8.825	-21.692

3.4.2. Effect of Overlap Length

To investigate the effect of the overlap length on the dynamic behaviours of the SLJ specimens, the overlap length is varied, while the individual adherend lengths are fixed. Further, the general use of the effective Young's modulus, found by the single variable TMM model updating approach, is evaluated by varying the overlap region length. In this case, consider the

category A beams listed in Table 3.2. The overlap lengths are varied from 30 mm to 60 mm in 10 mm steps.

Increasing the overlap length causes an overall reduction in beam length, and an increase in the overall mass of the structure, since more adhesive is required for a larger overlap length. The natural frequencies of the structure are related to its mass and stiffness, where the stiffness in this case is dependent on overall beam length (since all other properties are fixed). The increased mass and decreased beam length, due to an increasing overlap length, has a conflicting impact on the natural frequencies of the specimens. Increasing mass typically causes a reduction in the natural frequencies, while decreasing overall beam length typically increases the specimen's stiffness, thus increasing the natural frequencies.

The FE model natural frequencies for the category A beam specimens are shown in Table 3.9. It can be seen that all of the natural frequencies increase with an increase in the SLJ overlap length, for the specimens considered. This suggests that the reduced overall length of the specimens with increasing overlap length has a greater impact on the natural frequencies than the increased adhesive mass. The increase in adhesive mass due to the increased overlap length is almost negligible relative to the specimen's overall mass. On the other hand, the reduction in overall length caused by the increase in overlap length is of greater significance. For example, consider beams 1A and 4A, whose overlap lengths are 30 mm and 60 mm, and overall specimen lengths are 495 mm and 465 mm, respectively. Beam 4A represents an approximate 6.1% reduction in overall length compared to beam 1A. Thus, the increase in natural frequencies with increasing overlap length in this case is reasonable to expect.

Table 3.9: Natural frequencies determined by the FE model for the category A specimens

Beam Specimens	Overlap Length (mm)	Natural Frequencies (Hz)					
		f_1	f_2	f_3	f_4	f_5	f_6
1A	30	7.30	42.94	127.53	242.01	404.84	595.56
2A	40	7.60	44.35	132.40	252.74	421.47	622.86
3A	50	7.91	45.76	137.38	263.75	438.28	647.93
4A	60	8.24	47.36	142.54	275.74	456.19	673.35

The effective material properties for both the single variable TMM model updating approach and additive TMM approach are listed in Table 3.10. For the additive TMM approach, the effective Young's modulus and effective density is the same for each category A specimen, since the adherend and adhesive thickness in the overlap region is fixed. The effective Young's modulus for the single variable TMM model updating approach is found for beam 2A, using the first four natural frequencies from the FE model as model updating targets. The effective material properties are then used in the TMM for the other category A beam specimens, to evaluate the general usability of the effective Young's modulus determined by the single variable TMM model updating approach. There is a significant difference between the effective Young's modulus of the single variable TMM model updating approach and the additive TMM approach, while the effective density is the same. This is expected considering the results from Section 3.4.1.

Table 3.10: Overlap region effective material properties

Effective Density	2,248 kg/m^3
Single Variable TMM Model Updating Young's Modulus	3.75 GPa
Additive TMM Young's Modulus	68.08 GPa

The single variable TMM model updating natural frequencies of the category A specimens are shown in Table 3.11. Table 3.12 shows the relative errors of the natural frequencies for each specimen compared to the FE model. The relative errors show that the single variable TMM model updating approach performs well compared to the FE model, with a maximum absolute error of 3.223% given by the sixth natural frequency of beam specimen 1A. The minimum absolute error of 0.035% is given by the fundamental frequency of beam specimen 2A, which is expected since the effective Young's modulus is found using model updating for beam 2A. These results suggest that the effective Young's modulus found by the single variable TMM model updating approach can be used when the overlap length is varied. Interestingly, the fifth and sixth natural frequency of the specimens tend to compare better with the FE model as the overlap length is increased.

Table 3.11: Natural frequencies determined by single variable TMM model updating for the category A specimens

Beam Specimens	Overlap Length (mm)	Natural Frequencies (Hz)					
		f_1	f_2	f_3	f_4	f_5	f_6
1A	30	7.32	43.37	128.09	244.99	410.81	614.75
2A	40	7.60	44.32	132.80	253.32	425.12	636.49
3A	50	7.89	45.39	137.66	262.52	440.05	658.37
4A	60	8.21	46.58	142.65	272.50	455.52	680.16

Table 3.12: Relative errors of the single variable TMM model updating for the category A specimens

Beam Specimens	Overlap Length (mm)	Relative Error (%)					
		f_1	f_2	f_3	f_4	f_5	f_6
1A	30	-0.262	-0.994	-0.439	-1.229	-1.476	-3.223
2A	40	0.035	0.060	-0.302	-0.231	-0.866	-2.188
3A	50	0.223	0.816	-0.202	0.467	-0.404	-1.612
4A	60	0.422	1.651	-0.076	1.173	0.147	-1.011

Table 3.13 and Table 3.14 show the resulting natural frequencies and relative errors, respectively, of the additive TMM approach. Considering the relative errors for the first and third natural frequencies, the additive TMM approach gives a maximum absolute relative error of 3.121% compared with the FE model. However, the remaining natural frequencies give absolute relative errors greater than 4%, with a maximum absolute relative error of 11.609% found for the second natural frequency of beam 4A. Furthermore, the relative errors tend to increase with increasing overlap length for each natural frequency, which contrasts with the fifth and sixth natural frequencies from the single variable TMM model updating approach. Comparing these results with those of the single variable TMM model updating approach shows that the latter outperforms the additive TMM approach for all natural frequencies.

Table 3.13: Natural frequencies determined by the additive TMM for the category A specimens

Beam Specimens	Overlap Length (mm)	Natural Frequencies (Hz)					
		f_1	f_2	f_3	f_4	f_5	f_6
1A	30	7.42	45.64	129.24	257.02	424.27	634.33
2A	40	7.74	47.69	134.70	271.37	446.98	666.74
3A	50	8.09	50.09	140.59	287.65	473.31	702.78
4A	60	8.46	52.86	146.99	305.91	504.23	743.54

Table 3.14: Relative errors of the additive TMM for the category A specimens

Beam Specimens	Overlap Length (mm)	Relative Error (%)					
		f_1	f_2	f_3	f_4	f_5	f_6
1A	30	-1.698	-6.272	-1.344	-6.199	-4.799	-6.510
2A	40	-1.920	-7.542	-1.739	-7.374	-6.052	-7.044
3A	50	-2.281	-9.447	-2.337	-9.061	-7.993	-8.466
4A	60	-2.668	-11.609	-3.121	-10.943	-10.532	-10.423

Mode shapes determined by the FE model, single variable TMM model updating approach, and additive TMM approach are shown in Figure 3.8 and Figure 3.9. For brevity, only the first, second, and fifth mode shapes of beams 1A and 4A are shown. In general, the mode shapes of both the TMM approaches compare well with the FE mode shapes for all category A beams, with the single variable TMM model updating approach giving slightly better performance. This can be seen for the fifth mode in particular, as the additive TMM approach shows significant deviation from the FE mode shapes. Due to the relatively stiff overlap region found by the additive TMM approach, the overlap region is more difficult to bend than the rest of the beam. The relatively high bending stiffness of the overlap region found by the additive TMM approach has a noticeable impact on the mode shapes of the beams. The negligible change in slope in the overlap region of beam 4A suggests that little bending occurs relative to the rest of the beam. This is best seen in the second mode shape between positions 177 mm and 228 mm. On the other hand, the single variable TMM model updating approach gives a significantly lower bending stiffness for the overlap region. This gives an overlap region which is more susceptible to bending, which tends to agree better with the FE model than the additive TMM approach.

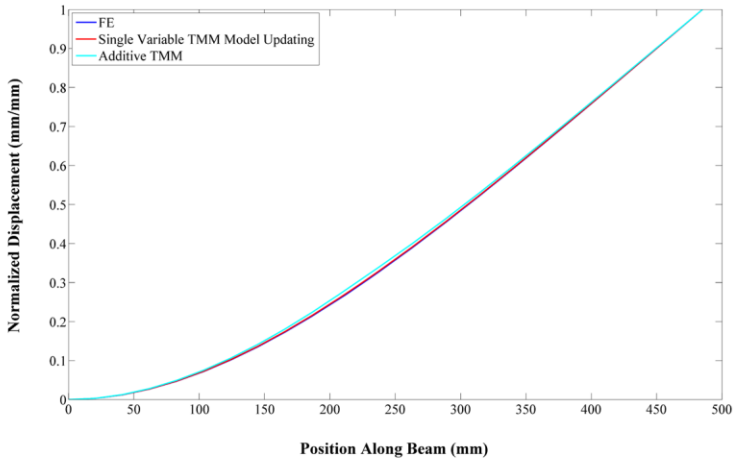

(a)

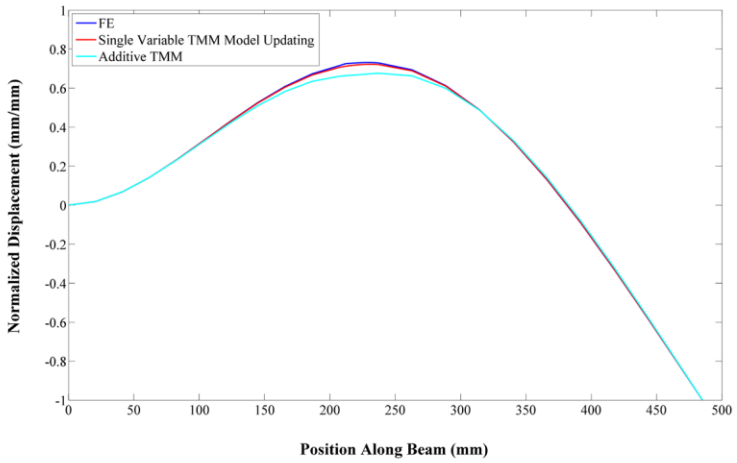

(b)

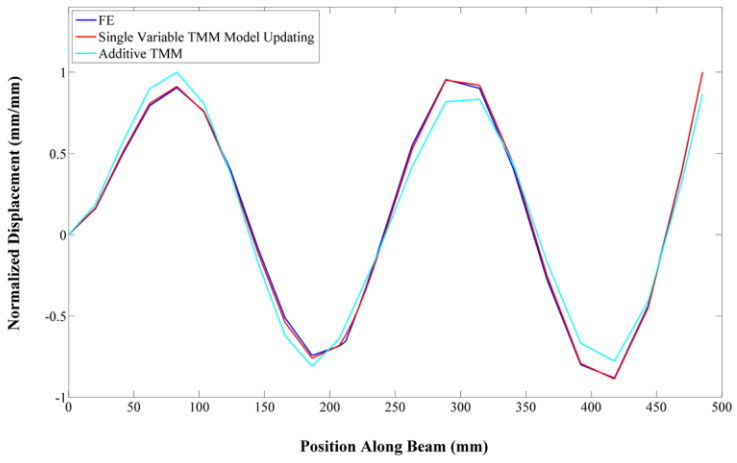

(c)

Figure 3.8: Beam 1A mode shapes: (a) mode 1; (b) mode 2; (c) mode 5

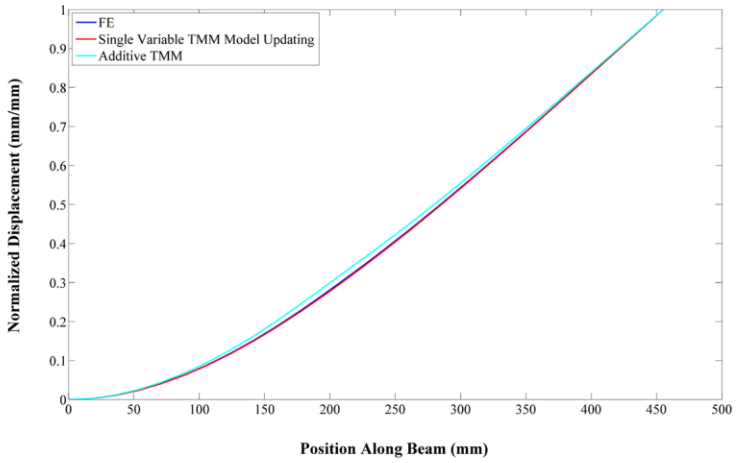

(a)

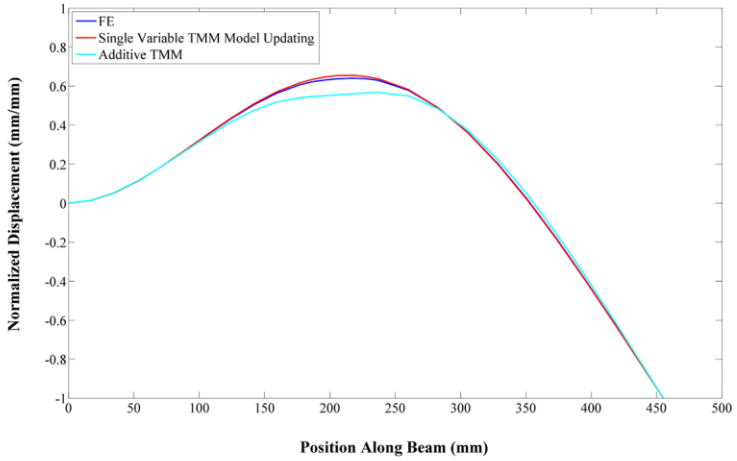

(b)

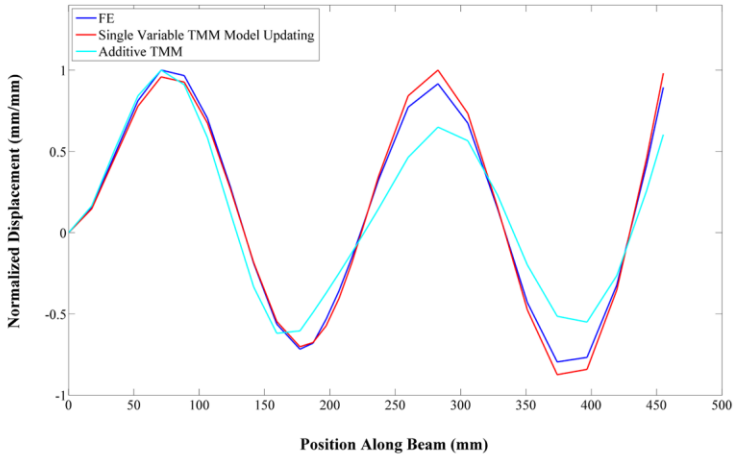

(c)

Figure 3.9: Beam 4A mode shapes: (a) mode 1; (b) mode 2; (c) mode 5

3.4.3. General Use of the Effective Young's Modulus

This section further investigates the general use of the effective Young's modulus found by the single variable TMM model updating approach. From Table 3.2 it can be seen that the adherend and adhesive thicknesses of the category A and B specimens differ. However, both the category A and B specimens have the same adherend to adhesive thickness ratio of 1.16. The effective Young's modulus found for beam 2A using the single variable TMM model updating approach in Section 3.4.2 is used in the TMM for the category B specimens. Thus, the general use of the effective Young's modulus is evaluated for specimens with the same overlap adherend to adhesive thickness ratio. Although model updating is not used in this section, the FE model is still used as a benchmark for comparison.

The effective material properties of the additive TMM approach are determined for each specimen by equation (3.9) and (3.10). Since the adherend to adhesive thickness ratio is the same for both the category A and B specimens, the effective material properties determined by the additive TMM approach are the same for both the categories (i.e. an effective density and Young's modulus of 2,248 kg/m^3 and 68.08 GPa, respectively). This can be seen by defining an adherend to adhesive thickness ratio, *r*, and solving for the effective density and Young's modulus in equations (3.9) and (3.10). The adherend to adhesive thickness ratio, overlap region area, and polar moment of inertia are as follows:

$$r = \frac{t}{t_{ad}} \tag{3.29}$$

$$A = b(2t + t_{ad}) \tag{3.30}$$

$$I = \frac{1}{12} b\left(2t + t_{ad}\right)^3 \tag{3.31}$$

Substituting equation (3.29) into equations (3.9), (3.10), (3.30), and (3.31), and solving for the effective density and Young's modulus yields:

$$\rho_{eff} = \frac{2\rho r + \rho_{ad}}{2r + 1} \tag{3.32}$$

$$E_{eff} = \frac{E_{ad} + 2E\left[r^3 + 3r\left(1+r\right)^2\right]}{\left(2r+1\right)^3} \tag{3.33}$$

Through equations (3.32) and (3.33) we can see that the effective Young's modulus and density depend upon the adherend to adhesive thickness ratio. The results from the additive TMM approach are presented for the purpose of comparison.

Table 3.15 shows the FE model natural frequencies for the category B specimens. Increasing the overlap region length causes an increase in the natural frequencies of each specimen, like the findings in Section 3.4.2. It can be seen that the natural frequencies of the category B specimens are significantly lower than the natural frequencies of the category A specimens from Table 3.9. This is due to the thinner adherend and adhesive thicknesses of the category B specimens, which causes a significant reduction in beam stiffness.

Table 3.15: Natural frequencies determined by the FE model for the category B specimens

Beam Specimens	Overlap Length (mm)	Natural Frequencies (Hz)					
		f_1	f_2	f_3	f_4	f_5	f_6
1B	30	5.32	31.57	93.05	178.13	297.87	444.46
2B	40	5.54	32.49	96.56	185.40	309.52	461.80
3B	50	5.77	33.56	100.25	193.59	322.08	479.65
4B	60	6.01	34.82	104.09	202.73	335.76	498.31

Table 3.16 and Table 3.17 show the resulting natural frequencies and relative errors, respectively, of the TMM using the effective Young's modulus determined by the single variable TMM model updating approach for beam 2A. Interestingly, the absolute maximum relative error of the category A specimens, from Table 3.12, is greater than the category B specimens, reporting 3.223% and 2.626% respectively. This may be explained by the model updating process. The maximum error for the category A specimens is found to occur to the sixth natural frequency of beam 1A. The fifth and sixth natural frequencies are impacted by the overall error minimization of the first four natural frequencies of beam 2A, since the fifth and sixth natural frequencies are not used during model updating. The maximum error for the category B specimens is reported in the third natural frequency of specimen 4B. Thus, although the absolute

maximum relative error is reduced, the relative error within the first four natural frequencies of the category B specimens is negatively impacted. With that said, the resulting natural frequencies determined by the TMM for the category B specimens using the effective material properties of beam 2A, are in good agreement with the FE model. This suggests that the effective material properties determined by the single variable TMM model updating approach can be used in general when the adherend to adhesive thickness ratio is the same.

Table 3.16: Natural frequencies of the TMM using the effective Young's modulus from beam 2A for the category B specimens

Beam Specimens	Overlap Length (mm)	Natural Frequencies (Hz)					
		f_1	f_2	f_3	f_4	f_5	f_6
1B	30	5.32	31.55	93.16	178.24	298.85	447.20
2B	40	5.53	32.25	96.59	184.34	309.29	463.06
3B	50	5.74	33.03	100.13	191.06	320.19	479.04
4B	60	5.97	33.91	103.76	198.35	331.50	494.96

Table 3.17: Relative errors of the TMM for the category B specimens

Beam Specimens	Overlap Length (mm)	Relative Error (%)					
		f_1	f_2	f_3	f_4	f_5	f_6
1B	30	0.057	0.058	-0.125	-0.060	-0.328	-0.616
2B	40	0.233	0.735	-0.025	0.576	0.074	-0.272
3B	50	0.499	1.571	0.113	1.308	0.585	0.127
4B	60	0.685	2.626	0.308	2.160	1.268	0.672

The natural frequencies for the category B specimens, found by the additive TMM approach, are listed in Table 3.18. Table 3.19 shows the natural frequency relative errors between the FE model and the additive TMM approach. Like Section 3.4.2, the natural frequencies of the category B specimens increase with increasing overlap region length, along with their corresponding relative errors compared to the FE model. Comparing the relative errors found by the additive TMM approach with those by the TMM using the effective Young's modulus of beam 2A, the latter outperforms the former for all frequencies of the beam specimens considered. Further, the absolute maximum relative error from the additive TMM approach is nearly four times larger in magnitude, at 10.372%, than that from the TMM using the effective

Young's modulus of beam 2A. This is particularly significant, since the effective materials properties used by the latter were the same as the category A specimens. Thus, although model updating was not directly used for the category B specimens, the performance of the effective Young's modulus determined by the single variable TMM model updating approach for beam 2A significantly outperforms the additive TMM approach.

Table 3.18: Natural frequencies determined by the additive TMM for the category B specimens

Beam Specimens	Overlap Length (mm)	Natural Frequencies (Hz)					
		f_1	f_2	f_3	f_4	f_5	f_6
1B	30	5.40	33.19	93.99	186.91	308.55	461.32
2B	40	5.63	34.68	97.96	197.35	325.06	484.89
3B	50	5.88	36.42	102.24	209.19	344.22	511.10
4B	60	6.15	38.43	106.89	222.47	366.71	540.74

Table 3.19: Relative errors of the additive TMM for the category B specimens

Beam Specimens	Overlap Length (mm)	Relative Error (%)					
		f_1	f_2	f_3	f_4	f_5	f_6
1B	30	-1.357	-5.108	-1.018	-4.925	-3.583	-3.792
2B	40	-1.695	-6.736	-1.444	-6.443	-5.021	-4.999
3B	50	-1.969	-8.510	-1.995	-8.058	-6.874	-6.557
4B	60	-2.360	-10.372	-2.696	-9.738	-9.218	-8.514

The first, second, and fifth mode shapes of beams 1B and 4B are shown in Figure 3.10 and Figure 3.11, respectively, for each of the numerical methods used. Like the category A specimens, the TMM using the effective Young's modulus from beam 2A compares slightly better with the FE mode shapes than the additive TMM approach, particularly for the fifth mode shape. This is particularly noteworthy since model updating was not used for the overlap region effective material properties of the category B specimens. This further shows the general usability of the effective Young's modulus found by the single variable TMM model updating approach, when the adherend to adhesive thickness ratio is the same. Like Section 3.4.2, the second mode shape shows that the overlap region bending stiffness of the additive TMM approach is significantly higher than the TMM using the effective Young's modulus of beam 2A.

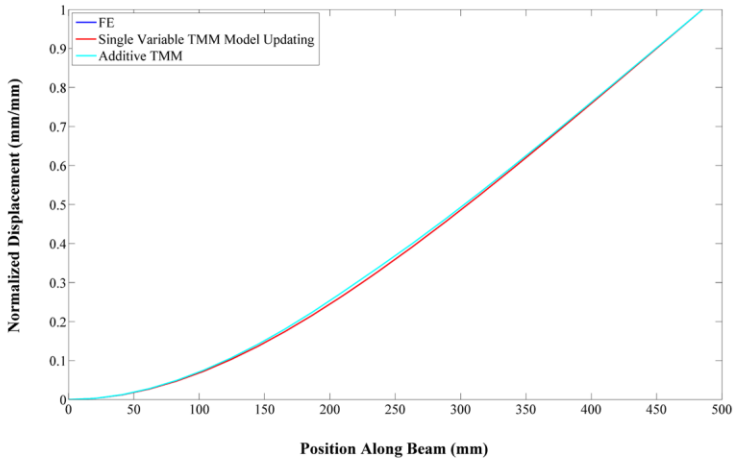

(a)

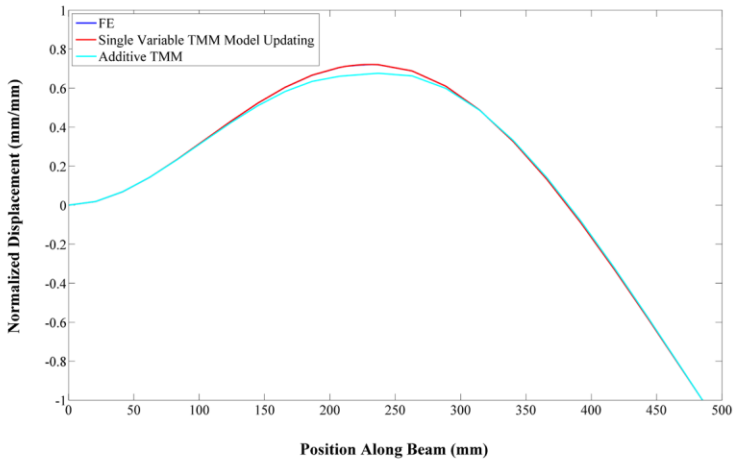

(b)

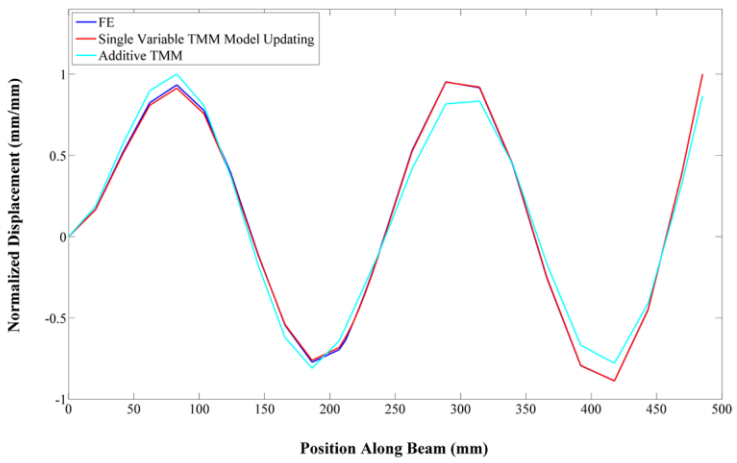

(c)

Figure 3.10: Beam 1B mode shapes: (a) mode 1; (b) mode 2; (c) mode 5

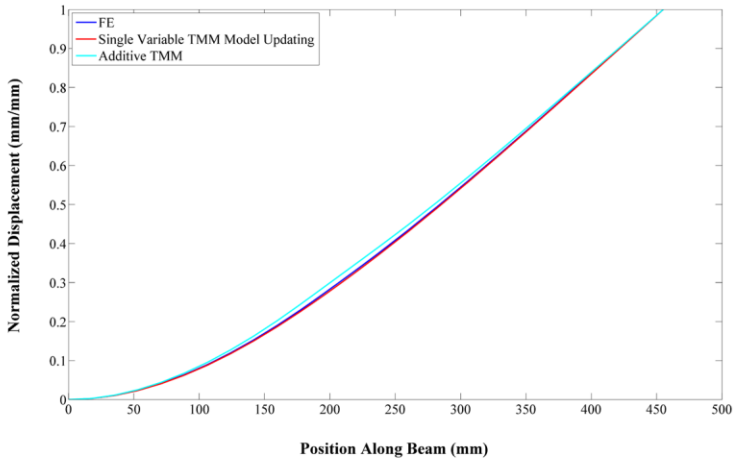

(a)

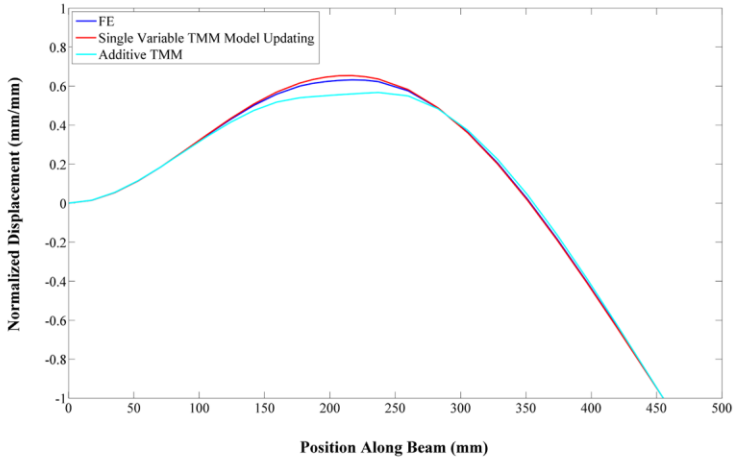

(b)

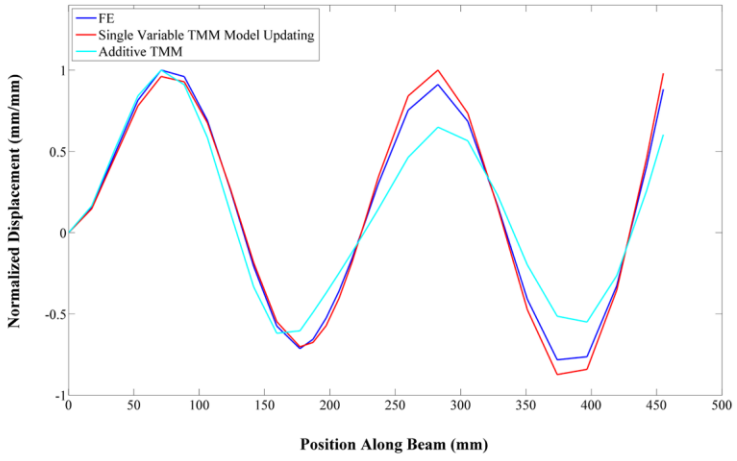

(c)

Figure 3.11: Beam 4B mode shapes: (a) mode 1; (b) mode 2; (c) mode 5

3.5. Conclusion

This chapter considers the dynamic single physics scenario, to determine the dynamic behaviours of an adhesive bonded SLJ cantilever beam. The effects of adhesive layer thickness, and the overlap length on the dynamic behaviours have been studied. It is found that increasing the adhesive thickness causes a reduction in the specimen's natural frequencies, while increasing the overlap length causes an increase in the specimen's natural frequencies. Further, the performance of the single variable TMM model updating approach has been compared with the additive TMM approach. For comparison sake, the FE model has been used as a benchmark to compare their performance. The effective Young's modulus determined by the single variable TMM model updating approach consistently outperforms the additive TMM approach. The robustness and general use of the effective Young's modulus from the single variable TMM model updating approach has been investigated. The effective material properties are shown to be robust, and their general usability is shown when the adherend to adhesive thickness ratio of the overlap region is maintained.

Chapter 4 Experimental Evaluation of the Numerical Analysis Results

In this chapter, the dynamic behaviours of adhesive bonded SLJs are measured experimentally to evaluate the performance of the numerical analysis approaches from Chapter 3. Category A and B specimens are investigated in this chapter, to validate the effects of overlap length, and the presence of an overlap region adherend to adhesive thickness ratio. The iterative design and benchmarking of an experimental testing apparatus are presented. This apparatus differs slightly from those reported in the literature of adhesive bonding, since optical non-contact position sensors are used for measurement, eliminating the effect of the added mass from accelerometers. Data collection is discussed, along with signal processing techniques used to remove noise from the collected data, thus improving the quality of the results. The experimental apparatus is used to determine the transmissibility function, natural frequencies, damping ratios, and mode shapes of the adhesive bonded SLJ specimens, to validate the numerical models. Further, the measured damping ratios used to tune the Rayleigh damping criterion are presented, and the Rayleigh damping tuning is discussed.

4.1. Experimental Apparatus

To measure the dynamic behaviours of the SLJ specimens, the specimens need to be excited harmonically. There are two kinds of excitation: direct force excitation and base excitation. In order to achieve the direct force excitation, an apparatus is designed using a shaker to apply force to the specimen, and optical position sensors are used to measure the displacement amplitudes of the specimen. It is important to ensure that the apparatus gives accurate measurements, and that contamination from the excitation system is minimized. Thus, the apparatus is benchmarked using a well-known and established analytical approach, to validate its performance. The iterative design and validation of the apparatus is detailed in the following. The equipment used for data collection is discussed, along with the signal processing techniques used to process and remove noise from the collected data.

Benchmarking of the apparatus is done by measuring the natural frequencies and mode shapes of an aluminum cantilever beam of constant rectangular cross section throughout. For clarity, this aluminum beam is called the benchmark beam in the remainder of this chapter. The benchmark beam is shown in Figure 4.1, while its material properties are the same as the

adherend material properties listed in Table 3.1 from Chapter 3. In this case, we can apply the Euler-Bernoulli beam theory as the benchmark to evaluate the performance of the apparatus. The Euler-Bernoulli beam theory is a well-established analytical formulation which can be used to find the natural frequencies and modes shapes of continuous thin beam structures. The thin beam criterion is satisfied if the beam has a ratio of $l/t \geq 10$, which the benchmark beam gives 302.5. Thus, the apparatus can be validated with confidence. For a beam with fixed-free boundary conditions, the Euler-Bernoulli beam theory gives the natural frequencies and mode shapes as follows [90]:

$$\omega_n = \beta_n^2 \sqrt{\frac{EI}{\rho A}} \tag{4.1}$$

$$X_n(x) = \cosh \beta_n x - \cos \beta_n x - \sigma_n (\sinh \beta_n x - \sin \beta_n x) \tag{4.2}$$

where, X_n, σ_n, ω_n, and β_n represent the mode shape, mode shape constant, natural frequency, and eigenvalue per unit length of the n^{th} vibration mode, respectively. The position along the beam is represented by x. The eigenvalue per unit length and mode shape constant are dependent on boundary conditions. These are tabulated in Table 4.1 for the first three modes of vibration for the fixed-free boundary condition.

Table 4.1: Weighted frequencies and mode shape constants of a fixed-free beam

Vibration Mode	Weighted Frequency, $\beta_n l$	Mode Shape Constant, σ_n
1	1.87510407	0.7341
2	4.69409113	1.0185
3	7.85475744	0.9992

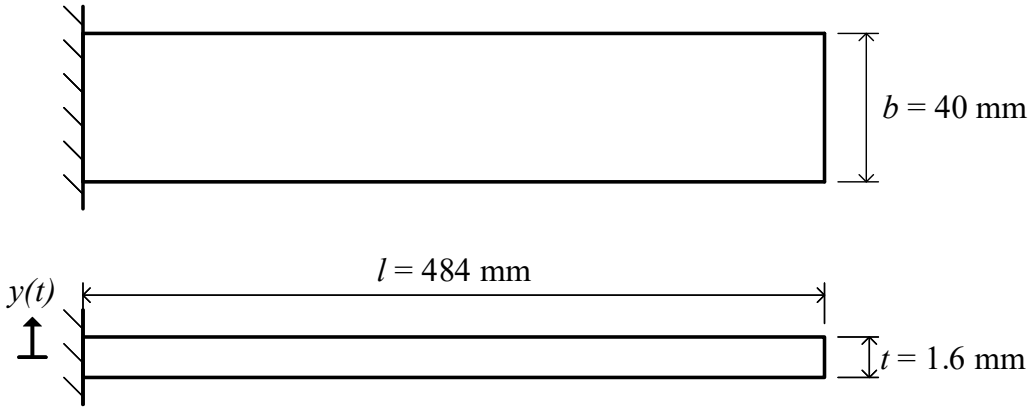

Figure 4.1: Benchmark beam geometry (not drawn to scale)

4.1.1. Experimental Data Collection

The experimental measurements are collected using the equipment shown in Figure 4.2 below. The key components of the measurement and data collection system are labeled accordingly. The computer provides the user interface allowing the user to send outputs, and record the measurement data. A Brüel & Kjær data acquisition unit (model 2827-002) is used to convert analog signals into digital ones and digital signals to analog ones. A software package Pulse by Brüel & Kjær allows the computer to communicate with the data acquisition unit. The amplifier amplifies the output signal from the data acquisition unit to adequately power the shaker. The shaker is a linear electromagnetic motor, and is used as the excitation system, which subjects the specimen under test to forced harmonic excitation. Two Wenglor optical position sensors (model CP24MHT80) measure the displacement of the beam at locations of interest for data collection. Finally, the power supply converts AC to DC power in order to power the optical position sensors.

Specimen transmissibility functions relate the input excitation displacement acting on the specimen, to the output measured at a location of interest, over a given frequency range. Further, the transmissibility function can be used to identify the damped resonant frequencies and modal damping ratios of the structure under test. Since the specimens have fixed-free boundary conditions, the output displacement at the free end of the beam is of interest. Therefore, the displacement of the free end and input excitation location are measured with optical position sensors. The transmissibility function is found as follows:

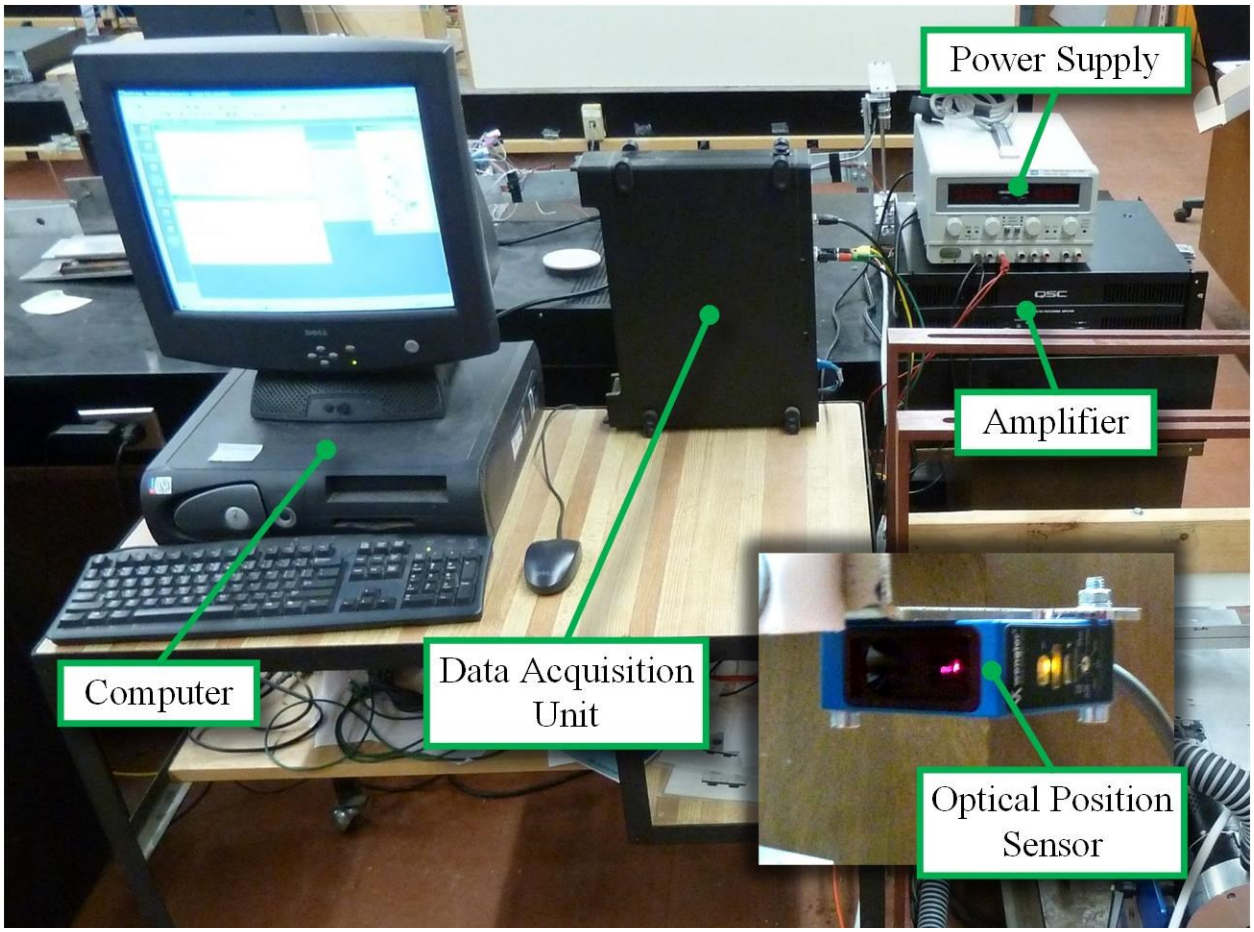

Figure 4.2: Data collection equipment

$$TR(\omega) = \frac{x_{12}(\omega)}{x_0(\omega)} \tag{4.3}$$

where, $TR(\omega)$, $x_{12}(\omega)$, and $x_0(\omega)$ represent the TR, output displacement, and input displacement, respectively, at a given excitation frequency, ω. The notations of the output and input displacements are consistent with the sensor positions shown in Figure 4.3 to measure the mode shapes. Since the measured displacement of the input and output is oscillatory, their RMS amplitude is used to compute the transmissibility functions and mode shapes of the specimen under test. The transmissibility function then represents the TRs over the given frequency range. To ensure that the first three vibration modes are measured, the frequency range considered for this study is 1 Hz - 150 Hz. For the frequency sweeping test, like the FE model, the frequency resolution near resonant frequencies is 0.25 Hz, and 2 Hz elsewhere, to reduce the time required for data collection.

The displacement data is collected by performing an excitation frequency sweep over the frequency range of interest. The time duration for an individual exciting frequency must allow the beam's response to achieve steady state. As the driving frequency changes, the transient response is induced. Data is collected over a two second time interval once the response has reached steady state. The sampling frequency of the experiment is 512 Hz, which means that the measured displacements are recorded approximately every 1.953 ms.

The mode shapes of the specimen under test are found by exciting the specimen at the corresponding natural frequency, and measuring the displacement amplitudes of the specimen at various locations. The measurement locations are selected along the centerline of the specimen. It is important to use a suitable number of measurement positions to measure the mode shapes of the specimens. Increasing the number of measurement positions increases the resolution of the mode shapes. However, there is a trade-off between the mode shape resolution and the amount of time required to measure the mode shapes. Since one optical position sensor is used to measure the displacement amplitude of the structure under test, the displacement amplitude of each position must be measured one by one. Thus, a balance between mode shape resolution and data collection time must be considered. Therefore, a total of twelve measurement positions are used. This is suitable, since the first three modes of vibration are measured within the frequency range used for the experiment. Figure 4.3 shows the general locations of the measurement positions. The measurement position x_{12} corresponds to the location used to measure the TR of the specimen; 10 mm from the free end. The remaining measurement locations are spaced 40 mm apart. The displacement of the base is also measured, such that the relative displacements can be found. The resulting mode shapes are normalized for comparison with the numerical solutions.

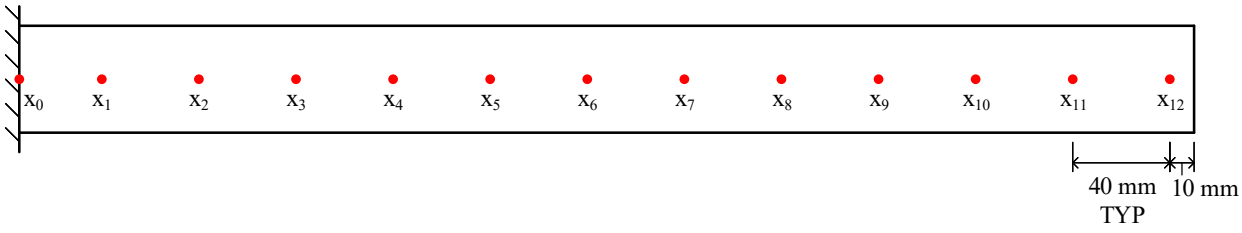

Figure 4.3: General sensor positions for all specimens (not drawn to scale)

The modal damping ratios are evaluated from the transmissibility functions. This method measures the magnitude of damping based on the steepness and magnitude of the resonant frequencies. To extract the modal damping ratios of the specimen, we use the quadrature peak picking method illustrated in Figure 4.4, and computed as follows [90]:

$$TR(\omega_a) = TR(\omega_b) = \frac{TR(\omega_d)}{\sqrt{2}} \tag{4.4}$$

where, $TR(\omega_d)$ represents the magnitude of the transmissibility function at the damped resonant frequency of interest (ω_d), and $TR(\omega_a)$ and $TR(\omega_b)$ represent the 3-dB down point magnitude of the corresponding excitation frequencies ω_a and ω_b. By calculating the magnitude of the 3-dB down point, the corresponding excitation frequencies are found, using interpolation if necessary. The damping ratios are then computed as follows [90]:

$$\zeta = \frac{\omega_b - \omega_a}{2\omega_d} \tag{4.5}$$

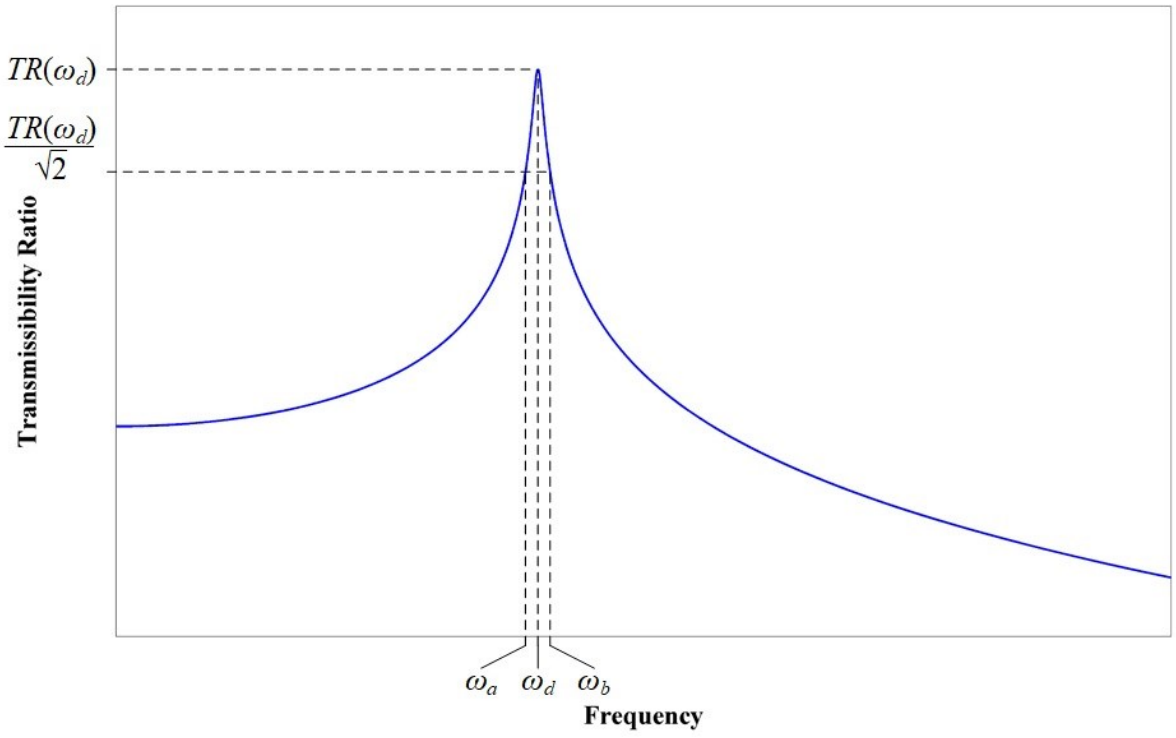

Figure 4.4: Quadrature peak picking method

4.1.2. Signal Processing and Analysis

One of the challenges of conducting the experiment is noise, whether it is introduced by the physical apparatus or the data collection equipment used. Regardless of the sources, noise can contaminate the collected data to a varying degree and should be minimized where possible. Although noise reduction is a consideration in the design of the experiment, there is typically some level of noise present in the measured data. During post-processing, a filter may be applied to the measured data to remove noise and improve the quality of the data.

There are many design considerations when using a filter to remove noise from the collected data, including its classification, frequency response, cut-off frequency and filter order. A Butterworth filter is selected. In this case, either a lowpass or bandpass frequency response is selected. Applying the filter to the measured data associated with frequencies lower than 10 Hz, a lowpass frequency response is used to eliminate high frequency noise contamination. For frequencies greater than or equal to 10 Hz, a bandpass frequency response is used to eliminate both low and high frequency noise contamination. The cut-off frequency of the lowpass filter is equal to the driving frequency of the data sample plus 6 Hz. The bandpass filter requires two cut-off frequencies, which correspond to plus and minus 3 Hz of the driving frequency. For example, for a driving frequency of 20 Hz, the bandpass cut-off frequencies are 17 Hz and 23 Hz. The filter order is selected as 8 and 3 for the lowpass and bandpass filters respectively.

In addition to filtering the data, zero padding is a post-processing technique which can improve the frequency spectrum quality. Zero padding is similar to applying a rectangular window function to the measured data in its advantages and disadvantages. Applying a rectangular window would mean that the data within the window is preserved, while the data outside of the window is zeroed. However, zero padding involves appending a large number of zeros to the measured data, such that the measured data is preserved. In our application, zero padding is a better option, especially in the lower frequency range, since only two cycles would be recorded over the two second sampling duration for a driving frequency of 1 Hz. The main advantages include the prevention of spectral leakage, improved frequency spectrum resolution, and preservation of the frequency spectrum magnitude within the passband of the filter. The main disadvantage is the presence of side lobes on either side of the exciting frequency. The sampling duration and frequency of the experiment results in 1,024 samples per driving

frequency. Zeros are appended to the measured data by sixteen times the number of samples (16,384).

Comparisons of the raw and post-processed (filtered and zero padded) time response and frequency spectrum for Beam 1A excited at a driving frequency of 30 Hz are shown in Figure 4.5 to Figure 4.7. Figure 4.5(a) shows the raw time response of the specimen, which contains a significant amount of noise. It can be seen in Figure 4.6(a) that the main contributors to the noise seen in the time response are low and high frequency components of 7 Hz and 90 Hz respectively. It can be seen in Figure 4.5(b) that the time response is quite smooth, and there is an imperceptible amount of noise after post-processing. The reason for this can be seen in Figure 4.6(b), where the blue and green lines represent the post-processed frequency spectrum and the bandpass filter, respectively. The main noise contributors from Figure 4.6(a) have been removed after post-processing. Figure 4.7(a) to (b) show a detailed view of the raw and post-processed frequency spectrum, respectively. The resolution of the post-processed frequency spectrum is finer than the raw spectrum. Further, the characteristic side lobes due to zero padding can be seen in Figure 4.7(b).

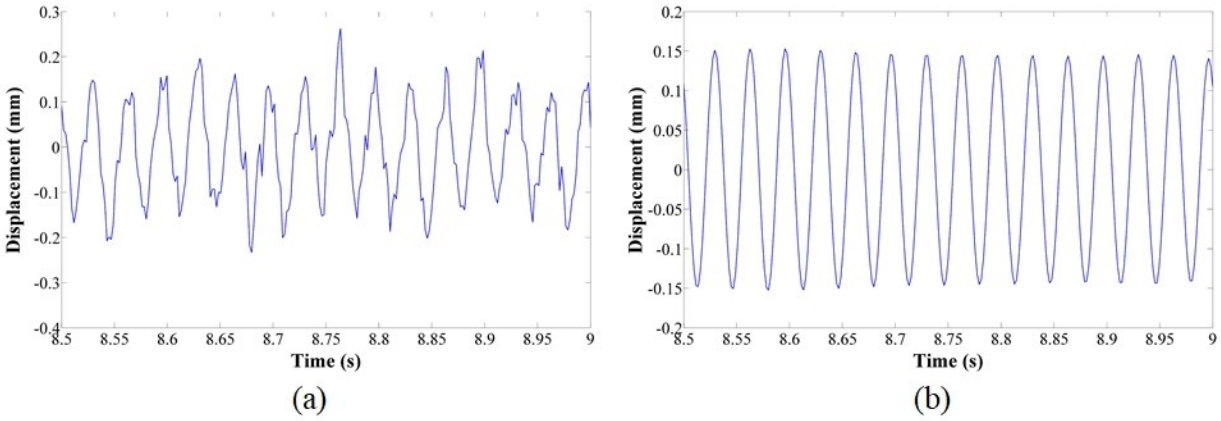

Figure 4.5: Time response comparison at 30 Hz excitation frequency: (a) raw; (b) post-processed

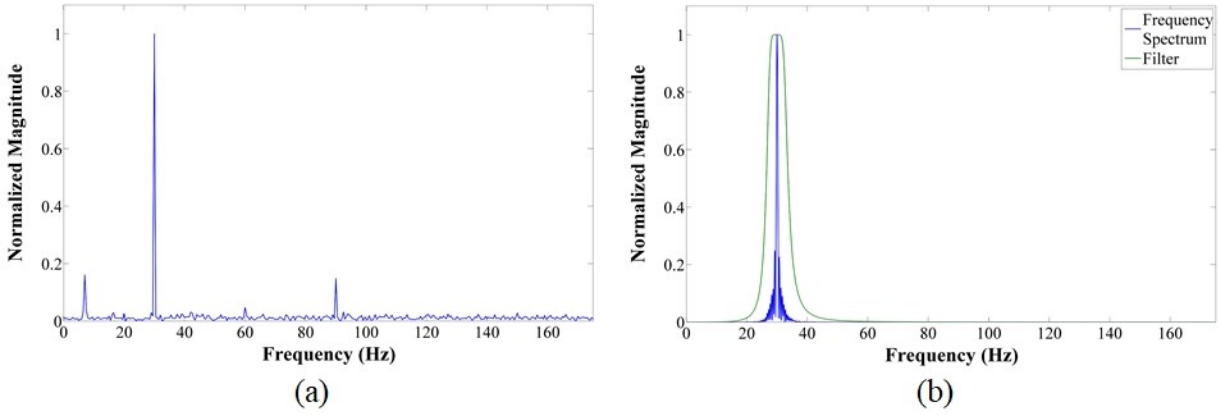

Figure 4.6: Frequency spectrum comparison at 30 Hz excitation frequency: (a) raw; (b) post-processed

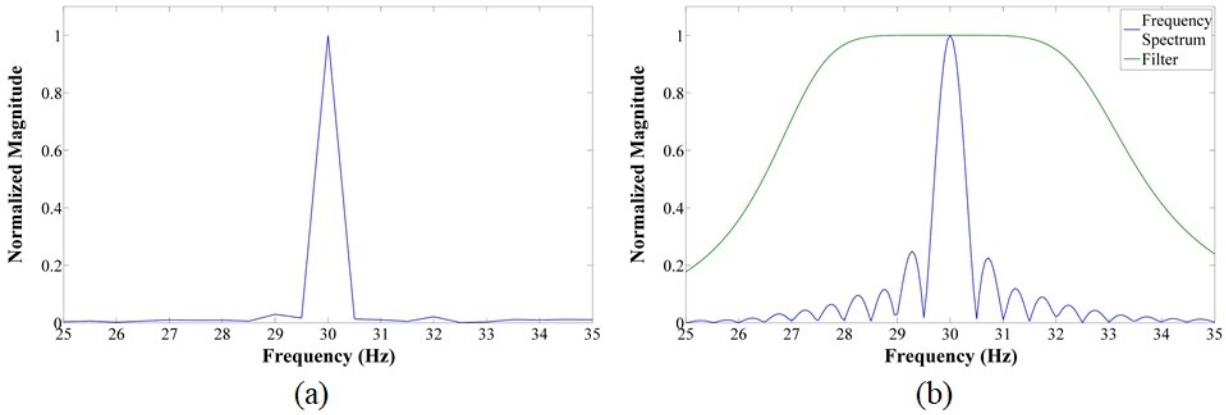

Figure 4.7: Detailed view of frequency spectrum comparison at 30 Hz excitation frequency: (a) raw; (b) post-processed

4.1.3. Original Experimental Apparatus

Subjecting a structure to forced harmonic excitation and measuring its dynamic behaviors requires the minimization of unwanted contamination. For example, when using a shaker to apply a dynamic load to a beam, the dynamic behaviours of the shaker must have a minimal impact on the specimen under test. When the shaker directly excites the specimen under test, additional stiffness is introduced, which affects the dynamics of the structure. If the impact of the dynamic behaviours of the shaker are not minimized, unwanted contamination is introduced

in the measured response of the structure, which gives results which do not represent the dynamics of the actual specimen under test.

The original experimental apparatus is built to reduce the fundamental frequency of the shaker system. The original experimental apparatus is shown in Figure 4.8. The specimen is held in a base fixture which is fixed to the ground, such that the specimen is mounted in a fixed-free, or cantilevered, configuration. Through a stinger, the shaker applies a force at a location of 20% of the length of the specimen from the base fixture. Eye bolts are mounted to a steel frame, which provide mounting locations for aircraft cable used to suspend the shaker. Suspending the shaker is recommended when the structure under test is fixed [94]. In this configuration, the shaker system is similar to a pendulum, whose fundamental frequency is inversely proportional to the suspension length. Thus, the vertical distance between the shaker and the aircraft cable mount locations is selected to be as large as possible, to achieve a relatively low fundamental frequency. Of course, the height of the frame constrains the suspension cable length.

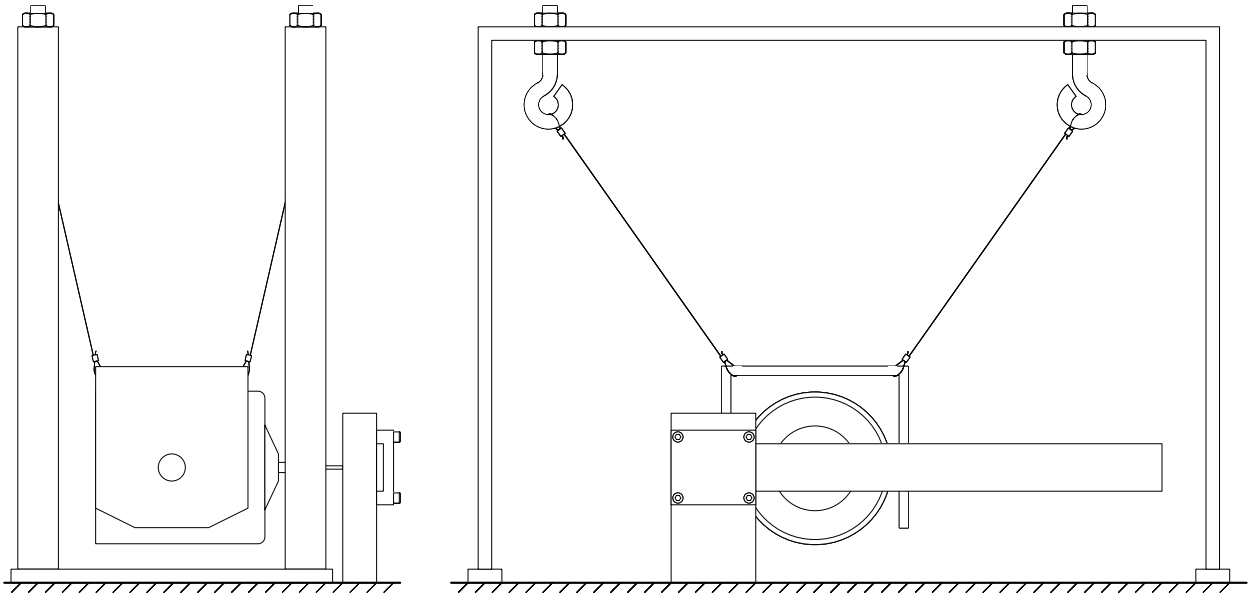

Figure 4.8: Original experimental apparatus for forced vibration (not drawn to scale)

Benchmarking of the original experimental apparatus showed poor performance when compared with the Euler-Bernoulli beam theory. The first natural frequency of the benchmark beam is found to be 5.75 Hz, which compares well with the analytical result of 5.62 Hz. The second natural frequency of the benchmark beam is found as 60.25 Hz compared with the

analytical result of 35.21 Hz, which is an unacceptable representation of the beam. Mayes and Gomez provide several recommendations to reduce the impact of the shaker and stinger on the structure, such as adjusting the stinger length, and choosing different excitation locations [94]. However, these adjustments show an insignificant change in the second natural frequency of the benchmark beam. Mohammadali and Ahmadian suggest that the shaker-stinger interaction with the beam can significantly impact its response, especially for flexible and lightweight structures [95], which is an appropriate description of the benchmark beam, and the category A and B SLJ specimens. Thus, the original experimental apparatus is revised to improve accuracy.

4.1.4. Revised Experimental Apparatus

It is apparent from benchmarking the original experimental apparatus that using the shaker and stinger to directly excite the specimen under test gives poor results. Thus, the excitation system of the revised experimental apparatus imparts harmonic base excitation to the specimen under test. In this configuration, the specimen under test is in a fixed-free configuration, but the fixed support is free to move along the transverse direction relative to the structure under test. Applying a harmonic base excitation to the specimen under test eliminates the additional stiffness acting on the specimen from the shaker and stinger. Measurements then become a more accurate representation of the specimen's dynamic behaviors.

The revised experimental apparatus is shown in Figure 4.9. The main components used in this apparatus include the shaker, shaking table, fixed support, optical position sensor, and the cooling vacuum. The shaking table is mounted to linear bearings, which allows the base to move along the transverse direction. The shaker is fixed to the ground to prevent it from moving during operations. The shaking table and shaker are connected through the stinger, which is threaded into a mount on the shaking table. The fixed support is mounted to the shaking table, and the specimen under test is inserted into the fixed support, giving fixed-free boundary conditions. In this configuration, the shaker excites the specimen under test through the shaking table and fixed support, resulting in harmonic base excitation. Since the base is free to oscillate, we must measure its displacement as well as the displacement of the specimen under test, which requires two optical position sensors. The cooling vacuum is used to ensure the shaker does not overheat, since the shaker typically runs for more than 2 hours during data collection per specimen.

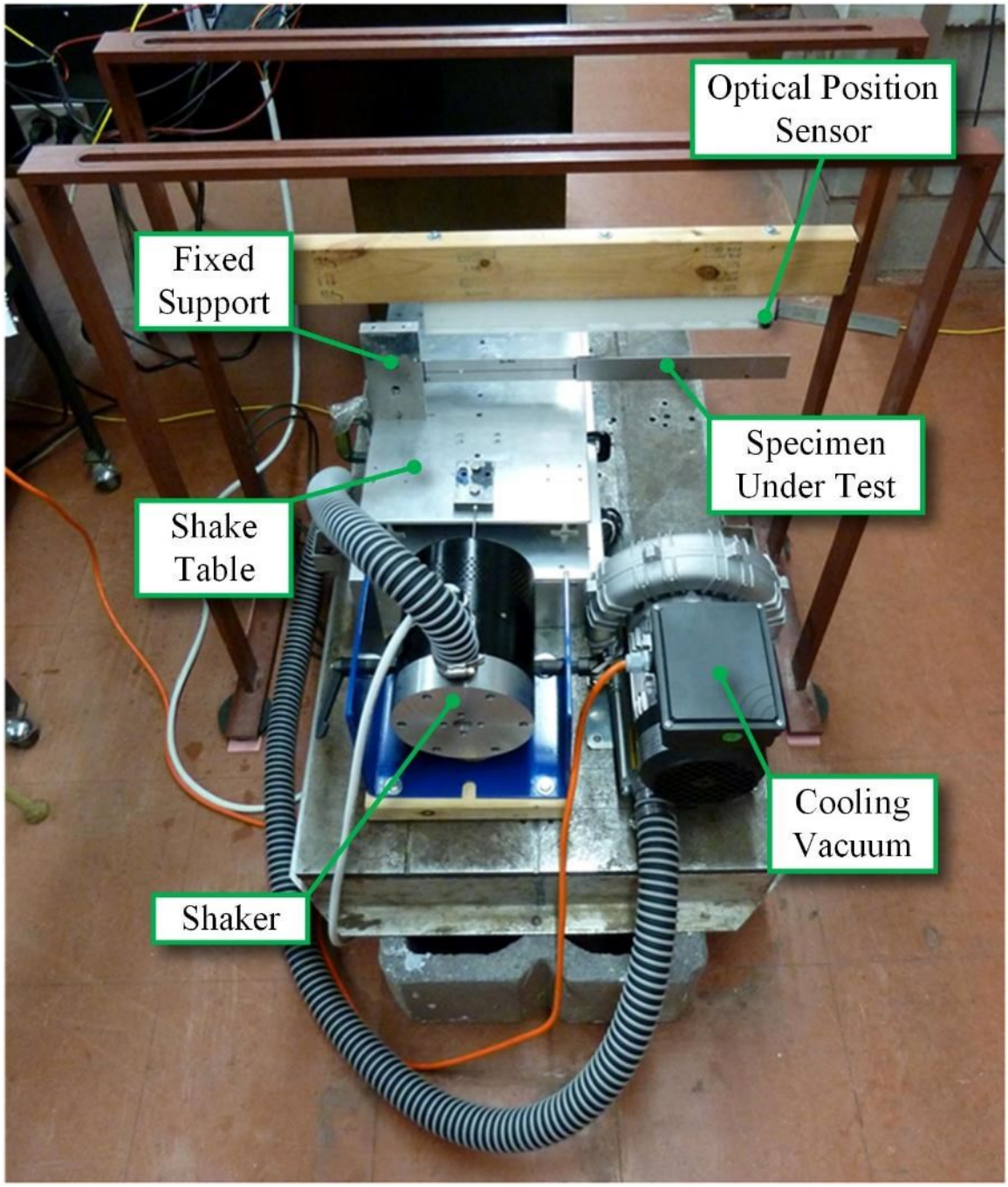

Figure 4.9: Revised experimental apparatus for harmonic base excitation

The natural frequency benchmarking results for the revised experimental apparatus show a significant improvement over the results from the original apparatus. The resulting analytical and experimental natural frequencies of the first three vibration modes are displayed in Table

4.2, including the measurement error percentage. From these benchmarking results, it can be seen that the measured natural frequencies from the revised experimental apparatus are in close agreement with those based on the Euler-Bernoulli beam theory. The largest reported error of 2.31% is found in the first vibration mode, whereas the remaining vibration modes report less than 1% error. The amount of error reported in the first vibration mode is likely due to the frequency resolution used in the data collection frequency sweep. This means that the measured natural frequency has a tolerance of plus or minus 0.125 Hz. Thus, a measured natural frequency of 5.75 Hz means that the actual result could range from 5.625 Hz to 5.875 Hz. It is also worth mentioning that the frequency resolution affects the magnitude of the measured error to a greater extent in the low frequency range than in the higher frequency range, due to the relative magnitude of the frequency resolution compared to the lower frequency range. This confirms that the revised experimental apparatus can reliably measure the resonant frequencies of the structure under test within the frequency range considered.

Table 4.2: Revised experimental apparatus natural frequency benchmarking

Vibration Mode	Analytical Natural Frequency (Hz)	Experimental Natural Frequency (Hz)	Measurement Error Percentage (%)
1	5.62	5.75	2.31
2	35.21	35.50	0.82
3	98.58	99.25	0.68

The measured mode shapes of the benchmark beam are compared with those based on the Euler-Bernoulli beam theory. Figure 4.10 shows the comparison between the analytical and measured mode shapes for the first three vibration modes, respectively. The experimentally measured mode shapes are in close agreement with the analytical results for all three vibration modes. Of these measured mode shapes, the second vibration mode compares most favourably. These results further validate the performance of the revised experimental apparatus, which can be used with confidence for the remainder of the analyses when required.

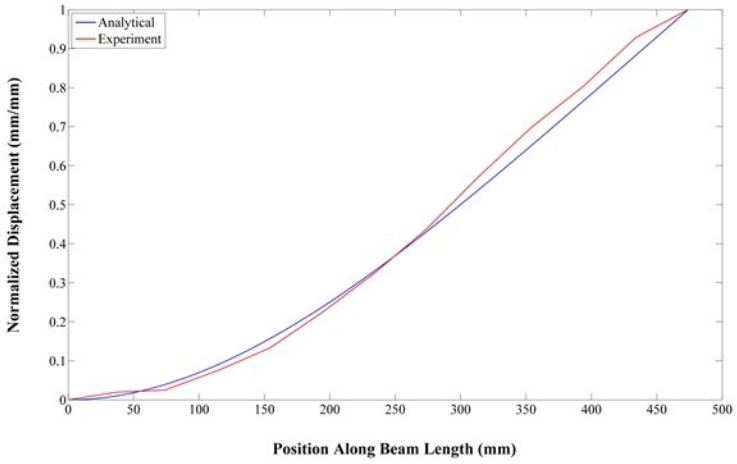

(a)

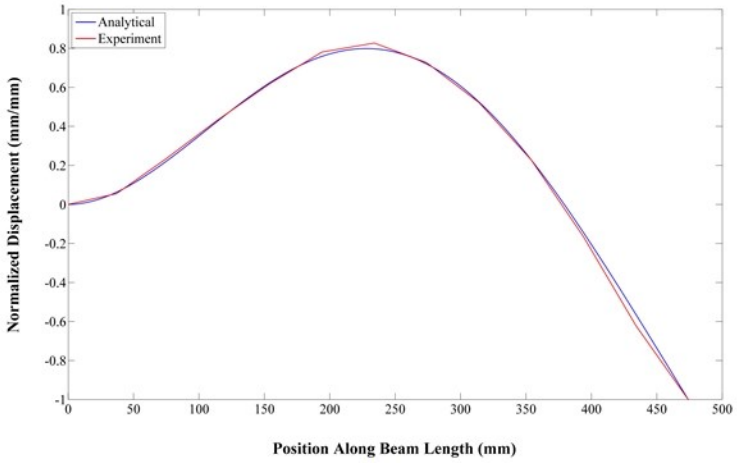

(b)

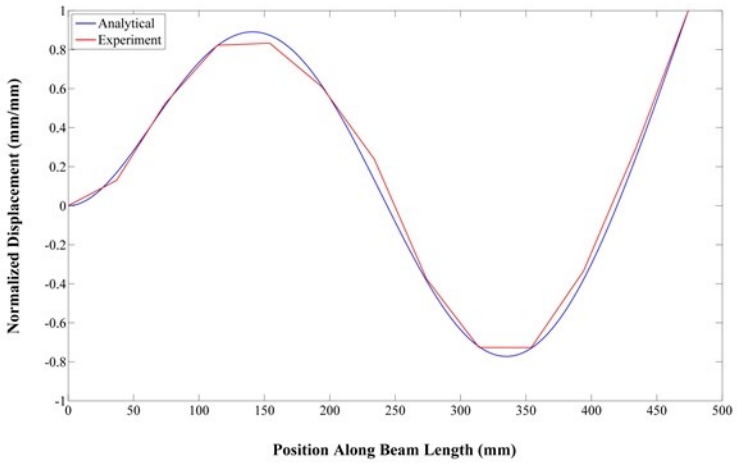

(c)

Figure 4.10: Benchmark beam mode shapes: (a) mode 1; (b) mode 2; (c) mode 3

4.2. Experimental Validation of Simulation Results

In this section, the results obtained using the numerical analysis approaches from Chapter 3 are compared with the experimental ones. The measured natural frequencies and mode shapes of category A and B specimens are presented. The effective Young's modulus of the single variable TMM model updating approach is updated using the measured natural frequencies of beam 2A as model updating targets. The experimental damping ratios are presented, and used in the FE model to investigate Rayleigh damping tuning. Further, the experimental and FE transmissibility functions are presented and discussed.

4.2.1. Evaluation of Dynamic Behaviours of Category A Specimens

The natural frequencies measured experimentally for the category A specimens are shown in Table 4.3. It can be seen that the natural frequencies tend to increase with increasing overlap length. This is in agreement with the numerical analysis findings in Section 3.4.2 from Chapter 3. This validates the relationship between the beam overlap region length and the natural frequencies for category A specimens.

Table 4.3: Natural frequencies measured by the experiment for the category A specimens

Beam Specimens	Overlap Length (mm)	Natural Frequencies (Hz)		
		f_1	f_2	f_3
1A	30	7.00	42.00	123.00
2A	40	7.25	43.25	128.25
3A	50	7.50	44.25	133.00
4A	60	8.00	46.25	138.50

To determine the effective Young's modulus from the single variable TMM model updating approach, model updating is performed for beam 2A, using the measured natural frequencies as model updating targets. However, the first two measured natural frequencies of beam 2A are used for model updating, since only three natural frequencies are measured experimentally. In this way, the single variable TMM model updating approach results for the third natural frequency can be evaluated, to determine its ability to find the natural frequencies of higher modes of vibration which are not used in model updating. Through model updating, the effective Young's modulus is found to be 2.375 GPa. Of course, the effective density is

unchanged from Section 3.4.2, however, the effective Young's modulus is slightly lower than the effective Young's modulus from Section 3.4.2 of 3.75 GPa. The updated natural frequencies from the single variable TMM model updating approach are shown in Table 4.4. Like the experimentally measured natural frequencies, the natural frequencies determined by the single variable TMM model updating approach increase with increasing overlap length.

Table 4.4: Natural frequencies determined by single variable TMM model updating for the category A specimens

Beam Specimens	Overlap Length (mm)	Natural Frequencies (Hz)		
		f_1	f_2	f_3
1A	30	7.25	42.18	127.49
2A	40	7.51	42.66	131.86
3A	50	7.78	43.22	136.30
4A	60	8.06	43.88	140.74

The relative natural frequency error between the experiment and the FE model, the single variable TMM model updating approach, and the additive TMM approach are shown in Table 4.5 to Table 4.7, respectively. Both the FE model and the single variable TMM model updating approach compare well with the measured natural frequencies. The additive TMM approach, however, compares poorly with the measured natural frequencies. For all the category A specimens, the relative errors found by the additive TMM approach are greater than 5% in absolute value for each natural frequency, giving a maximum absolute relative error of 14.294% for the second natural frequency of beam 4A. The additive TMM approach is consistently outperformed by the FE model and the single variable TMM model updating approach for category A specimens. These results demonstrate the improved performance given by the effective Young's modulus determined by the single variable TMM model updating approach compared to the additive TMM approach. Comparing the FE model and the single variable TMM model updating approach shows that the latter outperforms the former for all computed natural frequencies, apart from the second natural frequency of beam 4A. This is particularly notable for the third natural frequency of each specimen, which was not used as a model updating target in the determination of the effective Young's modulus of the single variable TMM model updating approach. This shows that this approach performs well under uncertainty

for the category A specimens. The maximum absolute relative error of the FE model and the single variable TMM model updating approach are 5.459% and 5.114%, respectively, both considerably lower than the additive TMM approach.

Table 4.5: Relative errors of the FE model for category A specimens

Beam Specimens	Overlap Length (mm)	Relative Error (%)		
		f_1	f_2	f_3
1A	30	-4.241	-2.250	-3.683
2A	40	-4.804	-2.543	-3.233
3A	50	-5.459	-3.420	-3.296
4A	60	-3.007	-2.406	-2.915

Table 4.6: Relative errors of the single variable TMM model updating for the category A specimens

Beam Specimens	Overlap Length (mm)	Relative Error (%)		
		f_1	f_2	f_3
1A	30	-3.623	-0.434	-3.648
2A	40	-3.561	1.365	-2.814
3A	50	-3.685	2.321	-2.479
4A	60	-0.737	5.114	-1.614

Table 4.7: Relative errors of the additive TMM for the category A specimens

Beam Specimens	Overlap Length (mm)	Relative Error (%)		
		f_1	f_2	f_3
1A	30	-6.011	-8.663	-5.077
2A	40	-6.816	-10.277	-5.028
3A	50	-7.865	-13.190	-5.710
4A	60	-5.755	-14.294	-6.127

The measured and simulated mode shapes of beams 1A and 4A are shown in Figure 4.11 and Figure 4.12, respectively. Of course, the measured mode shape resolutions are significantly lower than the numerical analysis approaches, however, they adequately describe the specimen mode shapes. All of the numerical analysis approaches are in good agreement with the

experimentally measured mode shapes for category A specimens. Overall, the FE model and the single variable TMM model updating approach compare slightly better with the experimental results of beams 1A and 4A than the additive TMM. However, the additive TMM approach compares better with the second measured mode shape of beam 4A. The measured mode shape shows a decreased change in slope near the overlap region, like the relatively stiffer overlap region of the additive TMM approach.

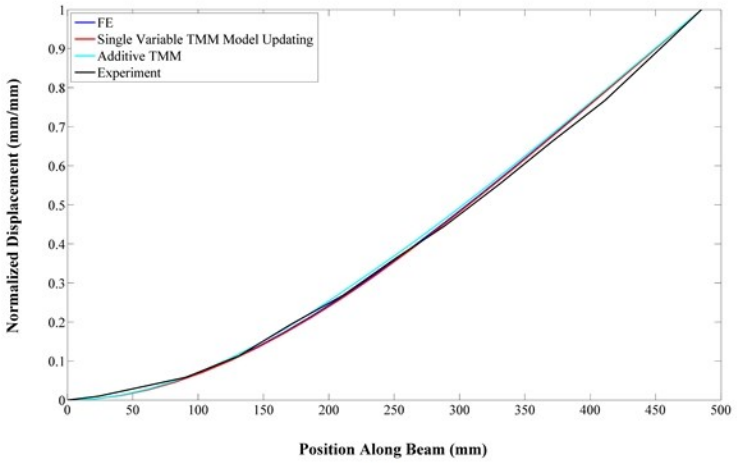

(a)

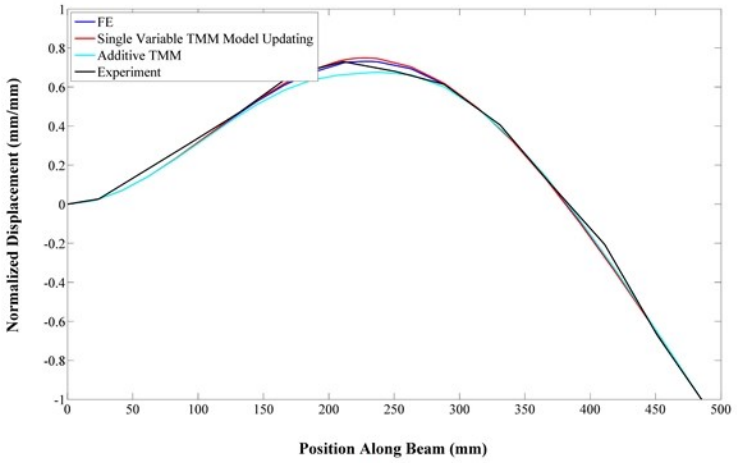

(b)

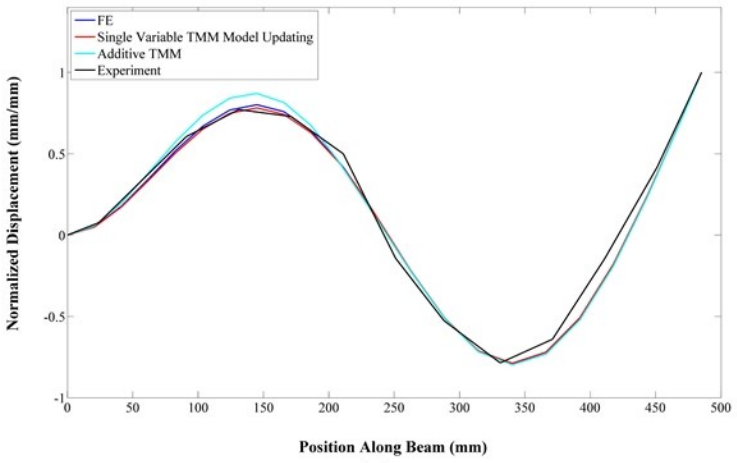

(c)

Figure 4.11: Beam 1A updated mode shapes: (a) mode 1; (b) mode 2; (c) mode 3

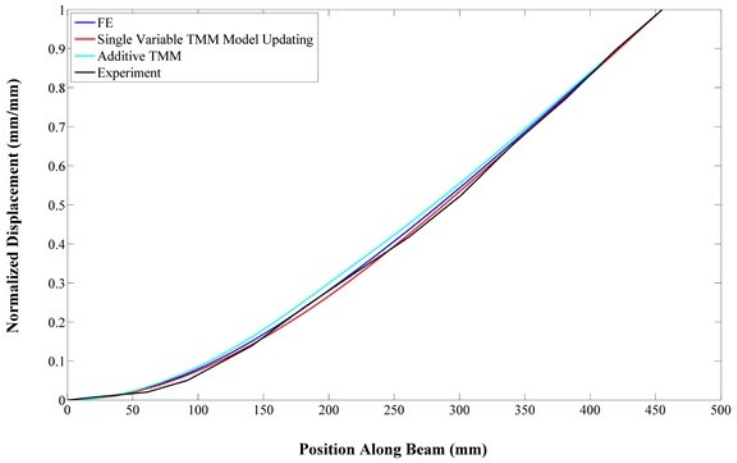

(a)

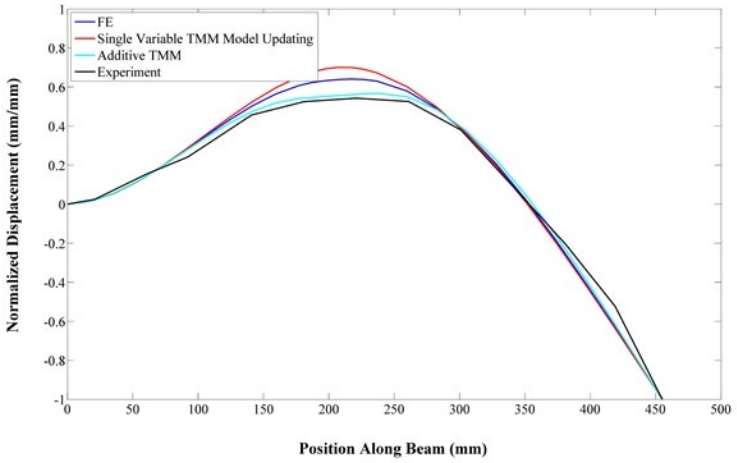

(b)

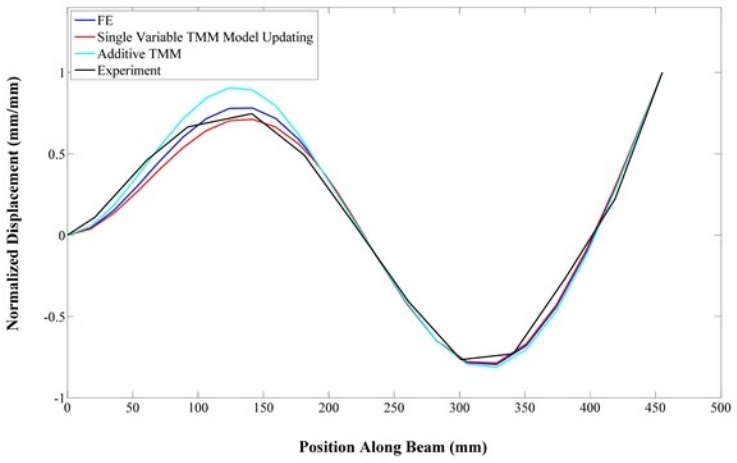

(c)

Figure 4.12: Beam 4A updated mode shapes: (a) mode 1; (b) mode 2; (c) mode 3

4.2.2. Evaluation of Dynamic Behaviours of Category B Specimens

The natural frequencies measured by the experiment for the category B specimens are shown in Table 4.8. Like Section 4.2.1, the natural frequencies tend to increase with increasing overlap length. This is in agreement with the numerical analysis findings in Section3.4.3 from Chapter 3. This validates the relationship between the beam overlap region length and the natural frequencies for category B specimens.

Table 4.8: Natural frequencies measured by the experiment for the category B specimens

Beam Specimens	Overlap Length (mm)	Natural Frequencies (Hz)		
		f_1	f_2	f_3
1B	30	5.25	31.00	91.25
2B	40	5.25	32.00	94.50
3B	50	5.75	33.25	99.00
4B	60	6.00	34.75	103.75

Table 4.9 show the resulting natural frequencies of the TMM for the category B specimens. The effective Young's modulus determined by the single variable TMM model updating approach for beam 2A in section 4.2.1 (2.375 GPa) is used for the category B specimens to investigate their general use. Like the experimentally measured natural frequencies, the natural frequencies increase with increasing overlap length.

Table 4.9: Natural frequencies determined by single variable TMM model updating for the category B specimens

Beam Specimens	Overlap Length (mm)	Natural Frequencies (Hz)		
		f_1	f_2	f_3
1B	30	5.28	30.70	92.73
2B	40	5.46	31.05	95.91
3B	50	5.66	31.47	99.15
4B	60	5.86	31.96	102.38

The relative natural frequency error between the experiment and the numerical analysis approaches are listed in Table 4.10 to Table 4.12, for the category B specimens. Like Section 4.2.1, the additive TMM approach compares least favourably with the measured natural

frequencies. It is worth noting, however, that the performance of the additive TMM approach for the category B specimens is significantly improved compared to the category A specimens. The maximum absolute relative error in this case is 10.601%, a significant reduction compared to 14.249% for the category A specimens. The FE model and the TMM using the effective Young's modulus determined by the single variable TMM model updating approach for beam 2A are in good agreement with the measured natural frequencies for the category B specimens. From the individual relative errors, it is difficult to determine whether the FE model or the TMM using the effective Young's modulus from beam 2A compare better with the experiment. However, comparing the maximum absolute relative errors from each shows that the former tends to compare more favourably, at 5.484%, than the latter which gives 8.035%. Further, the maximum absolute relative error for the category B specimens, determined by the TMM using the effective Young's modulus of beam 2A, is greater than the category A specimens, determined by the single variable TMM model updating approach, giving 5.114%. Interestingly, in both cases, the maximum relative error is found in the second natural frequency of the fourth specimen, corresponding to an overlap length of 60 mm. Apart from beam 4B, the third natural frequencies of the category B specimens found by the TMM compare better with the experimental results than the FE model. This is interesting again since the third natural frequency was not used when model updating was performed for beam 2A. The presence of an adherend to adhesive thickness ratio for the overlap region is confirmed in this case, since the effective Young's modulus determined by the single variable TMM model updating approach for beam 2A perform well for category B specimens in the TMM.

Table 4.10: Relative errors of the FE model for the category B specimens

Beam Specimens	Overlap Length (mm)	Relative Error (%)		
		f_1	f_2	f_3
1B	30	-1.418	-1.846	-1.968
2B	40	-5.484	-1.532	-2.184
3B	50	-0.339	-0.935	-1.258
4B	60	-0.177	-0.207	-0.323

Table 4.11: Relative error of the single variable TMM model updating for the category B specimens

Beam Specimens	Overlap Length (mm)	Relative Error (%)		
		f_1	f_2	f_3
1B	30	-0.506	0.980	-1.619
2B	40	-4.041	2.965	-1.494
3B	50	1.604	5.358	-0.148
4B	60	2.269	8.035	1.318

Table 4.12: Relative error of the additive TMM for the category B specimens

Beam Specimens	Overlap Length (mm)	Relative Error (%)		
		f_1	f_2	f_3
1B	30	-2.795	-7.049	-3.006
2B	40	-7.272	-8.372	-3.660
3B	50	-2.315	-9.525	-3.278
4B	60	-2.541	-10.601	-3.028

The measured and simulated mode shapes of beams 1B and 4B are shown in Figure 4.13 and Figure 4.14, respectively. All of the numerical analysis approaches are in good agreement with the experimentally measured mode shapes for all of the category B specimens. For beam 1B, the performance of each numerical technique is mixed, therefore, it is difficult to say for certain which performs best. However, for beam 4B it can be seen that the FE model tends to compare favourably with the measure mode shapes, while the TMM using the effective Young's modulus determined by the single variable TMM model updating approach for beam 2A is a close second. The second mode shape of the additive TMM approach does not compare as well with the experiment for beam 4B, unlike beam 4A from Section 4.2.1.

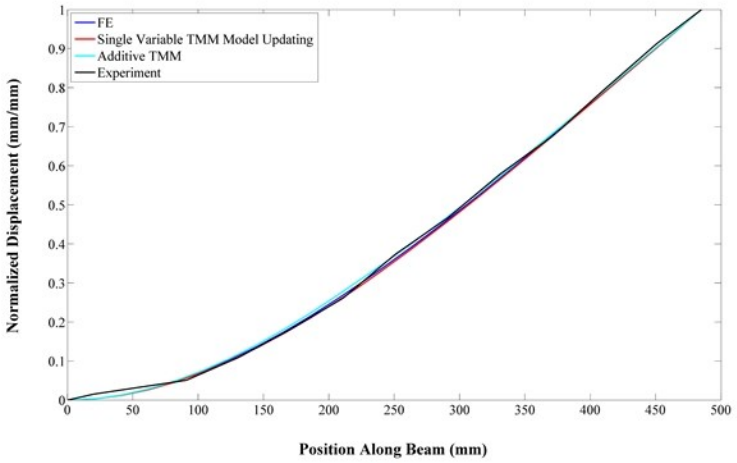

(a)

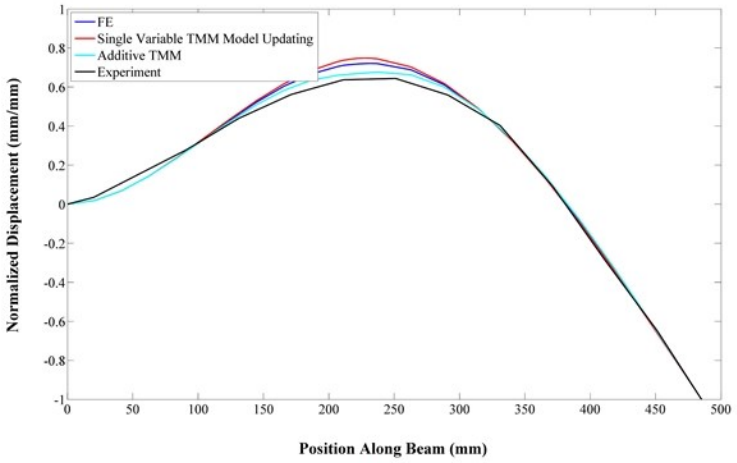

(b)

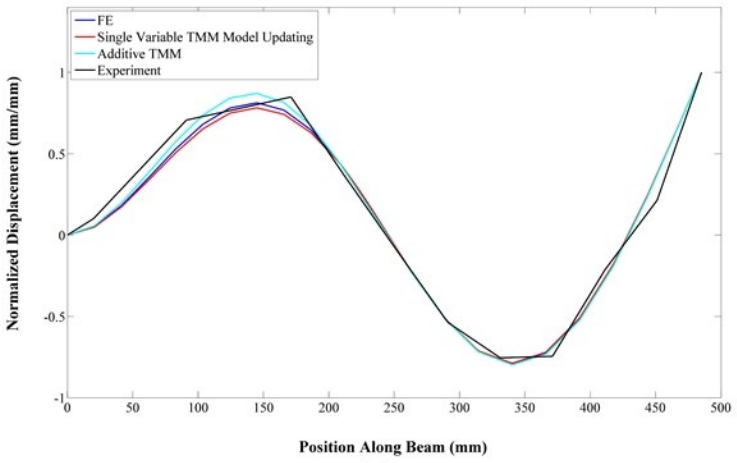

(c)

Figure 4.13: Beam 1B updated mode shapes: (a) mode 1; (b) mode 2; (c) mode 3

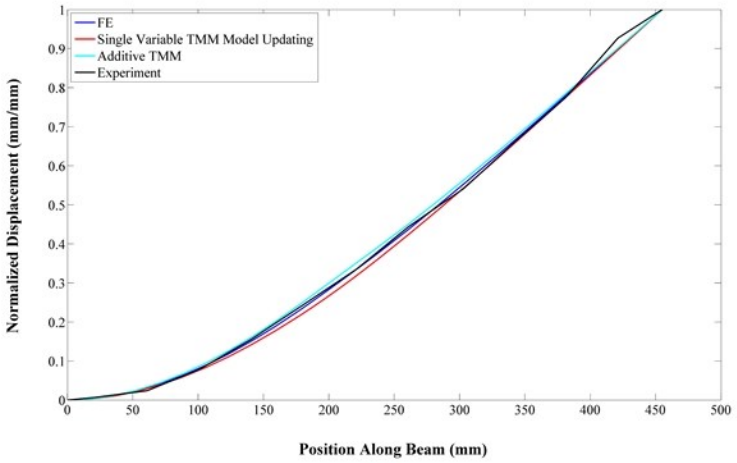

(a)

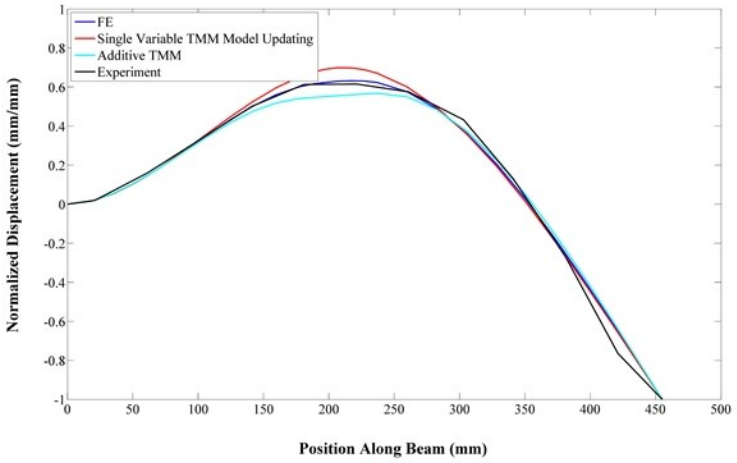

(b)

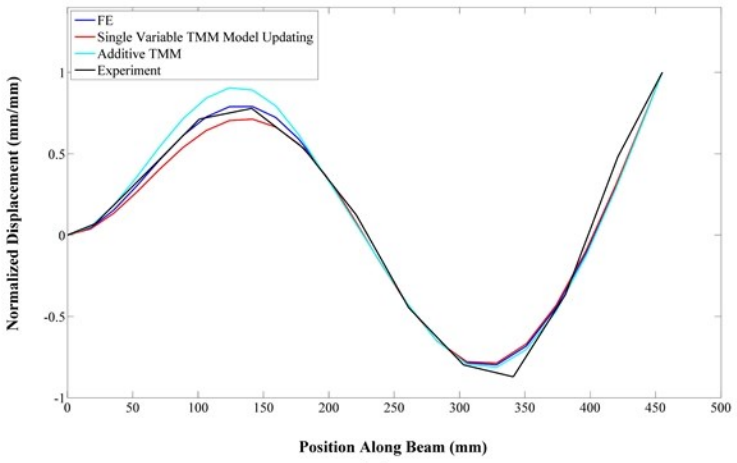

(c)

Figure 4.14: Beam 4B updated mode shapes: (a) mode 1; (b) mode 2; (c) mode 3

4.2.3. Specimen Damping Ratios

The measured damping ratios of the category A and B specimens are shown in Table 4.13 and Table 4.14, respectively. Apart from the second and third damping ratios of beam 3A, the damping ratios for the category A specimens tend to decrease with increasing overlap length. The first damping ratio of the category B specimens shows a similar relationship as the category A specimens. Finally, the damping ratios of each specimen decrease with an increase in vibration mode. This is expected from (4.5) of the quadrature peak picking method, which shows that an increase in resonant frequency tends to decrease the damping ratio. For this reason, it is interesting that the damping ratios of the category B specimens do not show a clear decrease with increasing overlap length. From Sections 4.2.1 and 4.2.2, it was seen that increasing the overlap length caused an increase in the specimen's natural frequency. Thus, one would expect the category B specimens to follow a similar trend as the category A specimens. An explanation for this might be related to the experimental driving frequency resolution used near resonant frequencies. Using a finer driving frequency resolution may give higher magnitude resonant frequency TRs, which would impact the 3-dB down point, and therefore, the specimen damping ratios. However, this needs to be investigated further in future work.

Table 4.13: Damping ratios of category A specimens

Beam Specimens	Damping Ratios		
	ζ_1	ζ_2	ζ_3
1A	1.439×10^{-2}	4.919×10^{-3}	2.515×10^{-3}
2A	1.436×10^{-2}	4.159×10^{-3}	2.112×10^{-3}
3A	1.326×10^{-2}	6.168×10^{-3}	2.808×10^{-3}
4A	1.174×10^{-2}	2.983×10^{-3}	9.301×10^{-4}

Table 4.14: Damping ratios of category B specimens

Beam Specimens	Damping Ratios		
	ζ_1	ζ_2	ζ_3
1B	2.381×10^{-2}	5.103×10^{-3}	2.795×10^{-3}
2B	2.421×10^{-2}	4.193×10^{-3}	2.342×10^{-3}
3B	2.113×10^{-2}	4.469×10^{-3}	3.380×10^{-3}
4B	2.056×10^{-2}	6.421×10^{-3}	2.709×10^{-3}

4.2.4. Rayleigh Damping Tuning

Tuning the Rayleigh damping model requires two natural frequencies and corresponding damping ratios, as discussed in Section 3.1.2 from Chapter 3. Rayleigh damping has some shortcomings, particularly when used for large frequency ranges. These shortcomings are presented to demonstrate the care needed when tuning the Rayleigh damping model, and to choose which vibration modes are used for the remainder of the FE models in this chapter. The Rayleigh damping model is tuned for all possible vibration mode combinations found experimentally for Beam 1A. Since the experimental analysis gives three natural frequencies for all the dynamic SLJ specimens, over the frequency range considered, there are three possible combinations that can be used for tuning. Plotting the resulting transmissibility functions illustrates the impact of selecting different frequency combinations.

Figure 4.15 shows the FE transmissibility functions for Beam 1A using the following tuning combinations: vibration modes 1 and 2, modes 1 and 3, and modes 2 and 3. The TR magnitudes at the resonant frequencies are noticeably affected by the tuning combination used. To further illustrate this, Figure 4.16 gives a detailed view of each natural frequency. Using a tuning combination of vibration modes 1 and 2 results in overdamping of the third mode, shown by the drastic reduction in magnitude. Similarly, using a tuning combination of vibration modes 2 and 3 shows overdamping in the first mode. Using a tuning combination of vibration modes 1 and 3 results in slight underdamping of the second mode, evidenced by the increase in magnitude. These results demonstrate that the Rayleigh damping model tends to cause overdamping for natural frequencies outside of the frequency range defined by the vibration modes used for tuning, while the opposite is true within this frequency range.

The normalized FE transmissibility function magnitudes for Beam 1A are further compared with the experiment at the resonant frequencies. The overall error between tuning combinations of modes 1 and 2, modes 1 and 3, and modes 2 and 3 are 19.8%, 18.0%, and 12.0% respectively. For Beam 1A, it is apparent that the tuning combination of modes 2 and 3 gives the best overall performance. However, the tuning combination of modes 1 and 2 is selected for the remainder of the FE models, since this combination is best suited for the first two vibration modes of the specimen, which are typically dominant compared to the third mode.

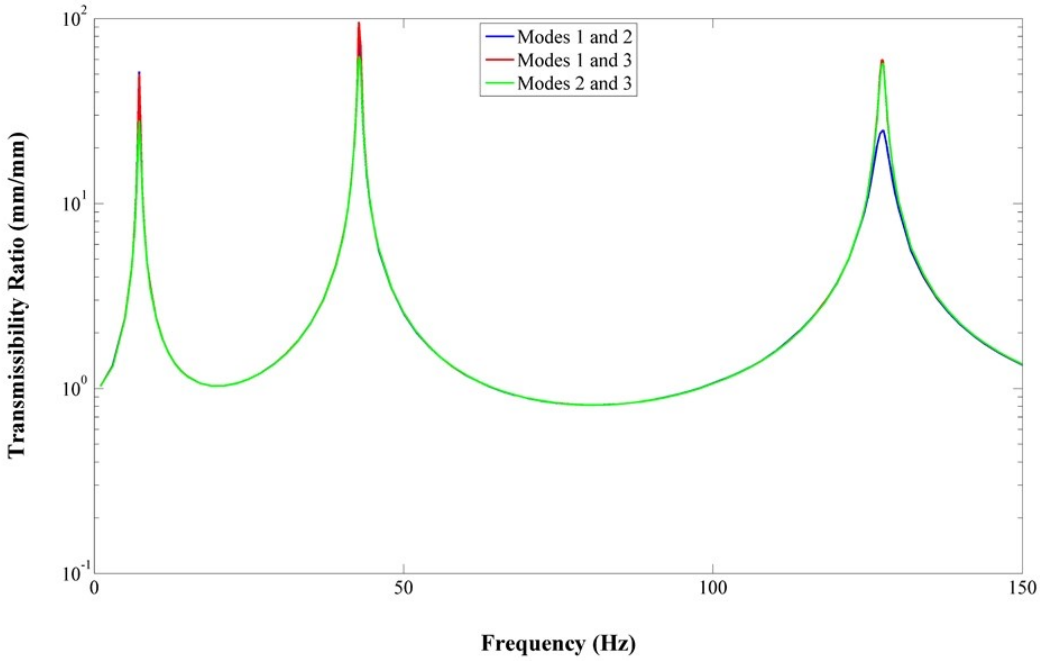

Figure 4.15: FE transmissibility function of Beam 1A damping tuning

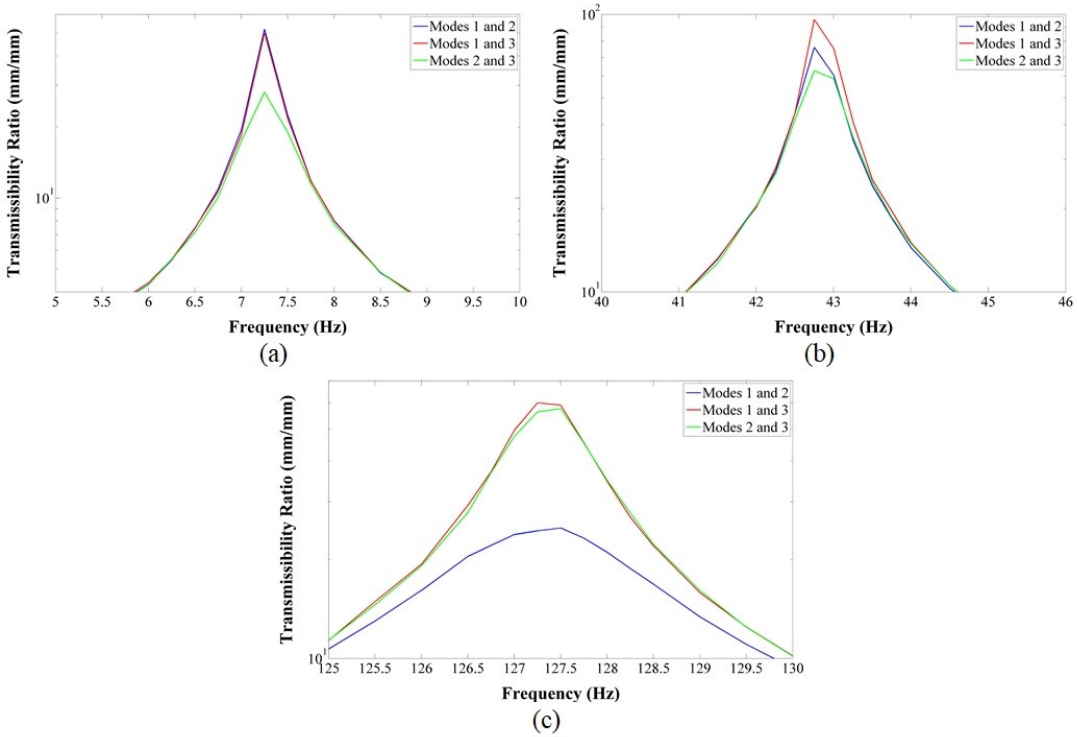

Figure 4.16: Detailed view of the FE transmissibility function of Beam 1A: (a) first mode; (b) second mode; (c) third mode

4.2.5. Specimen Transmissibility Functions

Overall the FE transmissibility functions compare well with the experimental ones. The resulting experimental and FE transmissibility function comparisons are shown in Figure 4.17 to Figure 4.20 for the category A specimens, and Figure 4.21 to Figure 4.24 for the category B specimens. The FE results for the category B specimens show better agreement with the experiment than the category A specimens. This is particularly noticeable in the regions between the natural frequencies. The transmissibility function of Beam 4A in Figure 4.20 shows a noticeable discrepancy compared to the experiment in terms of magnitude. In this case, the measured natural frequency of the third vibration mode had a significantly larger magnitude than the first two natural frequencies. Evidently from Table 4.13, the third damping ratio of beam 4A is significantly smaller than all other specimens. Selecting a different natural frequency combination used to tune the Rayleigh damping model could give improved results.

The effect of damping on the location of the natural frequencies in the FE model can also be observed in their transmissibility functions. All three FE vibration modes from the transmissibility function of Beam 4B show exact matches with experiment; however, the effects of damping in the first two vibration modes cannot be observed with the 0.25 Hz swept frequency resolution used near resonant frequencies. For example, the frequency of the first FE vibration mode from the undamped eigenfrequency analysis is 6.01 Hz (Table 3.15 from Chapter 3), whereas the transmissibility function gives 6 Hz. Thus, a finer swept frequency resolution would be required to see the effects of damping on the first two vibration modes. On the other hand, the third FE vibration mode clearly shows the effects of damping. The undamped eigenfrequency analysis give a frequency value of 104.09 Hz (Table 3.15 from Chapter 3), whereas the transmissibility function gives a frequency of 103.75 Hz, which matches the frequency of the third vibration mode found in the experiment. Taking the swept frequency resolution into account for the third mode of vibration, one would expect the frequency to be 104 Hz for the undamped eigenfrequency case due to the swept frequency resolution. Thus, the damped natural frequency can be observed in the third FE vibration mode within an accuracy of 0.25 Hz from the transmissibility function of Beam 4B.

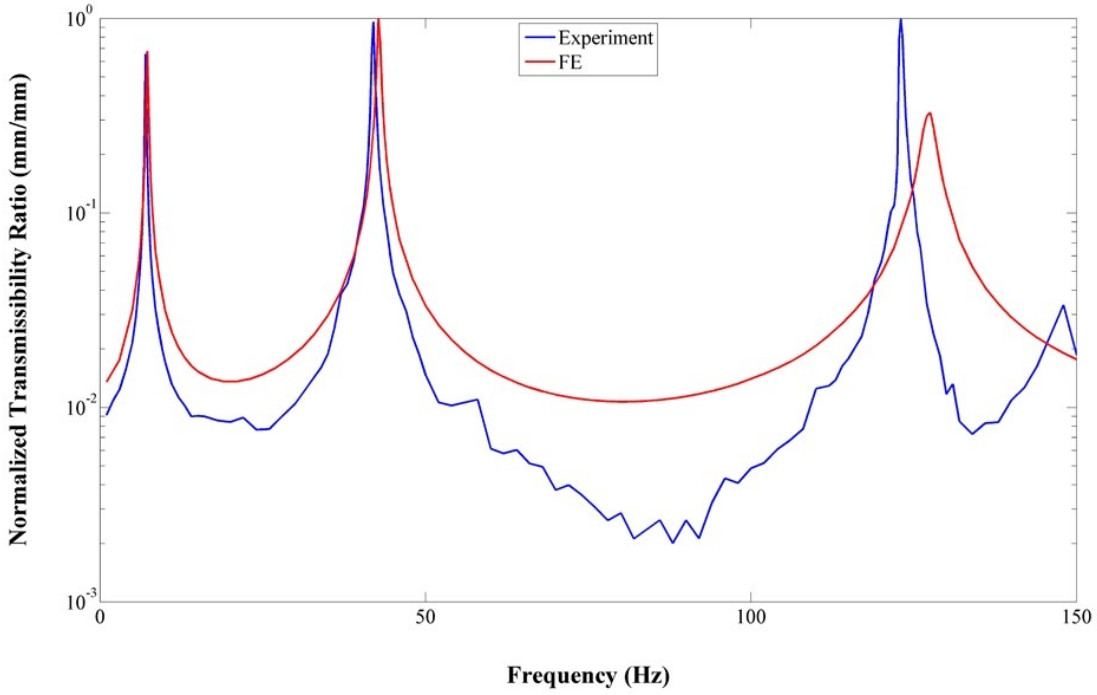

Figure 4.17: Measured and FE simulated transmissibility functions of Beam 1A

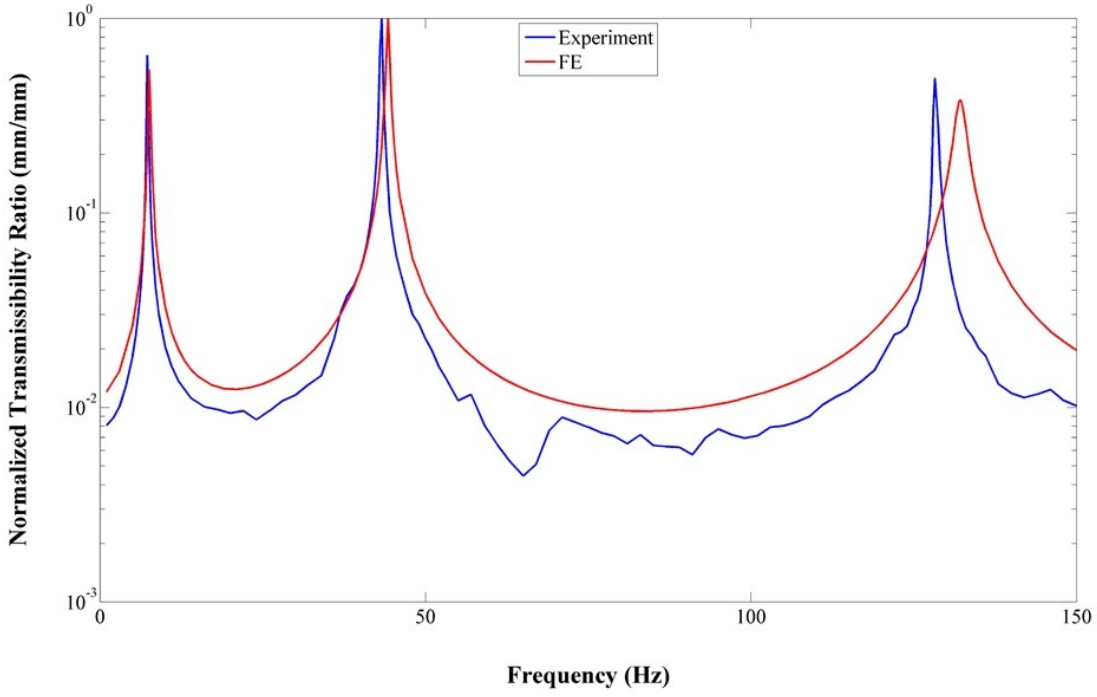

Figure 4.18: Measured and FE simulated transmissibility functions of Beam 2A

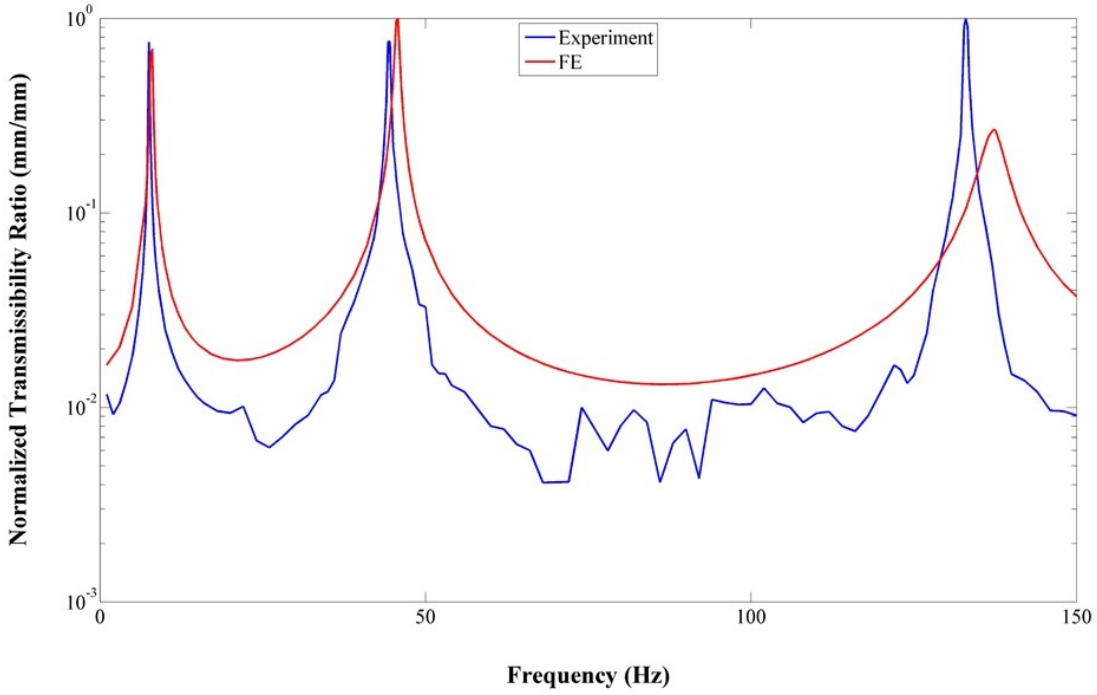

Figure 4.19: Measured and FE simulated transmissibility functions of Beam 3A

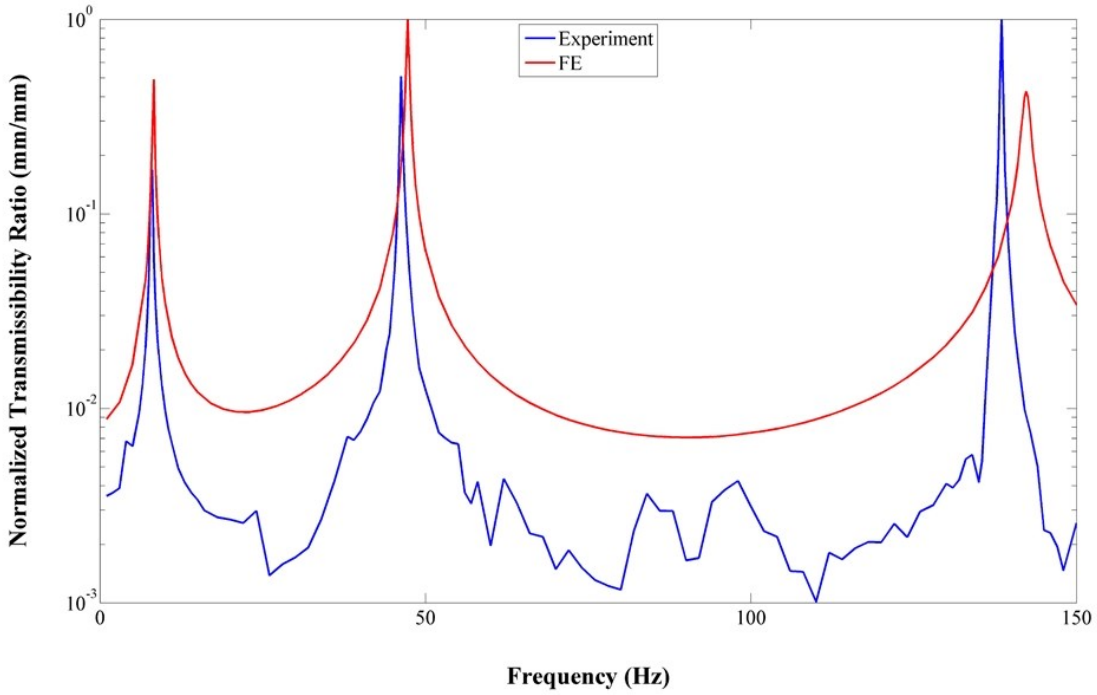

Figure 4.20: Measured and FE simulated transmissibility functions of Beam 4A

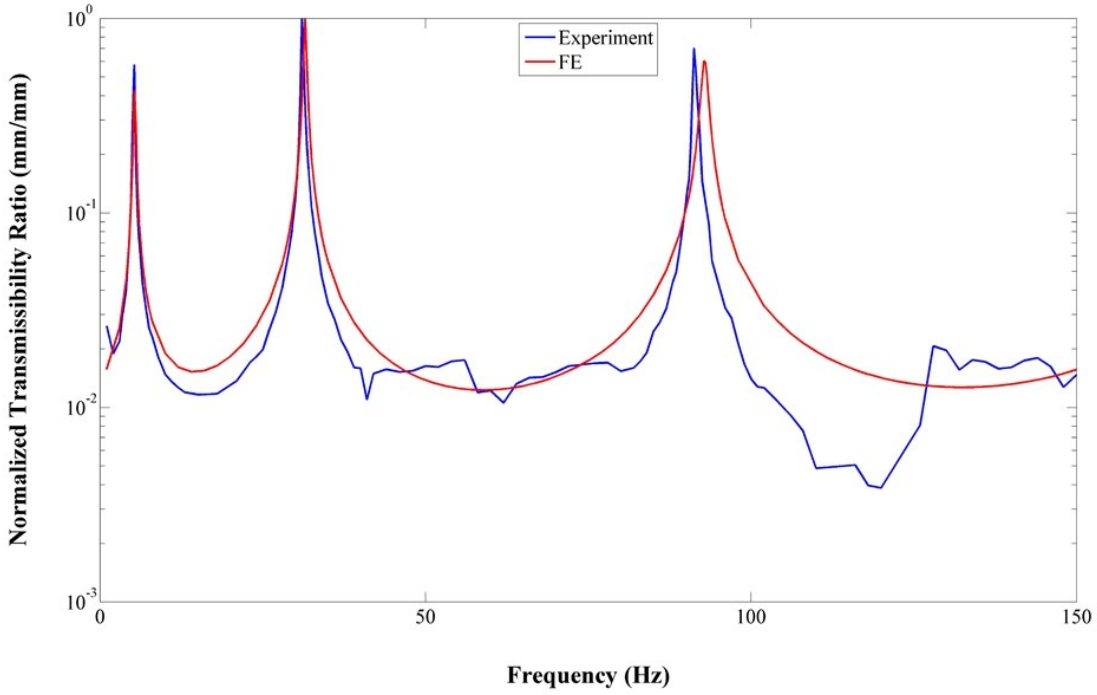

Figure 4.21: Measured and FE simulated transmissibility functions of Beam 1B

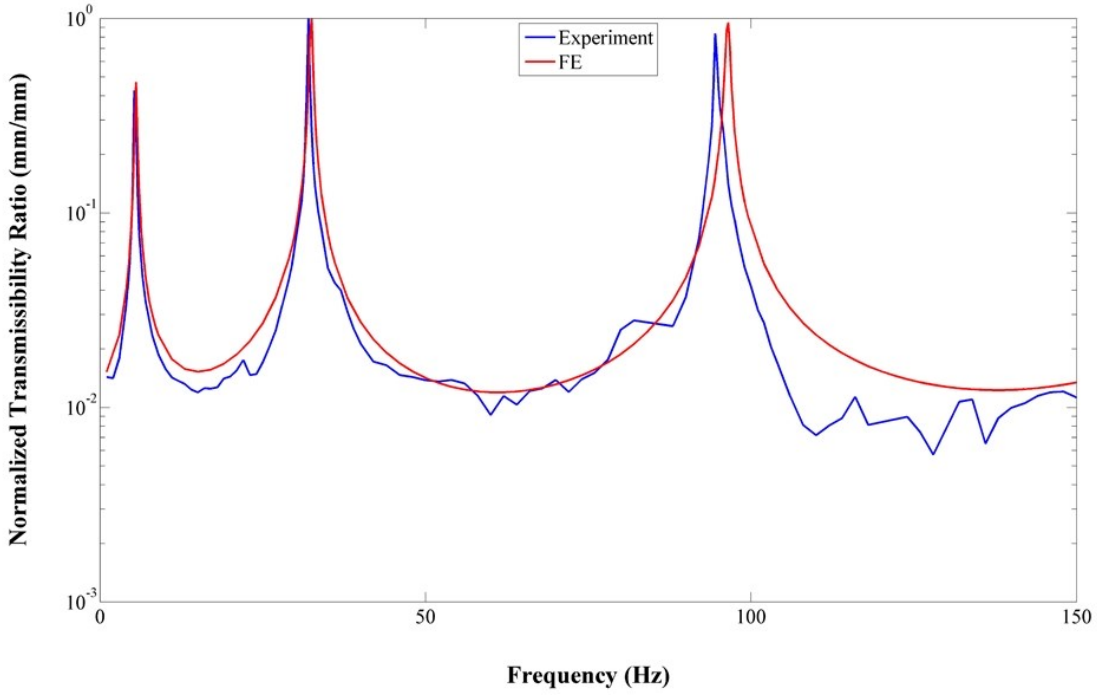

Figure 4.22: Measured and FE simulated transmissibility functions of Beam 2B

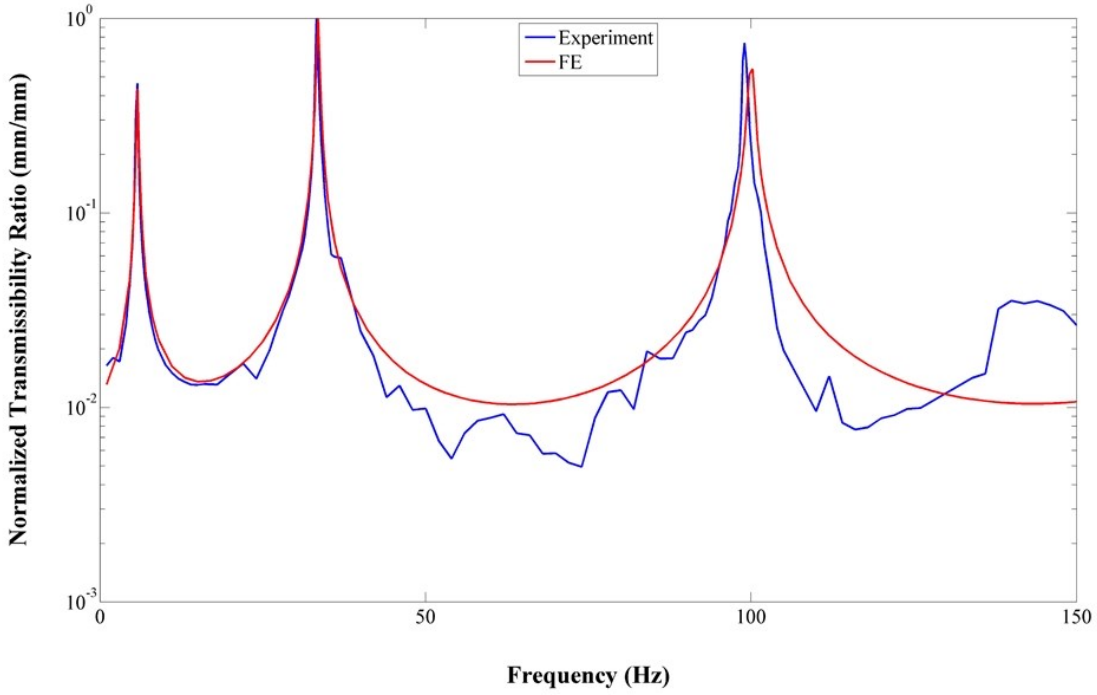

Figure 4.23: Measured and FE simulated transmissibility functions of Beam 3B

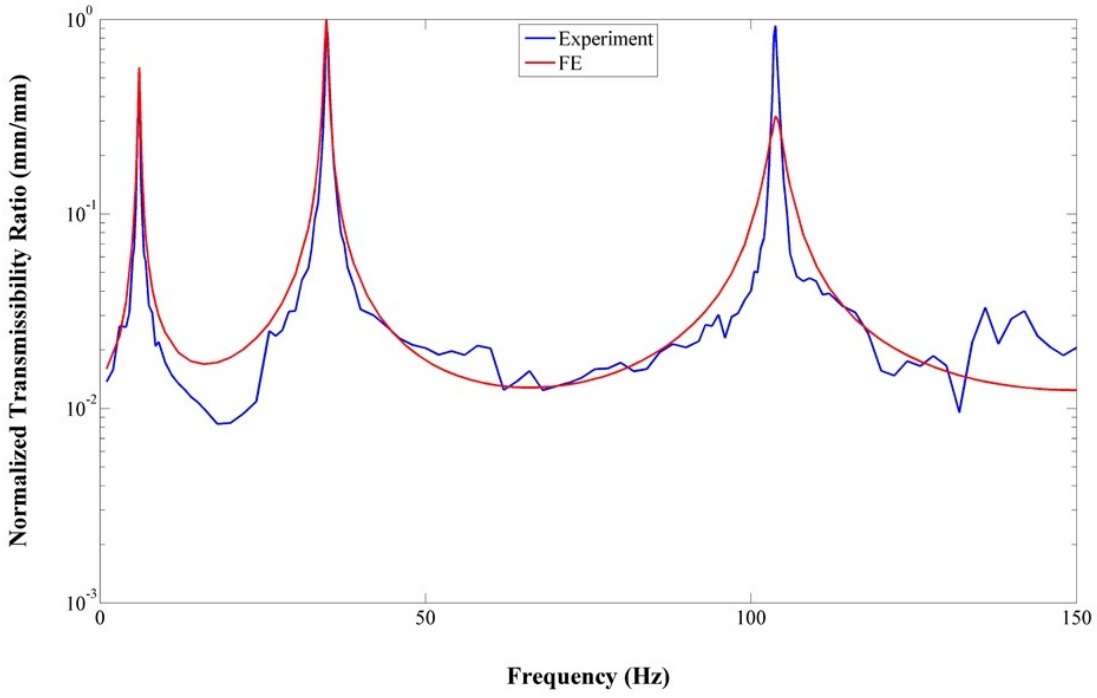

Figure 4.24: Measured and FE simulated transmissibility functions of Beam 4B

4.3. Conclusion

This chapter has evaluated the performance of the numerical analysis techniques experimentally. Further, this chapter has presented the FE and experimental transmissibility functions of the SLJ specimens. The mode shapes of all of the numerical analysis approaches compare well with the measured mode shapes. Both the FE model and the single variable TMM model updating approach natural frequencies show good agreement with the experimental results, with the latter outperforming the former for the category A specimens, and vice-a-versa for the category B specimens. The effective Young's modulus determined by the single variable TMM model updating approach consistently outperforms the effective Young's modulus determined by the additive TMM approach, thereby demonstrating the improvements introduced by model updating. Lastly, the Rayleigh damping tuning has been explored and employed in the FE model. Overall, the transmissibility functions from the FE model compare well with the experiment.

Chapter 5 Performance of a Piezoelectric Energy Harvester

This chapter focuses on the output performance of a PEH. Typically, PEHs provide a power source for low energy devices. The PEH's design should deliver the required performance demands depending on the specific device to be powered, to ensure reliable operation. Ideally, its design should be optimized such that its output power is maximized. If the PEH does not meet the performance requirements, the device it powers will not operate correctly. On the other hand, vastly exceeding the performance requirements of the PEH would potentially increase costs, and waste of the excess energy output. Using numerical models in the design of a PEH gives insight into its performance, which can assist in the optimization of its design, to increase overall efficiency. An FE model of a PEH is developed in this chapter to simulate its performance, which is compared with experimental testing for validation.

The performance of the PEH is tested with and without an added proof mass. Attaching a proof mass to the energy harvester can be useful to reduce the fundamental frequency of the PEH when operating in an environment with excitation of low frequency. The effects of the proof mass are examined in terms of the fundamental frequency, transmissibility function, voltage and power output of the PEH. Further, the effects of the electrical load on the power output of the PEH are investigated for both the configurations. Impedance matching is an important consideration in the performance of a PEH, as it maximizes the power output of the PEH [96]. By varying the electrical load on the circuit and computing the corresponding power output of each corresponding resistance, the impedance matched resistance is found, which corresponds to the maximum power output.

Figure 5.1 shows the geometry of a cantilever beam attached by a PEH and a proof mass, where the green, grey, and orange shaded areas represent the piezo-ceramic material, stainless-steel beam, and proof mass, respectively. The geometry of the configuration without the proof mass is identical, with the proof mass removed. The proof mass is a magnet of 29 g, which can be attached or removed from the PEH when required. The piezo-ceramic patch is glued to the stainless-steel beam using the 3M electrically conductive adhesive transfer tape 9707. Table 3.1 displays the material properties of the stainless-steel beam and proof mass. Only the density of the proof mass is known, thus, the remaining properties are assumed to be the same as the

stainless-steel material. This assumption is reasonable, since the deformation of the proof mass is insignificant, and it has a negligible impact on the stiffness of the beam. The structural material properties of the adhesive tape are not provided by the manufacturer. Further, the adhesive tape is assumed to have a negligible impact on the PEH, and is not considered in the FE model. Thus, the available adhesive tape material properties are not listed in this work, but the technical data sheet is found in the following reference [97].

Table 5.1: Stainless-steel beam and proof mass material properties

Stainless-steel Young's Modulus	200 GPa
Stainless-steel Density	8,000 kg/m^3
Stainless-steel Poisson's Ratio	0.29
Proof mass Young's Modulus	200 GPa
Proof mass Density	8,200 kg/m^3
Proof mass Poisson's Ratio	0.29

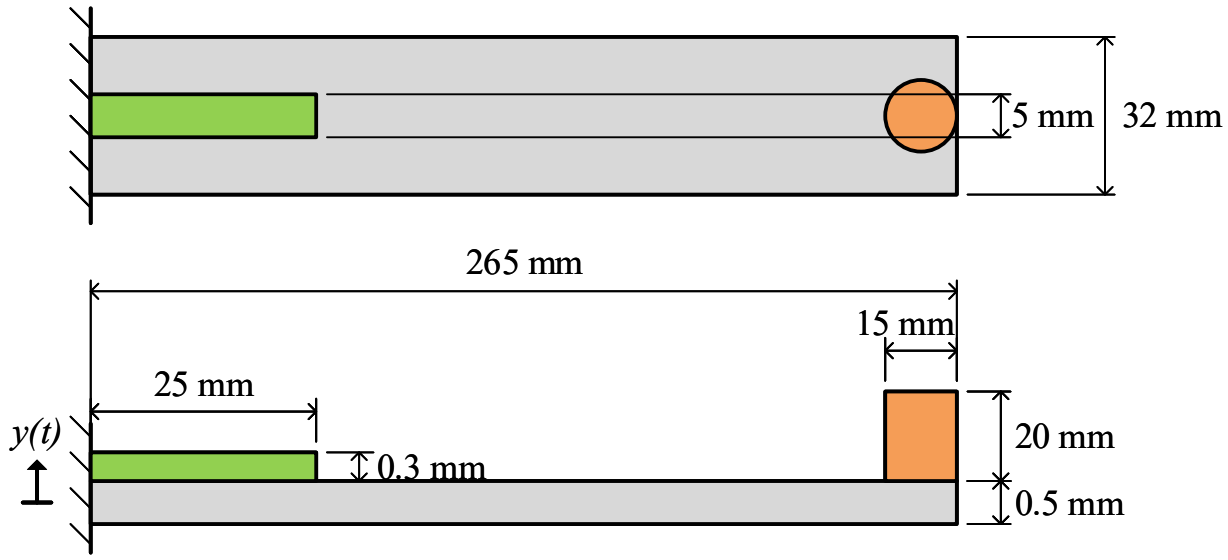

Figure 5.1: PEH geometry with the proof mass (not drawn to scale)

The piezo-ceramic material used is the PZT-5H manufactured by Steminc. Only selected material property components are given by the piezo-ceramic material manufacturer (see Appendix). Specifically, the piezoelectric coefficients d_{33} and d_{31}, the elastic compliance components s_{11} and s_{33}, and the dielectric permittivity component e_{33}. Thus, the absent material properties are provided by the built in PZT-5H material provided by Comsol, which is modified

to suit the material property components given by the manufacturer where available. It can also be assumed that $s_{11} = s_{22}$, $s_{13} = s_{23}$, $s_{44} = s_{55}$, $d_{31} = d_{32}$, and $d_{15} = d_{24}$, according to [98]. Thus, the material properties of the PZT-5H are defined as follows:

$$\mathbf{d} = \begin{bmatrix} 0 & 0 & 0 & 0 & 7.41 \times 10^{-10} & 0 \\ 0 & 0 & 0 & 7.41 \times 10^{-10} & 0 & 0 \\ -2.7 \times 10^{-10} & -2.7 \times 10^{-10} & 6 \times 10^{-10} & 0 & 0 & 0 \end{bmatrix} \left(\mathrm{C/N}\right)$$

$$\mathbf{s} = \begin{bmatrix} 1.39 \times 10^{-11} & -4.78 \times 10^{-12} & -8.45 \times 10^{-12} & 0 & 0 & 0 \\ & 1.39 \times 10^{-11} & -8.45 \times 10^{-12} & 0 & 0 & 0 \\ & & 1.89 \times 10^{-11} & 0 & 0 & 0 \\ & & & 4.35 \times 10^{-11} & 0 & 0 \\ & \text{Sym.} & & & 4.35 \times 10^{-11} & 0 \\ & & & & & 4.26 \times 10^{-11} \end{bmatrix} \left(\mathrm{1/Pa}\right)$$

$$\mathbf{e} = \begin{bmatrix} 3{,}130 & 0 & 0 \\ & 3{,}130 & 0 \\ \text{Sym.} & & 3{,}500 \end{bmatrix}$$

The density and quality factor of the piezo-ceramic material are 7,800 kg/m^3 and 80, respectively.

5.1. Finite Element Model

Developing an FE model of the PEH adds further complexity than those from the previous chapters, as it involves dynamics and multi-physics coupling. Since the PEH converts mechanical energy input to electrical energy output, the FE model must include an electro-mechanical coupling. This requires the use of additional boundary conditions to effectively characterize the PEH. Further, the inclusion of multi-physics increases the model's degrees of freedom, thus increasing computational demand.

Building from the modeling simplifications presented in the previous chapters, the PEH is modelled in 2D. The electrically conductive adhesive transfer tape is neglected due to its negligible impact on the PEH structure. The adhesive has a thickness of 50 μm, which is much thinner than the piezo-ceramic and stainless-steel beam. This would require a significant increase in the number of elements used in the model for an insignificant impact on the results. Further, the adhesive tape has an electric resistance less than 0.5 Ω for a 2 mm x 5 mm area. This is equivalent to an electrical resistance of less than 6.25 Ω for the PEH, which is insignificant compared to the resistances used for impedance matching. The FE model is

developed in the following, including mesh design, study and physics, boundary conditions, and post-processing.

Figure 5.2 shows the general geometry of the PEH FE model with the added proof mass. The proof mass used for the physical PEH, shown in Figure 5.1, is cylindrical in shape which cannot be modelled in 2D. Instead, the FE model represents the proof mass as two square cross-section rectangular prisms which span the out-of-plane width of the stainless-steel beam. The cross-sectional area of the proof mass in the FE model is selected such that it has a total volume equivalent to the physical proof mass. This ensures that the total mass of the proof mass is approximately 29 g in the FE model.

Figure 5.2: Geometry of the PEH FE model with the proof mass

5.1.1. PEH Model Mesh

The model mesh of the PEH without the proof mass is user-defined, while the PEH with the proof mass includes elements automatically generated by the FE software. Since the PEH is subjected to in-plane transverse vibration, the quadratic quadrilateral elements are used for the piezo-ceramic domain and the stainless-steel beam. Since the proof mass experiences insignificant bending stresses, its domain is meshed using quadratic triangular elements.

Since the FE model involves the coupling of mechanical and electrical physics, the number of degrees of freedom is inherently increased when compared with an FE model involving single physics. Thus, a computationally efficient model mesh is desired as the number of elements used is directly related to the model's degrees of freedom. For the PEH without the proof mass, the piezo-ceramic domain and the stainless-steel beam use one quadratic quadrilateral element through their thickness. Along their lengths, the piezo-ceramic domain and the stainless-steel beam use 50 and 532 quadratic quadrilateral elements, respectively. This yields a total of 582 elements, with an average and minimum element quality of 0.9899 and 0.8824, respectively. The PEH with the proof mass uses the same mesh for the piezo-ceramic domain and the stainless-steel beam. However, the proof mass domains are represented by

quadratic triangular elements, generated by the software package with a normal mesh density. Using triangular elements is suitable as it is assumed that the proof mass will experience negligible bending stress. The software package automatically generates a mesh to ensure continuity with the smaller quadratic quadrilateral elements, regardless of the minimum element size setting defined by the mesh density. The proof mass domains are represented by 244 quadratic triangular elements. This yields 826 total elements for the PEH with the proof mass FE model, with an average and minimum element quality of 0.9751 and 0.7802, respectively. Figure 5.3 shows the FE model mesh for the PEH with the proof mass, including detailed views of the piezo-ceramic domain, and the proof mass domain, to clearly illustrate the mesh elements. The FE model mesh of the PEH without the proof mass is the same, apart from the proof mass.

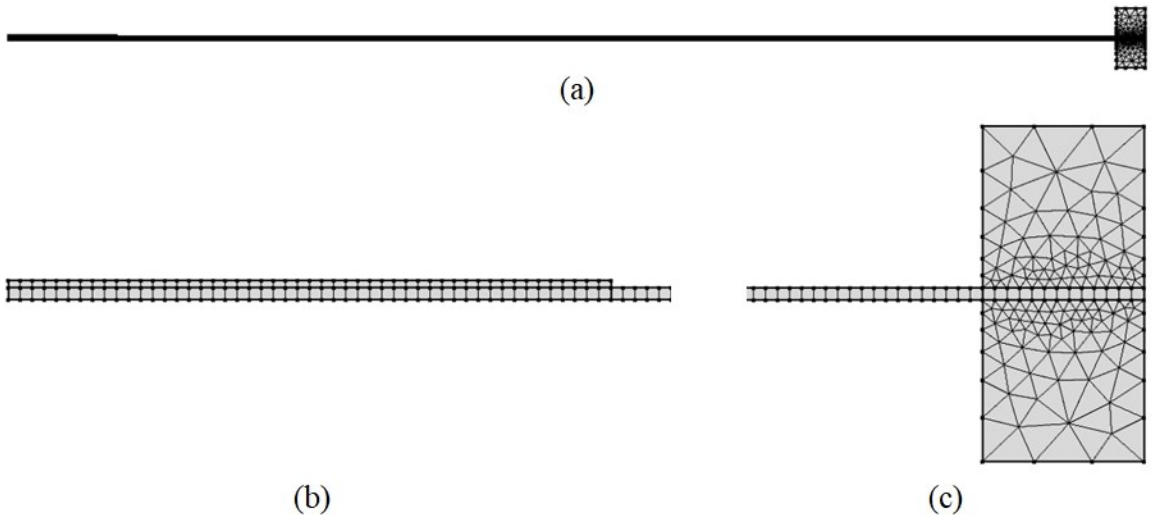

Figure 5.3: PEH with the proof mass FE model mesh: (a) complete FE model mesh; (b) piezo-ceramic domain detail; (c) proof mass domain detail

5.1.2. Physics and Study

The PEH for both the configurations require a dynamic multi-physics FE model to evaluate the voltage load dependence, impedance matching, and transmissibility function. The FE model includes the solid mechanics, the electrostatics, and the electrical circuit physics. Further, the piezoelectric devices multi-physics coupling is used to couple the electro-mechanical physics interaction. A time dependent and a frequency dependent study are used to solve for the output of the PEH and its dynamic behaviours.

The solid mechanics physics are applied to every component of the PEH, which solves the displacement field of the PEH. The electrostatics physics are applied only to the piezo-ceramic domain, which solves for its electric potential. The piezo-ceramic domain includes both the solid mechanics and electrostatics physics. Thus, the piezoelectric devices multi-physics coupling is automatically applied to the piezo-ceramic domain. Further, the electrical circuit physics are applied, which incorporate the effects of the load resistance. Instead of applying the electrical circuit physics to a domain, it interacts with the FE model through appropriate boundary conditions, which are detailed in Section 5.1.3.3.

The time dependent study is used to determine the transmissibility function of the PEH. Like Chapter 3, the transmissibility function is found by an excitation frequency sweep, corresponding to the range used in the experiment, which are discussed in Section 5.2. The transmissibility function of each PEH configuration is evaluated at the impedance matched resistance. A time duration of 10 seconds is used to collect the time response for the PEH without the proof mass, where the final 2 seconds represent the steady state solution, used to compute the transmissibility ratio for each excitation frequency. It was difficult for the PEH with the proof mass to achieve steady state operation. Thus, a 50 second time duration is used in an attempt to minimize the transient response, where the final 2 seconds were used to determine the transmissibility ratios. The difficulty in achieving a steady state response is observed in Section 5.3.2.

The frequency dependent study is employed to compute the voltage load dependence and impedance matching. Although this could be done with a time dependent study, the frequency dependent study is computationally efficient by comparison, since the software solves the steady state solution directly. Furthermore, the frequency dependent study is suitable in this case, since the output from the PEH is determined by the strain energy of the piezo-ceramic material. Thus, the relative displacement of the input and output locations are not necessary to determine the voltage and power output.

To determine the voltage load dependence and impedance matching, an auxiliary sweep of the load resistance is performed. The resistance is varied between a range of 500 Ω - 3 MΩ for the PEH without the proof mass, and 500 Ω - 10 MΩ for the PEH with the proof mass. The

PEH with the proof mass requires a higher resistance for impedance matching, which is discussed in Section 5.3.1.

5.1.3. Boundary Conditions

The boundary conditions for each physics module are discussed in the following. For both PEH configurations, the boundary conditions are the same. However, the settings for some of the boundary conditions are different to suit each configuration. For example, the damping model for each PEH configuration must of course be tuned individually.

5.1.3.1. Solid Mechanics

The solid mechanics physics module includes the material models for the PEH components. The linear elastic material model is applied to the stainless-steel beam and proof mass domain, while the piezoelectric material model is applied to the piezo-ceramic domain. The piezoelectric material allows the user to define the piezoelectric constitutive relation. Since the material properties provided by the manufacturer are based on the strain-charge form, it is used as the constitutive relation for the piezoelectric material. Within the linear elastic and piezoelectric material models, the Rayleigh damping and dielectric loss are defined, respectively. The dielectric loss is selected as 1.25%, which is the inverse of the piezo-ceramic material quality factor.

The PEH is intended to operate at its fundament frequency. Thus, the Rayleigh damping is tuned using only the fundamental frequency, which differs from the approach detailed in Section 3.1.2 from Chapter 3 Chapter 3. Comsol suggests that the Rayleigh damping can be modified to represent an equivalent viscous damping model at the resonant frequency by considering only the stiffness proportional term [91]. This gave a significantly overdamped displacement response. Another approach, explored by Charney [99], is to consider only the mass proportional term. This approach is suitable in the low frequency range, since the mass proportional term of Rayleigh damping is dominant in this range. In the high frequency range, it shows poor performance, since the damping tends to zero when the stiffness proportional term is neglected. Using this approach, the Rayleigh damping is modified as follows:

$$\mathbf{C} = \mu\mathbf{M} \tag{5.1}$$

$$\zeta_n = \frac{\mu}{4\pi f_n}$$
$$\mu = 4\pi\zeta_n f_n \tag{5.2}$$

In equation (5.2) the subscript *n* is equal to 1, since the fundamental frequency of the PEH is used.

The time dependent study requires different boundary conditions than the frequency dependent study in terms of applied loads and constraints. A prescribed displacement is applied to the base of the PEH in the time dependent study to simulate base excitation, like the prescribed displacement applied in the FE models from Chapter 3. In fact, the same sinusoidal displacement function given by equation (3.5) from Chapter 3 is applied. For the frequency dependent study, a fixed constraint and body load replace the prescribed displacement. The fixed constraint is applied to the base of the PEH structure. The body load is applied to all the PEH domains, and the applied load are described in terms of g-force. The voltage output across the load resistor of the PEH scales linearly with the applied body load. Since the applied g-force from the experiment is not measured, the FE model initially uses a body load of 1 g-force. The voltage corresponding to the impedance matched resistance is then scaled by the experimental one to determine the g-force which gives voltage and power output results comparable to the experiment. This yields a body load of approximately 1.2 x 10^{-3} g-force and 1.0 x 10^{-3} g-force for the PEH without the proof mass and with the proof mass, respectively.

5.1.3.2. Electrostatics

The electrostatics boundary conditions are the same for both the time dependent and frequency dependent study. The boundary conditions applied to the PEH are the ground and terminal nodes. The ground node is applied to the top of the piezo-ceramic domain, while the terminal node is applied to the interface of the piezo-ceramic and stainless-steel beam domain. Within the terminal settings, the terminal type is selected as a circuit, such that the terminal can be used by the electrical circuit physics.

5.1.3.3. Electrical Circuit

The electrical circuit module allows for an electrical circuit to be linked to the FE model. The electric circuit is the same for both the time dependent and frequency dependent study. The electrical circuit includes a ground node, a resistor, and an external terminal. The resistance of

the resistor is varied, which is used to determine the voltage load dependence and the output power load dependence. The external terminal is linked to the terminal discussed in 5.1.3.2.

5.1.4. Post-Processing

The transmissibility functions of the specimens are found using the method described in Section 4.1.1 from Chapter 4. The input and output displacements are measured at the base and 5 mm from the free end, respectively. These displacements are measured from the time dependent study. The RMS amplitude of the input and output displacements are used to compute the transmissibility function for each PEH configuration.

To evaluate the voltage load dependence, the voltage output across the load resistor is evaluated for each resistance used in the auxiliary sweep from the frequency dependent study. Since the resistor is not discretely modelled, a global evaluation of the resistor from the electrical circuit module is used. The absolute voltage across the resistor is measured. The voltage output is necessary to compute the power output of the PEH to perform impedance matching. The power output of the PEH for each resistance value is computed as follows:

$$P = \frac{V^2}{R} \tag{5.3}$$

where, P, V, and R represent the power output, voltage output, and resistance, respectively. Impedance matching is performed by plotting the power output versus load resistance to find the resistance which corresponds to the maximum power output.

5.2. Experimental Data Collection

The experimental apparatus detailed in Chapter 4 is used to measure the voltage load dependence, impedance matching, and the transmissibility function of both the PEH configurations. The signal processing techniques applied to the PEH data are the same as described in Section 4.1.2 from Chapter 4. The same filter design is applied to the experimental data to remove noise, and zero padding is used to improve the frequency spectrum resolution, and prevent spectral leakage.

Figure 5.4 shows the experimental configuration of the PEH. To measure the voltage load dependence and impedance matching, a load resistor (the blue component) is connected to the leads of the piezo-ceramic material. To measure the voltage across the load resistor the black

and red leads are connected across the it and are sent to the data acquisition unit. To determine the voltage load dependence and impedance matching, the PEH is excited at its fundamental frequency. The fundamental frequency of the PEH without the proof mass and with the proof mass determined by the FE model is 6.7 Hz and 3.4 Hz, respectively. Once the PEH's response reaches steady state, the voltage output across the resistor is recorded over a time duration of two seconds. This process is conducted for load resistances of 500 Ω, 1 kΩ, 2 kΩ. 5 kΩ, 10 kΩ, 20 kΩ, 50 kΩ, 100 kΩ, 200 kΩ, 500 kΩ, 1 MΩ, 2 MΩ, and 3 MΩ for the PEH without the proof mass, while the PEH with the proof mass also includes load resistances of 5 MΩ, and 10 MΩ.

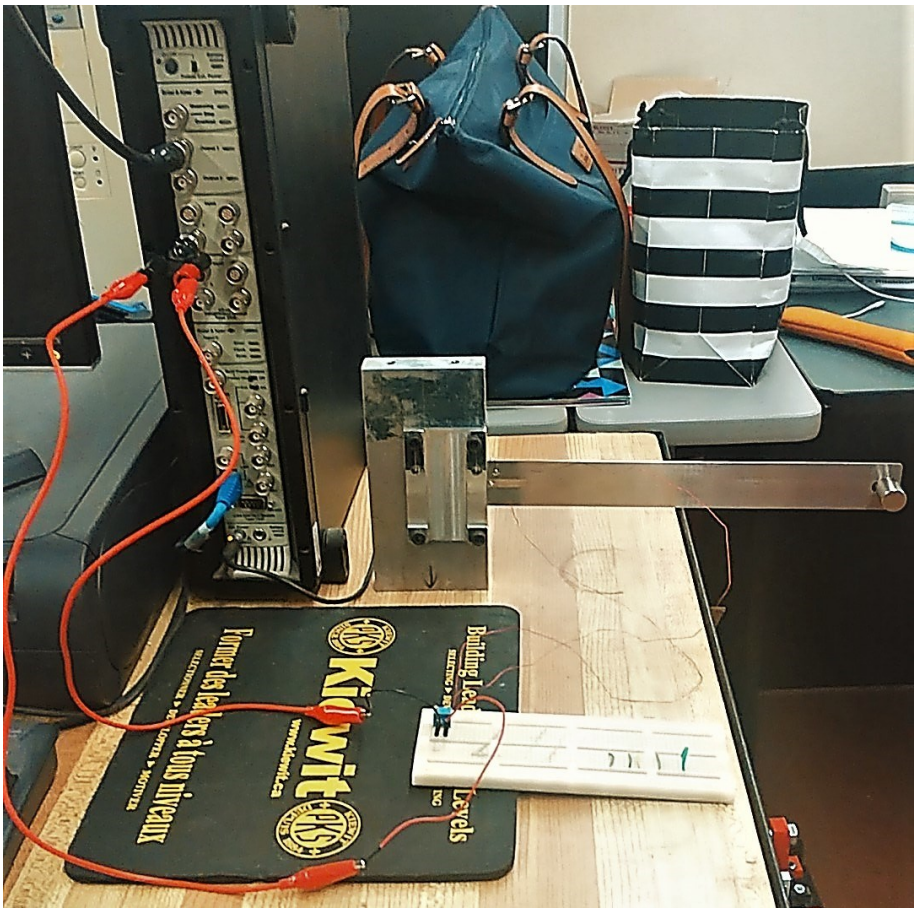

Figure 5.4: Experimental configuration of the PEH

Determining the transmissibility functions of the PEH is similar to the method in Section 4.1.1 from Chapter 4, with slight modifications. Since the electrical circuit is attached during the measurement of the transmissibility functions, the impedance matched load resistance is applied. Since the PEH is intended to operate at its fundamental frequency, the transmissibility functions

are found for a relatively narrow frequency range, unlike those from Chapter 4. The driving frequency ranges of the PEH without the proof mass and the PEH with the proof mass are between 4 Hz – 10 Hz and 3 Hz – 4 Hz, respectively. Since these are relatively narrow, the time required for data collection is significantly reduced. Thus, a finer frequency resolution is used to determine the transmissibility function. The frequency resolutions of the PEH without the proof mass are 0.25 Hz and 0.10 Hz when far from and near the resonant frequency, respectively. The frequency resolution of the PEH with the proof mass is 0.05 Hz throughout the frequency sweep, since the frequency range considered is particularly narrow.

5.3. Results

The experimental and simulation results of both PEH configurations are presented and discussed, including the voltage load dependence, impedance matching, and transmissibility functions. The simulation results are compared with the experimental ones, to validate the performance of the PEH FE models. Finally, the performance of the PEH without the proof mass and the PEH with the proof mass are compared.

5.3.1. PEH Voltage Load Dependence and Impedance Matching

Figure 5.5 shows the voltage load dependence, determined experimentally and by the FE model, of the PEH without the proof mass. In general, the voltage load dependence determined by the FE model is in close agreement with the experiment. The voltage output tends to increase with an increasing load resistance for the resistance sweep considered. The voltage load dependence curves, determined by the experiment and the FE model, are concave upwards up to the inflection point at a load resistance of 1 MΩ, where the curve becomes concave downwards. The maximum voltage outputs determined by the experiment and the FE model are 0.517 V and 0.554 V, respectively.

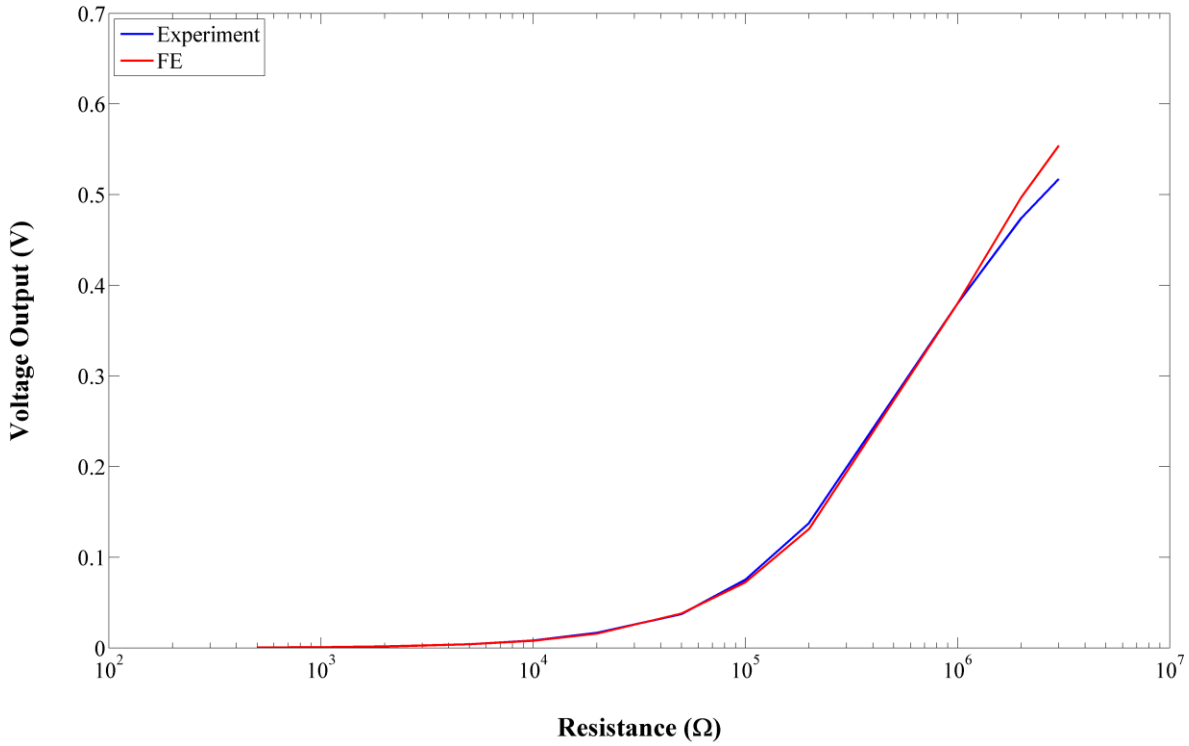

Figure 5.5: Voltage load dependence of the PEH without the proof mass

Figure 5.6 shows the impedance matching curves for the PEH without the proof mass, determined experimentally and by the FE model. It can be seen that the impedance matching curve determined by the FE model compares favorably with the experimental one. In both the experimental and the FE results, the power output reaches a maximum at a load resistance of 1 MΩ, which corresponds to the location of the inflection point shown in Figure 5.5. This load resistance is the impedance matched resistance of the PEH without the proof mass. The maximum power output magnitude measured by the experiment of 144 nW is the same as the maximum power output magnitude determined by the FE model. Of course, this is expected since the FE model body load is scaled based on the voltage output at the impedance matched resistance.

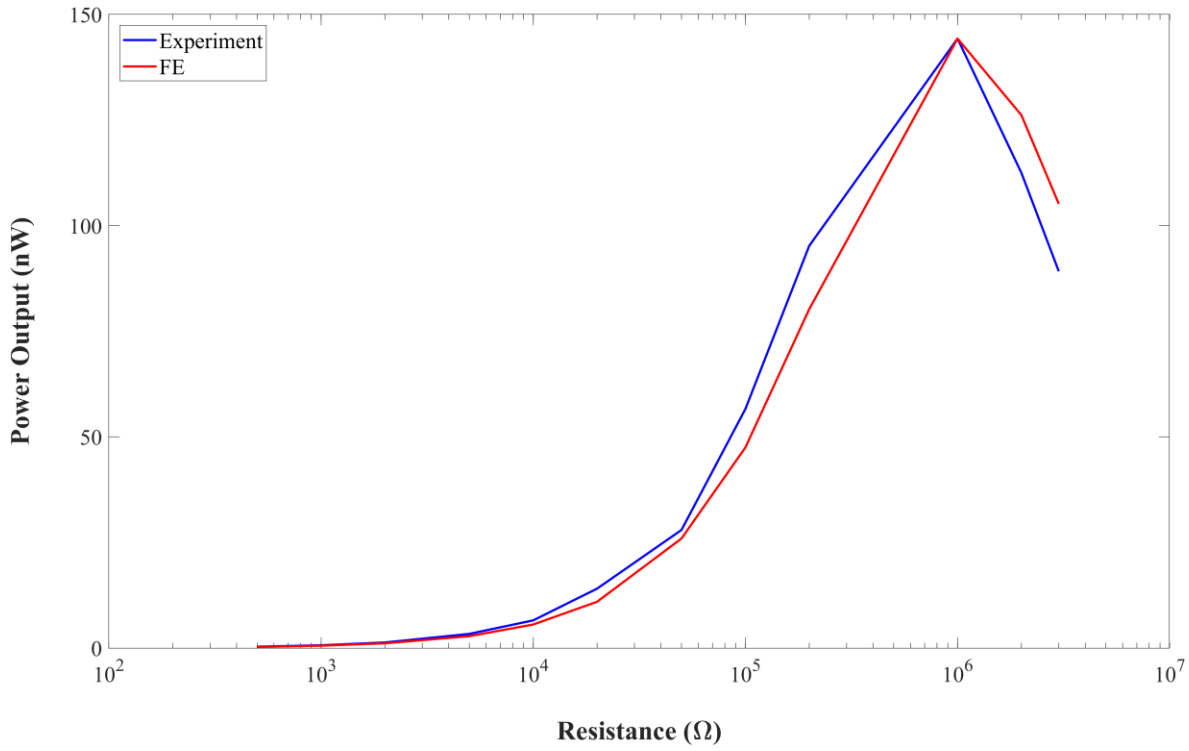

Figure 5.6: Impedance matching of the PEH without the proof mass

The voltage load dependence, determined experimentally and by the FE model, of the PEH with the proof mass are shown in Figure 5.7. The voltage load dependence determined by the FE model compares well with the experiment, showing a similar trend. Like the voltage load dependence from Figure 5.5, increasing the load resistance causes an increase in the voltage output across the resistor. In this case, the inflection point location in the voltage load dependence curve differs between the experiment and the FE model. The inflection point of the voltage load dependence curve determined by the experiment is located at a load resistance of 2 MΩ, whereas the FE model shows the inflection point at a load resistance of 3 MΩ. It can be seen that the FE model uses more load resistances in the resistance sweep than the experiment. This is done to show the general trend of the voltage load dependence curve determined by the FE model beyond the inflection point, which is useful for impedance matching. Thus, the voltage outputs, determined experimentally and by the FE model, at a load resistance of 3 MΩ are 0.170 V and 0.188 V, respectively.

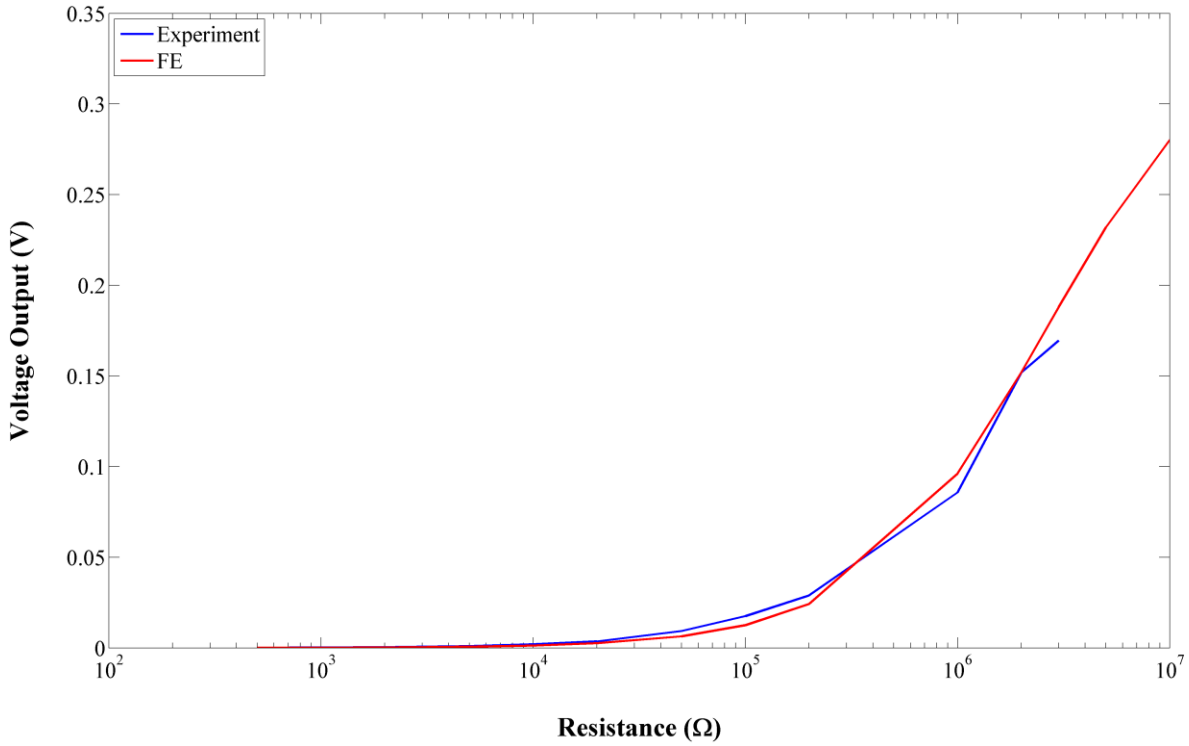

Figure 5.7: Voltage load dependence of the PEH with the proof mass

The impedance matching curves for the PEH with the proof mass, determined experimentally and by the FE model, are shown in Figure 5.8. It can be seen that the overall trend of the impedance matching curve determined by the FE model compares well with the experiment. The maximum power outputs correspond to the locations of the inflection points from the voltage load dependence curves. The impedance matched resistance determined by the experiment is 2 MΩ, which gives a maximum power output of 11.5 nW. The impedance matched resistance determined by the FE model is 3 MΩ, giving a maximum output of 11.8 nW. In this case, the maximum power outputs are different, since the FE body load is scaled by the voltage corresponding to then experimental impedance matched resistance, which can be seen in Figure 5.8, since the power output is the same at a 2 MΩ.

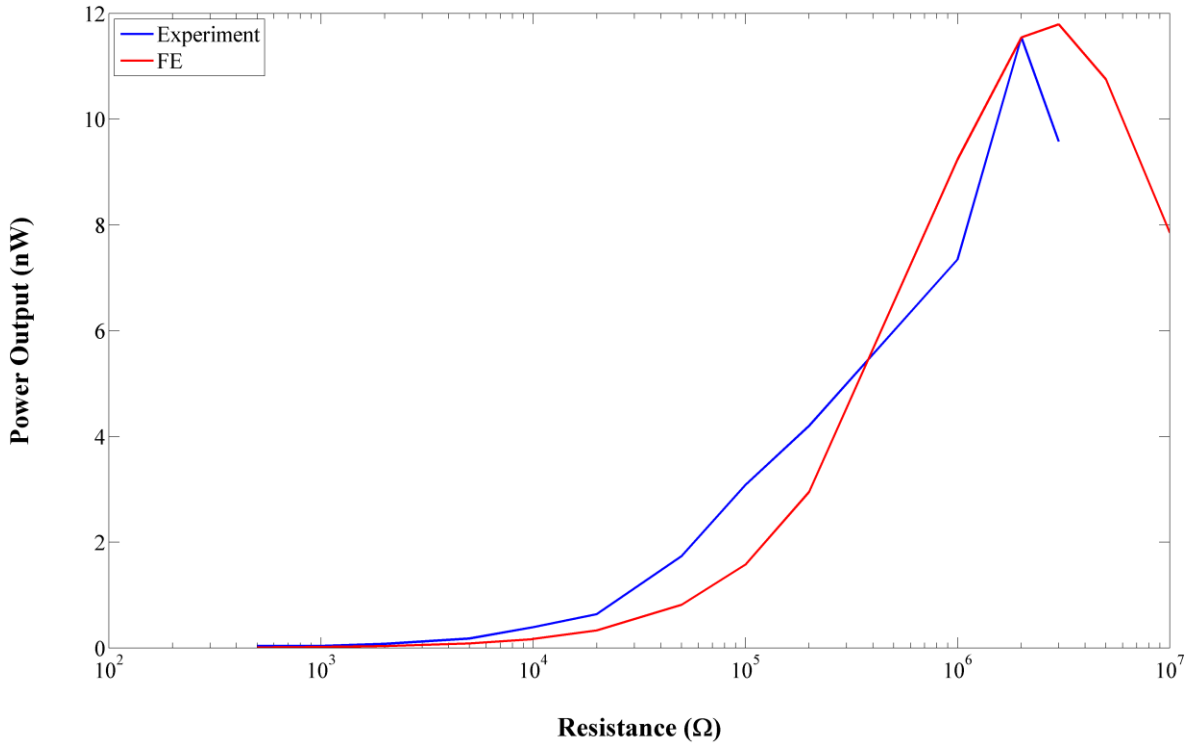

Figure 5.8: Impedance matching of the PEH with the proof mass

5.3.2. PEH Transmissibility Functions

The measured damping ratios of both the PEH configurations are listed in Table 5.2. The damping ratios are determined using the quadrature peak picking method described in Section 4.1.1 from Chapter 4. It can be seen that the damping ratio of the PEH without the proof mass is significantly larger than the damping ratio of the PEH with the proof mass.

Table 5.2: PEH damping ratios

PEH Configuration	Damping Ratio ζ_1
With the proof mass	6.675×10^{-3}
Without the proof mass	1.247×10^{-2}

Figure 5.9 shows the transmissibility functions of the PEH without the proof mass, determined experimentally and by the FE model. The transmissibility function determined by the FE model shows good agreement with that determined by the experiment. The fundamental frequency determined by the FE model is 6.7 Hz, whereas the experimental fundamental

frequency is 6.5 Hz, giving a relative error percentage of approximately 3.08%. The transmissibility function magnitudes at the fundamental frequency determined by the FE model and the experiment are 72.07 and 69.03, respectively. These magnitudes are within an order of magnitude and give a relative error percentage of approximately 4.40%.

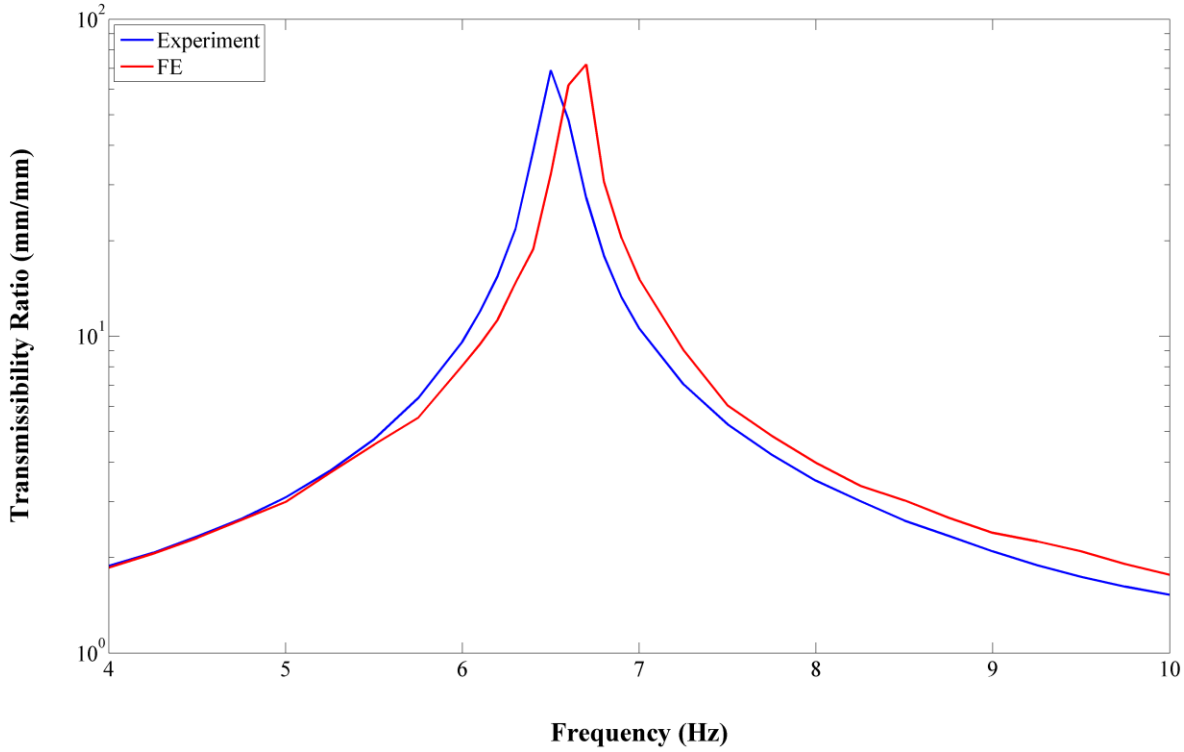

Figure 5.9: Transmissibility function of the PEH without the proof mass

Figure 5.10 shows the transmissibility functions determined experimentally and by the FE model for the PEH with the proof mass. In general, the transmissibility function determined by the FE model compares well with that by the experiment. However, it can be seen that the transmissibility function determined by the FE model is not as smooth as that by the experiment. Section 3.1.4 mentions that the time response of the PEH determined by the FE model did not reach steady state for some of the driving frequencies. This explains the poor smoothness of the transmissibility function determined by the FE model. The fundamental frequency found experimentally is 3.35 Hz, whereas the fundamental frequency determined by the FE model is 3.4 Hz, giving a relative error percentage of approximately 1.49%. The transmissibility function

magnitudes at the fundamental frequency determined by the FE model and the experiment are 99.17 and 119.60, respectively, giving a relative error percentage of approximately 17.08%.

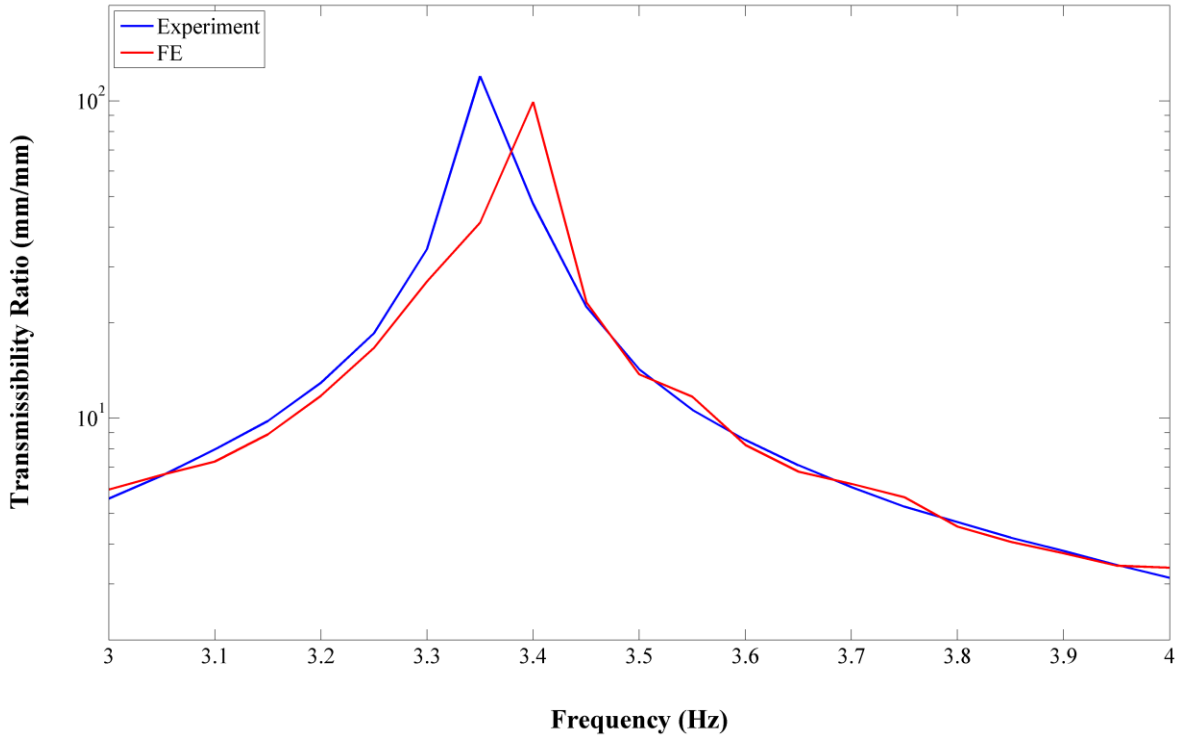

Figure 5.10: Transmissibility function of the PEH with the proof mass

5.3.3. Impact of the Proof Mass

Comparing the transmissibility functions, determined experimentally, of both the PEH configurations leads to key insights. Most obviously, the fundamental frequency of the PEH is directly impacted by the proof mass. This is useful for tuning the PEH to suit the ambient excitation frequency of the operating environment. Ensuring that the PEH is excited at its fundamental frequency increases its power output, which is desired. Further, the transmissibility function magnitude at the fundamental frequency for the configuration with the added proof mass is larger than the magnitude for the configuration without the proof mass. Thus, for a given input displacement applied to both the PEH configurations, the configuration with the proof mass has a larger free end displacement, which should increase the strain energy of the piezo-ceramic material.

Interestingly, the maximum power output of the PEH without the proof mass is significantly larger than the PEH with the proof mass. Their respective impedance matched power outputs are 144 nW and 11.8 nW. This seems to conflict with the expected increase in piezo-ceramic strain energy caused by the added proof mass. However, this could be related to the mechanical power input, which may have been higher for the PEH without the proof mass. Since the mechanical power input was not measured experimentally, the FE model is used to estimate it. It is found that the simulation mechanical power input for the PEH without the proof mass and the PEH with the proof mass are 905 nW and 63.5 nW, respectively. These give respective efficiencies of 15.94% and 18.17%. Therefore, the increased efficiency of the PEH with the proof mass suggests that the low power output relative to the PEH without the proof mass is related to its mechanical power input. This of course requires experimental validation, since the mechanical power input determined by the FE model is based on the scaled applied body load.

The proof mass tends to cause an increase in the impedance matched resistance. Comparing the impedance matching curves of both the configurations in Figure 5.6 and Figure 5.8, it can be seen that the impedance matched resistance without the proof mass is 1 MΩ, whereas the addition of the proof mass increases it to 2 MΩ. This suggests that increasing the proof mass could be a way to tune the impedance matched resistance of the piezo-ceramic material.

5.4. Conclusion

This chapter focused on the numerical modeling of the dynamic response and performance output of a PEH. The effects of an added proof mass were explored and compared with the performance of the PEH without the proof mass. The transmissibility functions, voltage load dependence, and impedance matching for each PEH configuration were found experimentally and by the FE model. The performance of the FE models compares well with the experimental results. The FE model shows trends which compare well with the experiment. The transmissibility functions and fundamental frequencies determined by the FE models were validated by the experimental ones. However, further analysis should be done to validate the performance of the FE model with respect to the voltage load dependence, and impedance matching results, since the body load magnitude was scaled based on the experimental

impedance matched output voltage. With that said, the FE results presented for the PEH electrical output performance are encouraging, and future work should be conducted to validate these.

Chapter 6 Conclusion and Recommendations

6.1. Conclusion

This research explored the use of numerical analysis approaches to study discontinuous beam structures in several applications. Specifically, the focus of the study is placed on the static and dynamic behaviours that involve single physics or multi-physics. Both the static single physics, and dynamic single physics cases were represented by modelling an adhesively bonded SLJ, whereas the dynamic multi-physics case was represented by modelling a PEH. In both the adhesively bonded SLJs and PEHs, material and geometric discontinuities exist. The FEM was used for all the three applications. A commercial FE software package Comsol Multiphysics was used to implement the FE simulations. In addition, the TMM was employed as an alternative numerical approach in the dynamic single physics scenario. The models used for simulation were discussed in detail, and their performance was evaluated by the analytical approaches and experimental testing. Furthermore, the impact of certain design considerations was investigated in each of the applications.

An experimental apparatus was developed and benchmarked, to validate the performance of the numerical analysis approaches. The iterative design of the apparatus highlighted the shortcomings of the original experimental apparatus, and the modifications necessary to improve the measurement quality in the revised apparatus. Data collection equipment and signal processing techniques were discussed in detail, including the use of zero padding and a Butterworth filter to prevent spectral leakage, improve the frequency domain resolution, and remove unwanted noise. The measured natural frequencies and mode shapes closely matched the analytical ones of the benchmark beam. Thus, the revised experimental apparatus was used to measure the dynamic behaviours of the adhesively bonded SLJs and the PEHs, as well as the electrical performance output of the PEHs.

An FE model was developed to model the shear and peel stress distribution within the adhesive layer of an adhesively bonded SLJ. Classical analytical approaches including the shear lag model, the Goland and Reissner Model, and the Hart-Smith model, were used to validate the FE model. Three distinct FE mesh designs were used to determine which mesh design gave the results that most favorably matched those from the analytical approaches. The shear and peel stress distributions determined by the selected FE model mesh design compared favorably with

those from the analytical approaches. The effect of the adhesive layer thickness on the stress distribution within the adhesive layer was investigated. It was shown that an increase in the adhesive layer thickness resulted in a reduction of the maximum shear and peel stresses. Also, the location of the maximum shear and peel stresses shifted towards the middle, away from the ends, of the overlap region. Further, increasing the adhesive layer thickness resulted in more evenly distributed shear and peel stress distributions. These relationships could be useful in the design of adhesively bonded SLJs.

The effects of the adhesive layer thickness, and the overlap length on the dynamic behaviours of an adhesively bonded SLJ were investigated. A single variable TMM model updating approach was proposed to determine the effective Young's modulus of the overlap region. This method was compared with the commonly used additive approach to determine the effective material properties of the overlap region. An FE model was used to estimate the natural frequencies used as model updating targets in the single variable TMM model updating approach. The natural frequencies and modes shapes of the SLJ specimens were determined. It was found that the TMM using the effective Young's modulus determined by the single variable TMM model updating approach more favourably matched the FE results than the TMM using the effective Young's modulus determined by the additive approach. It was also shown that the effective Young's modulus determined by the single variable TMM model updating approach was robust. The natural frequencies of an adhesively bonded SLJ were reduced when the adhesive thickness was increased, due to the increased adhesive mass and reduction in the overlap region rigidity. Further, increasing the length of the overlap region caused an increase in the natural frequencies of the SLJ specimens.

The natural frequencies, mode shapes, damping ratios, and transmissibility ratios of the adhesively bonded SLJ specimens were found experimentally to validate the results obtained by the FE simulations. It was shown that the natural frequencies and mode shapes determined by the FE model and the TMM, using the effective Young's modulus determined by the single variable TMM model updating approach, compared favourably with the experimental ones. The experimentally determined damping ratios were used in the FE model to determine the transmissibility functions of the specimens. It was found that the transmissibility functions

determined by the FE model compared well with the experimental ones. This validated the applicability of using the FE model to find the transmissibility functions of the SLJ specimens.

A multi-physics FE model was employed to model the dynamic behaviours and electrical generation performance of a PEH. Experimental measurement was done to validate the performance of the FE model. Two PEH configurations were considered including a PEH without the proof mass and a PEH with the proof mass. The effects of the added proof mass, the voltage load dependence, and the impedance matching of the PEH were investigated. The voltage load dependence, impedance matching, and transmissibility functions determined by the FE model closely matched the experimental ones. Therefore, the ability of the FE model to represent the PEH was validated. It was found that the added proof mass significantly reduced the natural frequencies of the PEH, dramatically increased the resonant amplitude of the transmissibility function, and caused an increase in the impedance matched resistance of the PEH. It was shown that the PEH with the added proof mass gave a lower power output than the PEH without the proof mass. A reason for this could be related to the lower mechanical power input for the PEH with the proof mass. These relationships play an important role in designing an optimized PEH.

This research has shown the ability for the numerical analysis approaches to model discontinuous beam structures. Overall, in the applications presented, it was shown that the results from the numerical analysis approaches closely match the analytical and experimental results. Key relationships within each application were demonstrated, which could be useful in design. Limitations in the research were discussed throughout, and suggestions are made in the recommendations section. This work has presented the successful application of the numerical analysis approaches in multiple applications.

6.2. Recommendations for Future Study

When numerically modelling the adhesive peel and shear stress distributions within an adhesively bonded SLJ, the applied load was within the elastic region of the adhesive material. Plastic deformation within the adhesive layer would have a significant impact on the peel and shear stress distributions. According to the Hart-Smith model, plastic deformation would initiate at the ends of the overlap region and move inwards with increasing applied load [31]. Investigating the effect of applied loads causing plastic deformation would require the

development of more advanced adhesive material models in the FE software package which include the material plasticity and hardening function. A material model of this sort could show the effects of the plasticity on the adhesive peel and shear stress distributions for high applied loads. Further, a time dependent model could be used to determine the residual strain within the adhesive layer once the applied load is removed.

The effect of the adhesive layer thickness on the dynamic behaviours of adhesively bonded SLJs were studied numerically in this work. The simulations showed that increasing the adhesive layer thickness would cause a reduction in the specimen's natural frequencies due to the increased adhesive mass and reduction in the overlap region rigidity. Although the effect of the adhesive layer thickness is logical, the degree to which it impacts the natural frequencies should be measured experimentally to validate the numerical results. Further, the effects of the adhesive layer thickness on the transmissibility functions of adhesively bonded SLJs could also be investigated.

The robustness of the effective Young's modulus of the overlap region determined by the single variable TMM model updating approach was investigated in this work. The effective Young's modulus was determined for one overlap length, and then applied to adhesively bonded SLJs with different overlap lengths. The robustness was also tested by holding a constant adherend to adhesive thickness ratio. Future work could consider modifying the boundary conditions of the adhesively bonded SLJ to further investigate the robustness of the effective Young's modulus. For example, the free end of a cantilevered adhesively bonded SLJ could be fixed, giving fixed-fixed boundary conditions. The effective Young's modulus determined by the cantilevered configuration could then be applied for the fixed-fixed configuration. Changing the boundary conditions of an adhesively bonded SLJ could give further insight about the robustness of the effective Young's modulus determined by the single variable TMM model updating approach.

Investigating uncertainty in the model updating targets used by the single variable TMM model updating approach could be done. In this work, model updating was performed using a selective number of the known natural frequencies in sequential order. However, for example, if only the first and third natural frequencies of a system was known, how would the performance of the resulting effective Young's modulus be affected? In other words, how well would the

model updating scheme handle this uncertainty? This could be conducted with the experimental data collected in Chapter 4.

Future work could be conducted to investigate the performance of the single variable TMM model updating approach for adhesively bonded joints with other bond line configurations. In this work, the SLJ configuration was used. Determining the effective Young's modulus of an adhesively bonded scarf joint would be interesting, since the overlap region of the scarf joint is more complex than the SLJ. This could be done for all the joint configurations shown in Figure 1.1 from Chapter 1.

For future work, using the TMM for different joint designs can be explored – for example how well does the single variable TMM model updating work when a double lap/scarf/bevel/step/butt strap joint is considered? Could the TMM deal with, for example, the entire overlap area of a step joint as a single element, or would it be better to break up a step joint into multiple elements at each step discontinuity to improve results? Due to the geometry of a bevel joint, should the element representing it be bound by the terminus of the adhesive region, or should this element extend slightly beyond the adhesive terminus, including more of the adherends, to improve results?

The base excitation load applied to the PEH was not measured during the experimental data collection. For sake of comparison, the body loads used in the FE models of both the PEH configurations were scaled since the voltage load dependence and impedance matching curves scaled linearly with the body load magnitude. Scaling the body loads was useful to demonstrate that the voltage load dependence and impedance matching plots gave similar trends compared to the experimental ones. It is suggested that the excitation load applied to the PEH during the experiment should be measured to validate the simulation results. Further, the experimental power output for the PEH without the proof mass was one order of magnitude larger than the power output for the PEH with the proof mass, at the impedance matched resistance. The mechanical energy input required to excite the PEH during the experiment was not measured. However, the simulation results showed that the mechanical energy input for the PEH without the proof mass was higher based on the scaled body loads. Thus, it is suggested that further experimental testing be done to measure the mechanical energy input for both PEH configurations to verify the mechanical energy input determined by the FE model.

References

[1] Environment and Climate Change Canada, "Harper government improves fuel efficiency of Canadian vehicles," Government of Canada, 27 November 2012. [Online]. Available: http://www.ec.gc.ca/default.asp?lang=En&n=714D9AAE-1&news=33B625CB-653E-4766-8C92-ACA551C94AB0.

[2] T. Muhleman, "Fuel economy standards and the adhesives market," *Adhesives and Sealants Industry,* vol. 20, no. 3, pp. 10-11, 2013.

[3] A. Wagner, "Customized structural adhesives deliver multiple benefits," *Adhesives and Sealants Industry,* vol. 23, no. 9, pp. 20-24, 2016.

[4] X. He, "A review of finite element analysis of adhesively bonded joints," *International Journal of Adhesion and Adhesives,* vol. 31, pp. 248-264, 2011.

[5] J. Y. Cognard, M. Bourgeois, R. Créac'hcadec and L. Sohier, "Comparative study of the results of various experimental tests used for the analysis of the mechanical behaviour of an adhesive in a bonded joint," *Journal of Adhesion Science and Technology,* vol. 25, no. 20, pp. 2857-2879, 2011.

[6] J. Gonçalves, M. de Moura and P. de Castro, "A three-dimensional finite element model for stress analysis of adhesive joints," *International Journal of Adhesion and Adhesives,* vol. 22, no. 5, pp. 357-365, 2002.

[7] P. Schmidt and U. Edlund, "A finite element method for failure analysis of adhesively bonded structures," *International Journal of Adhesion and Adhesives,* vol. 30, pp. 665-681, 2010.

[8] S. E. Stapleton, A. M. Waas and B. A. Bednarcyk, "Modeling progressive failure of bonded joints using a single joint finite element," *AIAA Journal,* vol. 49, no. 8, pp. 1740-1749, 2011.

[9] J. P. Lynch and K. J. Loh, "A summary review of wireless sensors and sensor networks for structural health monitoring," *The Shock and Vibration Digest,* vol. 38, no. 2, pp. 91-128, 2006.

[10] S. P. Beeby, M. J. Tudor and N. M. White, "Energy harvesting vibration sources for microsystems applications," *Measurement Science & Technology,* vol. 17, no. 12, pp. 175-195, 2006.

[11] C. R. Bowen, H. A. Kim, P. M. Weaver and S. Dunn, "Piezoelectric and ferroelectric materials and structures for energy harvesting applications," *Energy & Environmental Science,* vol. 7, pp. 25-44, 2014.

[12] X. D. Xie, N. Wu, K. V. Yuen and Q. Wang, "Energy harvesting from high-rise buildings by a piezoelectric coupled cantilever with a proof mass," *International Journal of Engineering Science,* vol. 72, pp. 98-106, 2013.

[13] M. Moallem, "Design and implementation of a regenerative damper: a review," in *CSME International Congress 2016*, Kelowna.

[14] T. Söllner, "The innovative shock absorber system from Audi: New technology saves fuel and enhances comfort," Audi MediaCenter, 8 October 2016. [Online]. Available: www.audimediacenter.com/en/press-releases/the-innovative-shock-absorber-system-from-audi-newtechnology-saves-fuel-and-enhances-comfort-6551.

[15] N. Mancelos, J. Correia, L. M. Pires, L. B. Oliveira and J. P. Oliveira, "Piezoelectric energy harvester for a CMOS wireless sensor," in *Doctoral Conference on Computing, Electrical and Industrial Systems*, Caparica, 2014.

[16] R. G. Budynas and J. K. Nisbett, Shigley's Mechanical Engineering Design, Ninth Edition, New York: McGraw-Hill, 2011.

[17] L. F. M. da Silva, R. F. T. Lima, R. M. S. Teixeira and A. Puga, "Closed-form solutions for adhesively bonded joints," Universidade do Porto, Porto.

[18] L. F. M. da Silva, P. J. C. das Neves, R. D. Adams, A. Wang and J. K. Spelt, "Analytical models of adhesively bonded joints—Part II: Comparative study," *International Journal of Adhesion and Adhesives,* vol. 29, no. 3, pp. 331-341, 2008.

[19] R. A. Barnes and G. C. Mays, "The transfer of stress through a steel to concrete adhesive bond," *International Journal of Adhesion and Adhesives,* vol. 21, pp. 495-502, 2001.

[20] L. F. M. da Silva and M. J. C. Q. Lopes, "Joint strength optimization by the mixed-adhesive technique," *International Journal of Adhesion and Adhesives,* vol. 29, no. 5, pp. 509-514, 2009.

[21] M. Y. Tsai and J. Morton, "An experimental investigation of nonlinear deformations in single-lap joints," *Mechanics of Materials,* vol. 20, no. 3, pp. 183-194, 1994.

[22] T. C. Silva and L. C. S. Nunes, "A new experimental approach for the estimation of bending moments in adhesively bonded single lap joints," *International Journal of Adhesion and Adhesives,* vol. 54, pp. 13-20, 2014.

[23] J. A. B. P. Neto, R. D. S. G. Campilho and L. F. M. da Silva, "Parametric study of adhesive joints with composites," *International Journal of Adhesion and Adhesives,* vol. 37, pp. 96-101, 2012.

[24] O. Volkersen, "Die Nietkraftverteilung in zugbeanspruchten Nietverbindungen mit konstanten Laschenquerschnitten," *Luftfahrtforschung,* vol. 15, no. 1/2, pp. 41-47, 1938.

[25] O. Sen, S. A. Tekalur and C. Jilek, "The determination of dynamic strength of single lap joints using the split Hopkinson pressure bar," *International Journal of Adhesion and Adhesives,* vol. 31, no. 6, pp. 541-549, 2011.

[26] L. da Silva and R. D. S. G. Campilho, Advances in Numerical Modelling of Adhesive Joints, Berlin: Springer, 2012.

[27] L. F. M. da Silva and A. Öchsner, Modeling of adhesively bonded joints, Berlin: Springer, 2008.

[28] M. Goland and E. Reissner, "The stresses in cemented joints," *Journal of Applied Mechanics,* vol. 11, no. 1, pp. A17-A27, 1944.

[29] M. Sandu, A. Sandu, D. M. Constantinescu and D. A. Apostol, "Single-strap adhesively bonded joints with square or tapered adherends in tensile test conditions," *International Journal of Adhesion and Adhesives,* vol. 44, pp. 105-114, 2013.

[30] N. Stein, H. Mardani and W. Becker, "An efficient analysis model for functionally graded adhesive single lap joints," *International Journal of Adhesion and Adhesives,* vol. 70, pp. 117-125, 2016.

[31] L. J. Hart-Smith, "Adhesive-bonded single-lap joints," Langley Research Center, Hampton VA, 1973.

[32] R. Q. Rodríguez, W. P. de Paiva, P. Sollero, M. R. B. Rodrigues and É. L. de Albuquerque, "Failure criteria for adhesively bonded joints," *International Journal of Adhesion and Adhesives,* vol. 37, pp. 26-36, 2012.

[33] X. He, "Study on forced vibration behavior of adhesively bonded single-lap joint," *Journal of Vibroengineering,* vol. 15, no. 1, pp. 169-175, 2013.

[34] A. Pereira, J. Ferreira, F. Antunes and P. Bártolo, "Analysis of manufacturing parameters on the shear strength of aluminium adhesive single-lap joints," *Journal of Materials Processing Technology,* vol. 210, no. 4, pp. 610-617, 2010.

[35] J. Díaz, L. Romera, S. Hernandez and A. Baldomir, "Benchmarking of three-dimensional finite element models of CFRP single-lap bonded joints," *International Journal of Adhesion and Adhesives,* vol. 30, no. 3, pp. 178-189, 2010.

[36] M. Y. Tsai and J. Morton, "The effect of a spew fillet on adhesive stress distributions in laminated composite single-lap joints," *Composite Structures,* vol. 32, no. 1-4, pp. 123-131, 1995.

[37] A. Rudawska, "Adhesive joint strength of hybrid assemblies: Titanium sheet-composites and aluminum sheet-composites—Experimental and numerical verification," *International Journal of Adhesion and Adhesives,* vol. 30, no. 7, pp. 574-582, 2010.

[38] R. Haghani, M. Al-Emrani and R. Kliger, "Stress distribution in adhesive joints with tapered laminates—Effect of tapering length and material properties," *Journal of Composite Materials,* vol. 44, no. 3, pp. 287-302, 2010.

[39] M. You, Z. M. Yan, X. L. Zheng, H. Z. Yu and Z. Li, "A numerical and experimental study of adhesively bonded aluminium single lap joints with an inner chamfer on the adherends," *International Journal of Adhesion and Adhesives,* vol. 28, no. 1, pp. 71-76, 2007.

[40] M. You, Z. Li, X. L. Zheng, S. Yu, G. Y. Li and D. X. Sun, "A numerical and experimental study of preformed angle in the lap zone on adhesively bonded steel single lap joint," *International Journal of Adhesion and Adhesives,* vol. 29, no. 3, pp. 280-285, 2009.

[41] T. C. Ko, C. C. Lin and R. C. Chu, "Vibration of bonded laminated lap-joint plates using adhesive interface elements," *Journal of Sound and Vibration,* vol. 184, no. 4, pp. 567-583, 1995.

[42] X. He and S. O. Oyadiji, "Influence of adhesive characteristics on the transverse free vibration of single lap-jointed cantilevered beams," *Journal of Materials Processing Technology,* vol. 119, no. 1, pp. 366-373, 2001.

[43] X. He, "Finite element analysis of torsional free vibration of adhesively bonded single-lap joints," *International Journal of Adhesion and Adhesives,* vol. 48, pp. 59-66, 2014.

[44] A. Kaya, M. S. Tekelioğlu and F. Findik, "Effects of various parameters on dynamic characteristics in adhesively bonded joints," *Materials Letters,* vol. 58, no. 27, pp. 3451-3456, 2004.

[45] P. Pandurangan and G. D. Buckner, "Vibration analysis for damage detection in metal-to-metal adhesive joints," *Experimental Mechanics,* vol. 46, no. 5, pp. 601-607, 2006.

[46] Y. Du and L. Shi, "Effect of vibration fatigue on modal properties of single lap adhesive joints," *International Journal of Adhesion and Adhesives,* vol. 53, pp. 72-79, 2014.

[47] X. He, "Numerical and experimental investigations of the dynamic response of bonded beams with a single-lap joint," *International Journal of Adhesion and Adhesives,* vol. 37, pp. 79-85, 2012.

[48] X. Gang, S. Chai, R. J. Allemang and L. Li, "A new iterative model updating method using incomplete frequency response function data," *Journal of Sound and Vibration,* vol. 333, no. 9, pp. 2443-2453, 2014.

[49] S. S. Jin, S. Cho, H. J. Jung, J. J. Lee and C. B. Yun, "A new multi-objective approach to finite element model updating," *Journal of Sound and Vibration,* vol. 333, no. 11, pp. 2323-2338, 2014.

[50] S. V. Modak, "Model updating using uncorrelated modes," *Journal of Sound and Vibration,* vol. 333, no. 11, pp. 2297-2322, 2014.

[51] V. Arora, S. P. Singh and T. K. Kundra, "On the use of damped updated FE model for dynamic design," *Mechanical Systems and Signal Processing,* vol. 23, no. 3, pp. 580-587, 2009.

[52] V. Arora, S. P. Singh and T. K. Kundra, "Damped FE model updating using complex updating parameters: Its use for dynamic design," *Journal of Sound and Vibration,* vol. 324, no. 1-2, pp. 350-364, 2009.

[53] V. Arora, S. P. Singh and T. K. Kundra, "Comparative study of damped FE model updating methods," *Mechanical Systems and Signal Processing,* vol. 23, no. 7, pp. 2113-2129, 2009.

[54] V. Arora, "Comparative study of finite element model updating methods," *Journal of Vibration and Control,* vol. 17, no. 13, pp. 2023-2039, 2011.

[55] T. Naraghi and A. S. Nobari, "Identification of the dynamic characteristics of a viscoelastic, nonlinear adhesive joint," *Journal of Sound and Vibration,* vol. 352, pp. 92-102, 2015.

[56] M. F. Najib, A. S. Nobari and K. Nikbin, "Modification and evaluation of a FRF-based model updating method for identification of viscoelastic constitutive models for a nonlinear polyurethane adhesive in a bonded joint," *International Journal of Adhesion and Adhesives,* vol. 74, pp. 181-193, 2017.

[57] J. Y. Yu and A. Craggs, "Transfer matrix method for finite element models of a chain-like structure under harmonic excitations," *Journal of Sound and Vibration,* vol. 187, no. 1, pp. 169-175, 1995.

[58] P. Chatterjee and M. Bryant, "Transfer matrix modeling of a tensioned piezo-solar hybrid energy harvesting ribbon," in *Proceedings SPIE 9431, Active and Passive Smart Structures and Integrated Systems*, San Diego, 2015.

[59] A. M. Wickenheiser, "Eigensolution of piezoelectric energy harvesters with geometric discontinuities: Analytical modeling and validation," *Journal of Intelligent Material Systems and Structures,* vol. 24, no. 6, pp. 729-744, 2012.

[60] H. Holzer, Die Berechnung der Drehschwingungen, Berlin: Springer, 1921.

[61] N. O. Myklestad, "New method of calculating natural modes of coupled bending-torsion vibration of beams," *Transaction of the ASME,* vol. 67, no. 1, pp. 61-67, 1945.

[62] L. Meirovitch, Fundamentals of Vibrations, Singapore: McGraw-Hill, 2001.

[63] K. B. Subrahmanyam and A. K. Garg, "Uncoupled flexural vibrations of straight beams with all possible boundary conditions treated by a transfer matrix method," *Journal of Sound and Vibration,* vol. 204, no. 3, pp. 397-419, 1997.

[64] J. S. Wu and B. H. Chang, "Free vibration of axial-loaded multi-step Timoshenko beam carrying arbitrary concentrated elements using continuous-mass transfer matrix method," *European Journal of Mechanics A/Solids,* vol. 38, pp. 20-37, 2013.

[65] M. Boiangiu, V. Ceausu and C. D. Untaroiu, "A transfer matrix method for free vibration analysis of Euler-Bernoulli beams with variable cross section," *Journal of Vibration and Control,* vol. 22, no. 11, pp. 2591-2602, 2014.

[66] J. Y. Shen, E. G. Abu-Saba, W. M. McGinley, L. Sharpe Jr and L. W. Taylor Jr, "A piecewise continuous Timoshenko beam model for the dynamic analysis of tapered beam-like structures," NASA STI/Recon Technical Report, 1992.

[67] A. M. Wickenheiser, "Power optimization of vibration energy harvesters utilizing passive and active circuits," *Journal of Intelligent Material Systems and Structures,* vol. 21, pp. 1343-1361, 2010.

[68] M. Zhu, E. Worthington and J. Njuguna, "Analyses of power output of piezoelectric energy-harvesting devices directly connected to a load resistor using a coupled piezoelectric-circuit finite element method," *IEEE Transactions on Ultrasonics, Ferroelectrics, and Frequency Control,* vol. 56, no. 7, pp. 1309-1318, 2009.

[69] E. Lefeuvre, A. Badel, C. Richard, L. Petit and D. Guyomar, "A comparison between several vibration-powered piezoelectric generators for standalone systems," *Sensors and Actuators A,* vol. 126, no. 2, pp. 405-416, 2005.

[70] Y. C. Shu and I. C. Lien, "Analysis of power output for piezoelectric energy harvesting systems," *Smart Materials and Structures,* vol. 15, no. 6, pp. 1499-1512, 2006.

[71] Y. Yang and L. Tang, "Equivalent circuit modeling of piezoelectric energy harvesters," *Journal of Intelligent Material Systems and Structures,* vol. 20, no. 18, pp. 2223-2235, 2009.

[72] H. Liu, "Piezoelectric MEMS energy harvester for low-frequency vibrations with wideband operation range and steadily increased output power," *Journal of Microelectromechanical Systems,* vol. 20, no. 5, pp. 1131-1142, 2011.

[73] F. Lu, H. P. Lee and S. P. Lim, "Modeling and analysis of micro piezoelectric power generators for micro-electromechanical-systems applications," *Smart Materials and Structures,* vol. 13, no. 1, pp. 57-63, 2004.

[74] D. Guyomar, A. Badel, E. Lefeuvre and C. Richard, "Toward energy harvesting using active materials and conversion improvement by nonlinear processing," *IEEE Transactions on Ultrasonics, Ferroelectrics, and Frequency Control,* vol. 52, no. 4, pp. 584-595, 2005.

[75] M. Gallina and D. Benasciutti, "Finite element analysis of optimized piezoelectric bimorphs for vibrational "energy harvesting"," in *International CAE Conference*, Lazise, 2013.

[76] L. Zhang, K. A. Williams and Z. Xie, "Evaluation of analytical and finite element modeling on piezoelectric cantilever bimorph energy harvester," *Transactions of the Canadian Society for Mechanical Engineering,* vol. 37, no. 3, pp. 621-629, 2013.

[77] M. Zhu, E. Worthington and A. Tiwari, "Design study of piezoelectric energy-harvesting devices for generation of higher electrical power using a couple piezoelectric-circuit finite element method," *IEEE Transactions on Ultrasonics, Ferroelectrics, and Frequency Control,* vol. 57, no. 2, pp. 427-437, 2010.

[78] D. F. Berdy, P. Srisungsitthisunti, B. Jung, X. Xu, J. F. Rhoads and D. Peroulis, "Low-frequency meandering piezoelectric vibration energy harvester," *IEEE Transactions on Ultrasonics, Ferroelectrics, and Frequency Control,* vol. 59, no. 5, pp. 846-858, 2012.

[79] R. Q. Rodríguez, P. Sollero, M. B. Rodrigues and É. L. de Albuquerque, "Stress analysis and failure criteria of adhesive bonded single lap joints," in *21st International Congress of Mechanical Engineering*, Natal, Brasil, 2011.

[80] M. Y. Tsai and J. Morton, "An evaluation of analytical and numerical solutions to the single-lap joint," *International Journal of Solids and Structures,* vol. 31, no. 18, pp. 2537-2563, 1994.

[81] A. D. Diaz, R. H. Ahmed, G. Foret and A. Ehrlacher, "Stress analysis in a classical double lap, adhesively bonded joint with a layerwise model," *International Journal of Adhesion and Adhesives,* vol. 29, no. 1, pp. 67-76, 2009.

[82] R. D. Cook, Finite Element Modeling for Stress Analysis, New York: John Wiley & Sons, 1995.

[83] D. M. Gleich, Stress Analysis of Stuctural Bonded Joints, Delft University Press Science, 2002.

[84] L. F. M. da Silva, P. J. das Neves, R. D. Adams and J. K. Spelt, "Analytical models of adhesively bonded joints—Part I: Literature survey," *International Journal of Adhesion and Adhesives,* vol. 29, no. 3, pp. 319-330, 2009.

[85] L. F. M. da Silva and R. B. Adams, "Adhesive joints at high and low temperatures using similar and dissimilar adherends and dual adhesives," *International Journal of Adhesion and Adhesives,* vol. 27, no. 3, pp. 216-226, 2007.

[86] Chatillon, "TCD1100 Digital Force Tester," Chatillon, [Online]. Available: http://www.chatillon.com/products/testers-and-stands/digital-force-testers/tcd1100-digital-force-tester.aspx. [Accessed 24 June 2015].

[87] M. Ignjatovic, P. Chalkley and C. Wang, "The yield behaviour of a structural adhesive under complex loading," Defence Science and Technology Organization, Melbourne, 1998.

[88] Instron, "Tensile Testing," Instron, [Online]. Available: http://www.instron.us/en-us/our-company/library/test-types/tensile-test. [Accessed 17 July 2015].

[89] M. D. Banea and L. F. M. da Silva, "Mechanical characterization of flexible adhesives," *The Journal of Adhesion,* vol. 85, no. 4-5, pp. 261-285, 2009.

[90] D. J. Inman, Engineering Vibration, Pearson Education Inc., 2014.

[91] Comsol, Structural mechanics module user's guide, Comsol, 2016.

[92] C. H. Liu and K. M. Lee, "Dynamic modeling of damping effects in highly damped compliant fingers for applications involving contacts," *Journal of Dynamic Systems, Measurement, and Control,* vol. 134, no. 1, pp. 1-9, 2012.

[93] P. J. Antsaklis and A. N. Michel, Linear Systems, New York: McGraw Hill, 1997.

[94] R. L. Mayes and A. J. Gomez, "Part 4: what's shakin', dude? Effective use of modal shakers," *Experimental Techniques,* vol. 30, no. 4, pp. 51-61, 2006.

[95] M. Mohammadali and H. Ahmadian, "Improvement in modal testing measurements by modeling and identification of shaker-stinger-structure interactions," *Experimental Techniques,* vol. 40, no. 1, pp. 49-57, 2013.

[96] L. Frenzel, "Back to basics: Impedance matching (part 1)," Electronic Design, 24 October 2011. [Online]. Available: http://www.electronicdesign.com/communications/back-basics-impedance-matching-part-1. [Accessed 5 November 2017].

[97] 3M, "3M™ Electrically Conductive Adhesive Transfer Tape 9707," 3M, [Online]. Available: https://www.3m.com/3M/en_US/company-us/all-3m-products/~/3M-Electrically-Conductive-Adhesive-Transfer-Tape-9707?N=5002385+3294001412&rt=rud. [Accessed 24 5 2016].

[98] J. Sirohi and I. Chopra, "Fundamental understanding of piezoelectric strain sensors," *Journal of Intelligent Material Systems and Structures,* vol. 11, no. 4, pp. 246-257, 200.

[99] A. Alipour and F. Zareian, "Study Rayleigh damping in structures; Unceratinties and treatments," in *The 14th World Conference on Earthquake Engineering*, Beijing, 2008.

Appendix

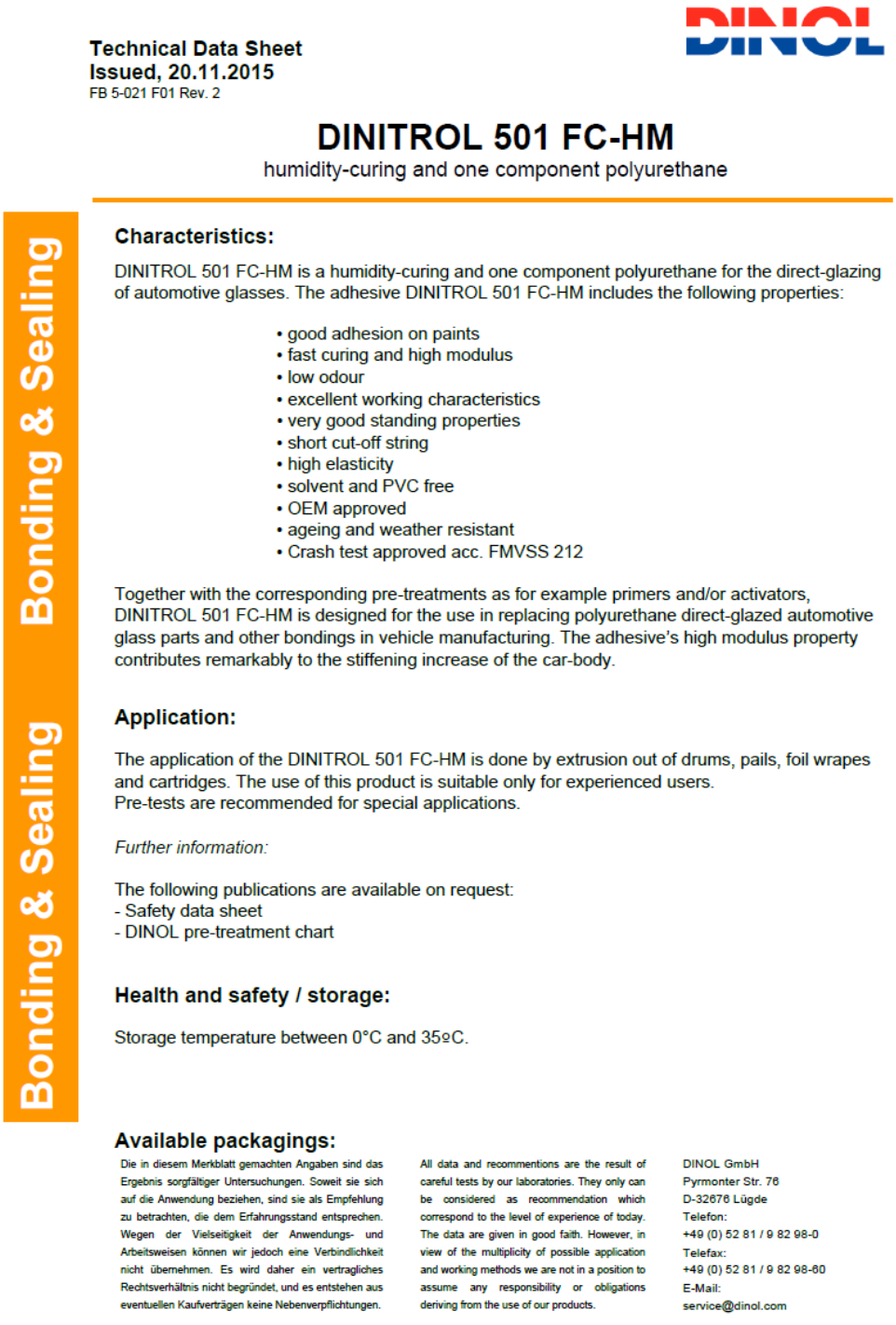

Technical Data Sheet
Issued, 20.11.2015
FB 5-021 F01 Rev. 2

DINITROL 501 FC-HM

humidity-curing and one component polyurethane

Bonding & Sealing

Bonding & Sealing

Characteristics:

DINITROL 501 FC-HM is a humidity-curing and one component polyurethane for the direct-glazing of automotive glasses. The adhesive DINITROL 501 FC-HM includes the following properties:

- good adhesion on paints
- fast curing and high modulus
- low odour
- excellent working characteristics
- very good standing properties
- short cut-off string
- high elasticity
- solvent and PVC free
- OEM approved
- ageing and weather resistant
- Crash test approved acc. FMVSS 212

Together with the corresponding pre-treatments as for example primers and/or activators, DINITROL 501 FC-HM is designed for the use in replacing polyurethane direct-glazed automotive glass parts and other bondings in vehicle manufacturing. The adhesive's high modulus property contributes remarkably to the stiffening increase of the car-body.

Application:

The application of the DINITROL 501 FC-HM is done by extrusion out of drums, pails, foil wrapes and cartridges. The use of this product is suitable only for experienced users.
Pre-tests are recommended for special applications.

Further information:

The following publications are available on request:
- Safety data sheet
- DINOL pre-treatment chart

Health and safety / storage:

Storage temperature between 0°C and 35ºC.

Available packagings:

Die in diesem Merkblatt gemachten Angaben sind das Ergebnis sorgfältiger Untersuchungen. Soweit sie sich auf die Anwendung beziehen, sind sie als Empfehlung zu betrachten, die dem Erfahrungsstand entsprechen. Wegen der Vielseitigkeit der Anwendungs- und Arbeitsweisen können wir jedoch eine Verbindlichkeit nicht übernehmen. Es wird daher ein vertragliches Rechtsverhältnis nicht begründet, und es entstehen aus eventuellen Kaufverträgen keine Nebenverpflichtungen.

All data and recommentions are the result of careful tests by our laboratories. They only can be considered as recommendation which correspond to the level of experience of today. The data are given in good faith. However, in view of the multiplicity of possible application and working methods we are not in a position to assume any responsibility or obligations deriving from the use of our products.

DINOL GmbH
Pyrmonter Str. 76
D-32676 Lügde
Telefon:
+49 (0) 52 81 / 9 82 98-0
Telefax:
+49 (0) 52 81 / 9 82 98-60
E-Mail:
service@dinol.com

Figure A.1: Technical data sheet of Dinitrol 501 FC-HM (page 1)

Technical Data Sheet
Issued, 20.11.2015
FB 5-021 F01 Rev. 2

DINITROL 501 FC-HM

humidity-curing and one component polyurethane

Bonding & Sealing

Bonding & Sealing

Cartridges 310 ml Foil wraps 400 ml Pail 20 L Drum 200 L

Technical properties:

Chemical base:	Polyurethane
Colour:	black paste
Cure mechanism:	humidity-curing
Density (DIN 53217-4):	approx. 1'200 kg/m^3
Non-sag properties:	very good
Application temperature:	10°C – 40°C (product)
Skin formation time[1]:	approx. 20 min.
Open time[1]:	approx. 15 min.
Rate of cure:	approx. 3 – 4 mm / 24 h
Shore A hardness (DIN 53505):	approx. 65 – 75
Tensile strength (DIN 53504):	approx. 11 MPa
Elongation at break (DIN 53504):	approx. 400%
Tear strength (DIN 53515):	approx. 11 N/mm
Lab-shear-strength (DIN EN 1465):	approx. 9 MPa
G-modulus (DIN 54451):	approx. 2.5 MPa
Volume resistivity (DIN 60093):	approx. 10^6 Ωcm
Glass transition temperature:	approx. -40°C
Temperature resistants: short term (approx. 1h)	 < 80°C < 120°C
Shelf life (storages below 25°C): cartridges / foil wrapes drums / pails	 12 month 6 month
Safe-Drive-Away-Time[1]: (FMVSS 212/208) without airbags with passenger airbags	 1 hour 1 hour

[1] 23°C / 50% rf

Health and safety information can be obtained from the material safety data sheet and the product label.

Die in diesem Merkblatt gemachten Angaben sind das Ergebnis sorgfältiger Untersuchungen. Soweit sie sich auf die Anwendung beziehen, sind sie als Empfehlung zu betrachten, die dem Erfahrungsstand entsprechen. Wegen der Vielseitigkeit der Anwendungs- und Arbeitsweisen können wir jedoch eine Verbindlichkeit nicht übernehmen. Es wird daher ein vertragliches Rechtsverhältnis nicht begründet, und es entstehen aus eventuellen Kaufverträgen keine Nebenverpflichtungen.

All data and recommentions are the result of careful tests by our laboratories. They only can be considered as recommendation which correspond to the level of experience of today. The data are given in good faith. However, in view of the multiplicity of possible application and working methods we are not in a position to assume any responsibility or obligations deriving from the use of our products.

DINOL GmbH
Pyrmonter Str. 76
D-32676 Lügde
Telefon:
+49 (0) 52 81 / 9 82 98-0
Telefax:
+49 (0) 52 81 / 9 82 98-60
E-Mail:
service@dinol.com

FigureA.2: Technical data sheet of Dinitrol 501 FC-HM (page 2)

Piezo Material Properties

PROPERTY	UNIT	SYMBOL	SM701	SM702	SM111	SM112	SM118	SM121	SM211	SM311	SM410	SM411	SM422	SM412
EQUIVALENCE			N/A	N/A	Modif. PZT-4	N/A	PZT-8	PZT-4	N/A	PZT-5H	PZT-5J	PZT-5J	Modif. PZT-5	PZT-5A
			N/A	N/A	N/A	N/A	Navy Type III	Navy Type I	N/A	Navy Type VI	Navy Type V	Navy Type V	N/A	Navy Type II
Electromechanical coupling coefficient		K_p	0.65	0.06	0.58	0.59	0.51	0.54	0.67	0.65	0.64	0.64	0.64	0.63
		K_t		0.49	0.45	0.46	0.40	0.43	0.35	0.37	0.45	0.45	0.48	0.42
		K_{31}	0.38		0.34	0.35	0.30	0.32	0.41	0.38	0.36	0.37	0.36	0.35
Frequency constant	Hz • m	N_p	1900		2200	2150	2340	2290	1940	1980	2030	2060	1990	2080
		N_t	1900	2200	2070	2050	2090	2080	1920	1950	2050	2000	2040	2080
		N_{31}			1680	1600	1700	1690	1410	1450	1460	1500	1460	1560
Piezoelectric constant	$\times 10^{-12}$m/v	d_{33}	640	50	320	360	250	300	650	600	500	500	500	450
		d_{31}	-410		-140	-155	-100	-130	-320	-270	-210	-210	-210	-190
	$\times 10^{-3}$Vm/N	g_{33}	16		25	24.7	25.6	26.4	13.6	19.4	23.3	24.2	23.3	25.6
		g_{31}			-11.0	-10.6	-12.5	-12.9	-6.7	-9.2	-10.3	-10.4	-10.3	-12.6
Elastic Constant	$\times 10^{10}$N/m^2	Y_{33}			7.3	7.2	7.4	7.3	5.1	5.3	5.6	5.4	5.6	5.6
		Y_{11}			8.6	8.4	8.7	8.6	6.2	7.2	6.5	7.4	6.5	7.6
Mechanical Quality Factor	-----	Q_m	65	800	1800	1600	1200	1000	60	80	60	85	60	100
Dielectric Constant	@1KHz	$\varepsilon T_{33}/\varepsilon_0$	3800	250	1400	1600	1100	1300	5400	3500	2000	2100	2200	1850
Dissipation Factor	%@1KHz	tan δ	0.4	1.5	0.4	0.6	0.2	0.4	3.0	2.5	2.0	2.0	2.0	1.2
Curie Temperature	°C	T_c	180	250	320	320	300	320	165	220	320	320	290	320
Density	g/cm^3	ρ	7.8	6.9	7.9	7.9	7.6	7.8	7.8	7.8	7.7	7.8	7.7	7.8

Figure A.3: Steminc piezo-ceramic material properties